THE UNIVERSITY *of* EDINBURGH

Nonlinear laser microscopy for the study of virus–host interactions

Iain Thomas ROBINSON

Doctor of Philosophy

THE UNIVERSITY OF EDINBURGH

2010

Abstract

Biomedical imaging is a key tool for the study of host-pathogen interactions. New techniques are enhancing the quality and flexibility of imaging systems, particularly as a result of developments in laser technologies. This work applies the combination of two advanced laser imaging methods to study the interactions between a virus and the host cells it infects.

The first part of this work describes the theory and experimental implementation of coherent anti-Stokes Raman scattering microscopy. This technique—first demonstrated in its current form in 1999—permits the imaging of microscopic samples without the need for fluorescent labelling. Chemical contrast in images arises from the excitation of specific vibrations in the sample molecules themselves. A laser scanning microscope system was set up, based on an excitation source consisting of two titanium-sapphire lasers synchronized with a commercial phase-locked loop system. A custom-built microscope was constructed to provide optimal imaging performance, high detection sensitivity and straightforward adaptation to the specific requirements of biomedical experiments. The system was fully characterized to determine its performance.

The second part of this work demonstrates the application of this microscope platform in virology. The microscope was configured to combine two nonlinear imaging modalities: coherent anti-Stokes Raman scattering and two-photon excitation. Mouse fibroblast cells were infected with a genetically modified cytomegalovirus. The modification causes the host cell to express the green fluorescent protein upon infection. The host cell morphology and lipid droplet distribution were recorded by imaging with coherent anti-Stokes Raman scattering, whilst the infection was monitored by imaging the viral protein expression with two-photon excitation. The cytopathic effects typical of cytomegalovirus infection were observed, including expansion of the nucleus, rounding of the cell shape, and the appearance of intracellular viral inclusions. In some cases these effects were accompanied by dense accumulations of lipid droplets at the nuclear periphery. Imaging was performed both with fixed cells and living. It was demonstrated that the lipid droplets in a single live cell could be imaged over a period of 7 hours without causing noticeable laser-induced damage. The system is shown to be a flexible and powerful tool for the investigation of virus replication and its effects on the host cell.

Declaration

This thesis has been written entirely by me and has not been submitted in any previous application for a degree. Except where stated, all the work detailed in this thesis was carried out by me.

Iain Robinson

1st March 2010

Acknowledgements

This work would not have been possible without the help and support of many people. I would sincerely like to thank the following people for the parts they played, both large and small, in enabling me to write this thesis:

My supervisors Will Hossack and Jason Crain for their scientific expertise, patient guidance and enthusiasm throughout. Without their unwavering support I could not have completed this.

Jochen Arlt for all his help and encouragement and Gerard Giraud for mentoring me.

Everyone who worked with me on the virology project including Holly Gibbs, Michael Ochsenkühn, Rob Menzies and Colin Campbell. Chrissy Wong for her dedication in learning the ropes and for contributing some of the images in this thesis.

Anthony Lee and Alvin Yeh of Texas A&M University who generously provided me with their software for the microscope system.

Andy Garrie for his technical skill in making numerous parts for the microscope. Eric Davidson who provided the important supplies. Hugh Vass for the benefit of his creativity and ingenuity.

Craig Gregor, Mira Nishimura and Chrissy Wong again for making the office always a friendly place.

Jane Patterson for looking after all the postgraduates in the School of Physics and Astronomy. Joan Myott for looking after the flat.

The tutors of various skills courses, who taught me much in a very short time. Dave Filipović-Carter, Piero Vitelli, Robin Henderson, Pat Reid, Anna Tinline, Hamish Macleod, Lorna Sinclair, Chris Robinson and Bill Earnshaw. And Jorge Cham for the most entertaining seminar ever.

My friends in the School of Physics and Astronomy for making it such a great place to work these few years. Grace Kim for music and Korean food; Colin Mclean for swimming and bicycles; Danielle van 't Zand for bread and Beanscene. The basketballers for the outdoor exercise. Louis in Starbucks for giving me too much coffee.

Finally, my parents for their support throughout.

Sir Chandrasekhara Venkata Raman
Portrait by Homi Bhabha

Contents

Abstract **ii**

Declaration **iii**

Acknowledgements **iv**

1 Introduction **1**

2 Coherent anti-Stokes Raman Scattering **4**
2.1 Introduction 4
2.2 Theory 5
2.3 Instrumentation 11
2.4 Techniques 20
2.5 Applications 22
2.6 Stimulated Raman scattering 24
2.7 Conclusions 24

3 The CARS microscope **26**
3.1 Introduction 26
3.2 Overview 26
3.3 The laser system 29
3.4 The microscope system 34
3.5 Testing and characterization 41
3.6 Conclusions 53

4 Intracellular imaging with CARS **54**
4.1 Introduction 54
4.2 Background 55
4.3 Methods 57
4.4 Results 57
4.5 Discussion 63
4.6 Conclusions 64

5 Multimodal imaging of fixed cells **65**
5.1 Introduction 65
5.2 Background 67
5.3 Methods 73
5.4 Results 75
5.5 Discussion 80

5.6 Conclusions 83

6 Live cell imaging **85**
6.1 Introduction 85
6.2 Background 86
6.3 Methods 87
6.4 Results 89
6.5 Discussion 95
6.6 Conclusions 96

7 Conclusions **98**

Bibliography **101**

A Publication **113**

1 Introduction

This thesis presents a new method for studying the interactions between viruses and the host cells they infect. The topic of this thesis is coherent anti-Stokes Raman scattering (CARS) microscopy. The objective is to construct a CARS microscope and apply it to an area of biomedical science. For the application two different imaging techniques, CARS and two-photon microscopies, are combined in a single experimental set-up and used to study cultured cell specimens under infection by a virus. This chapter will give a general introduction to the topic, a short description of the method and results, and an outline of the thesis.

The development of new optical materials has led to substantial advances in the quality of lenses for microscopes. At the same time a wealth of technological innovations—such as video microscopy, confocal optics, digital image analysis and chemical labelling—have brought about a Renaissance in the science of microscopy [1]. As a result of the introduction of laser scanning confocal microscopy in the 1980s modern microscopes, whilst still based around light and lenses, now incorporate the latest laser sources and detection technologies providing unprecedented levels of clarity and detail. In turn, the paramount importance of this scientific instrument, particularly for biomedical studies, is motivating further advancements in laser technology which are pushing the light microscope to its limits. The research described in this thesis has been enabled by just such advancements. Specifically, the nonlinear processes used here, CARS and two-photon, require pulsed lasers which can deliver momentary bursts of high-intensity light into the specimen inducing the simultaneous interaction with multiple photons. The result is that the excitation of molecules in the specimen can be targeted and confined to a small volume with pinpoint accuracy allowing high-resolution microscopic imaging.

Meaningful contrast is critical in microscopy [1]. The traditional microscope provides very limited contrast and most thin specimens appear transparent. Enhanced contrast can be achieved by staining, but this usually damages or destroys the specimen. Fluorescent labels added to samples can localize to specific compounds allowing their selective imaging when excited by a lamp or scanned by a laser beam. A huge variety of such compounds have been developed providing microscopists with the specificity required to pick out certain compounds or chemicals. However the use of fluorophores suffers several drawbacks. The addition of foreign compounds to the specimen can interfere with the natural functions or processes being studied. This is particularly an issue in biomedical studies which image the complex and dynamic intracellular environment. *Label-free* imaging can circumvent these difficulties and permits imaging without the addition of exogenous fluorophores. CARS microscopy is a label-free technique which provides chemical contrast by selectively exciting molecular bonds in the sample molecules.

The history of CARS begins at the Ford Motor Company in 1965 with the systematic study of this spectroscopic effect by Maker and Terhune [2]. CARS *microscopy*, i.e. the use of the CARS process for microscopic imaging, made something of a false start. After its invention by Duncan et al. [3] in 1982 it appears to have languished in obscurity for over a decade until its accidental rediscovery by Zumbusch and co-workers in 1999 [4]. Since its comeback the field has blossomed and CARS microscopy has been applied in a wide variety of biomedical imaging studies [5].

The undoubted success of CARS as a tool for label-free imaging comes with two important caveats. Firstly, CARS microscopy is, like almost all techniques of light microscopy, limited in resolution by diffraction. Secondly, CARS is affected by a background signal which complicates interpretation of images and can obscure the features being studied. Whilst progress has been made in addressing the second of these issues [6, 7], the first is more fundamental in nature. This is problematic for any virological application of light microscopy, such as this one, as viral particles are too small to be imaged with light. Such applications therefore concentrate on observing the effect of the virus on its host and this is the approach adopted here. The understanding of the complex nature of virus-host interactions leads to a clearer understanding of the virus life cycle with the ultimate aim of producing more effective interventions and treatments for viral diseases.

The experimental work presented in this thesis therefore links two areas of science: the physics of laser microscope systems and the virology of host-pathogen interactions. The techniques applied—CARS microscopy, two-photon microscopy, cell culture and live cell imaging—will all be described, but the focus will be on CARS microscopy as this is still a maturing technique. In contrast, two-photon microscopy [8] has already followed the route from the optical bench to the bioimaging lab and will therefore be outlined only briefly. The results will demonstrate that the combination of the two imaging modalities provides a powerful platform for imaging host-pathogen interactions, specifically to aid understanding of the

complex relationship between viruses and their host cells and the perturbations they can cause to host cell lipids. This thesis is structured as follows:

Chapter 2 describes the theory of CARS and explains its relationship with other optical processes. It outlines the instrumentation involved, including the laser system and the unique features of a CARS microscope. A review is presented of the techniques and applications developed around CARS microscopy.

The experimental set-up is detailed in **Chapter 3**. This gives a brief description of the laser system, followed by a more detailed explanation of the construction, operation and testing of the microscope system.

In **Chapter 4** the microscope is used to image intracellular lipid droplets in fixed cell specimens. The performance and reliability of the system are demonstrated.

Chapter 5 presents the results of experiments imaging the interactions between a virus and its host cell. The chapter begins with a brief introduction to virology and explains the methods applied, which include the combination of CARS and two-photon microscopies. The results of imaging experiments conducted on infected cells are presented and a discussion of the biomedical significance of these results is given.

Chapter 6 extends the microscope system to support live cell imaging. The ability to image single cells over a periods of hours is demonstrated.

Finally, **Chapter 7** concludes and offers suggestions for future work.

2

Coherent anti-Stokes Raman Scattering

2.1 Introduction

The purposes of this chapter are to outline the theory of coherent anti-Stokes Raman scattering (CARS) and to provide a broad overview of the present-day field of CARS microscopy. The literature review presented here aims to put the work of the following chapters into context.

The first section of this chapter will outline the theoretical aspects of CARS relevant to its use for microscopy. It will begin with a brief overview of Raman scattering, the antecedent of CARS. Then, the mechanism and conditions for CARS signal generation will be given. The presence of a background signal is a significant complication when applying the process. The origin of this background will be explored. Raman spectroscopy is an important complimentary technique to CARS, though there are significant differences between the two processes and these will be explained in detail. The significant distinctions between CARS, two-photon, and confocal microscopies will also be highlighted.

Setting up a CARS microscope requires a careful choice of instrumentation. There is as yet no universal design and commercial systems have appeared only very recently. An overview will be given of the design decisions that must be made, with emphasis on the properties of the laser system and the ways in which the microscope set-up differs from standard commercial systems such as confocal and two-photon.

A review will be made of the most important techniques and applications of CARS microscopy. CARS is, foremost, a spectroscopic technique. The literature review in this chapter will focus primarily on its use for microscopy, and mention the broader arena of CARS spectro-

scopy only where specifically relevant.

Finally, a brief description of stimulated Raman scattering will be given. This is a recent spin-off from CARS microscopy that addresses some of its shortcomings. An outline of this new technique will be given as a pointer to the likely future direction of this research field.

2.2 Theory

This section outlines the theoretical background to Raman scattering and CARS, then highlights the important differences between the two.

2.2.1 Raman scattering

The Raman effect is the inelastic scattering of a photon from a sample, manifested as a shift in the photon's frequency. The shift is the result of the exchange of energy between the photon and the molecule's vibrational state. The effect is very weak; of those photons which are scattered, most are Rayleigh scattered with no change in wavelength whilst around 1 in 10^5 are Raman scattered [9]. The scattered light carries detailed chemical information about the sample encoded in its Raman spectrum. Raman spectroscopy is often used as a companion to CARS as the Raman spectrum can be used to select a target vibrational resonance for CARS.

This theoretical outline will use a classical model to illustrate the origin of the Raman effect and to define the terminology and notation used in later sections. A quantum-mechanical treatment, which explains the selection rules that produce Raman spectra, is given by Ferraro et al. [10].

The light wave incident on a sample molecule is represented as a time-varying sinusoidal electric field with frequency ω_0 and vector amplitude $\mathbf{E_0}$

$$\mathbf{E} = \mathbf{E_0} \cos \omega_0 t$$

This field induces a time-varying molecular dipole moment $\mathbf{p}$. Generally, $\mathbf{p}$ can be expressed as a series expansion in powers of the electric field

$$\mathbf{p} = \mathbf{p}^{(1)} + \mathbf{p}^{(2)} + \mathbf{p}^{(3)} + \dots \tag{2.1}$$

If the incident light is not too intense, the induced dipole moment will be small, and the first-order term $\mathbf{p}^{(1)}$ is sufficient to accurately describe the dipole oscillation. The problem can be further simplified by considering a diatomic molecule vibrating in one dimension. The polarization is then simply proportional to the applied field

$$p^{(1)} = \alpha E = \alpha E_0 \cos \omega_0 t \tag{2.2}$$

where α is the molecule's polarizability. α will depend on the nuclear coordinate q which

defines the vibrational displacement. A change in q will change the separation between charges and hence alter the molecular polarizability. For small nuclear displacements, α can be expanded to first-order in q

$$\alpha = \alpha_0 + \alpha' q \tag{2.3}$$

where α_0 is the polarizability at equilibrium ($q = 0$) and $\alpha' = \frac{d\alpha}{dq}\Big|_{q=0}$ is the derivative of the polarizability evaluated at the equilibrium position.

Assuming mechanical harmonicity, i.e. that the restoring force of the molecular bond is proportional to q, the molecule will execute simple harmonic motion with amplitude q_0 and frequency Ω

$$q = q_0 \cos \Omega t \tag{2.4}$$

Substituting Equations 2.3 and 2.4 into Equation 2.2 gives the first-order time-varying dipole moment

$$p^{(1)} = \alpha_0 E_0 \cos \omega_0 t + \frac{1}{2}\alpha' E_0 q_0 \left(\cos(\omega_0 + \Omega)t + \cos(\omega_0 - \Omega)t\right)$$

This represents an oscillating dipole with three distinct frequency components, causing radiation at each of these frequencies:

- Rayleigh scattering: Frequency ω_0 is scattered at the same frequency as the incident light.
- anti-Stokes Raman scattering: Frequency $\omega_{as} \equiv \omega_0 + \Omega$ is *blueshifted* from the incident light.
- Stokes Raman scattering: Frequency $\omega_s \equiv \omega_0 - \Omega$ is *redshifted* from the incident light.

For a given frequency ω_0, Rayleigh scattering can occur from any polarizable molecule. Stokes and anti-Stokes scattering will only occur for Raman-active vibrations where $\alpha' \neq 0$, i.e. where the polarizability has a non-zero gradient at the equilibrium position. Figure 2.1(A) and (B) shows energy diagrams of the three processes. Anti-Stokes scattering transfers energy from the molecule to the photon and occurs when light is scattered from a molecule already in an excited vibrational state. Stokes scattering transfers energy from photon to molecule, leaving the molecule in an excited state. At room temperature, assuming a Boltzmann distribution of molecular vibrational energies, Stokes scattering is dominant.

This model considered only a single vibration in one-dimension. In general there will be many molecular vibrations present in different directions. The generalization of this model to three dimensions therefore sees α become the polarizability tensor. It was assumed that the variation of the polarizability is proportional to the first power of the nuclear displacement (q). The more general model is outlined by Long [11].

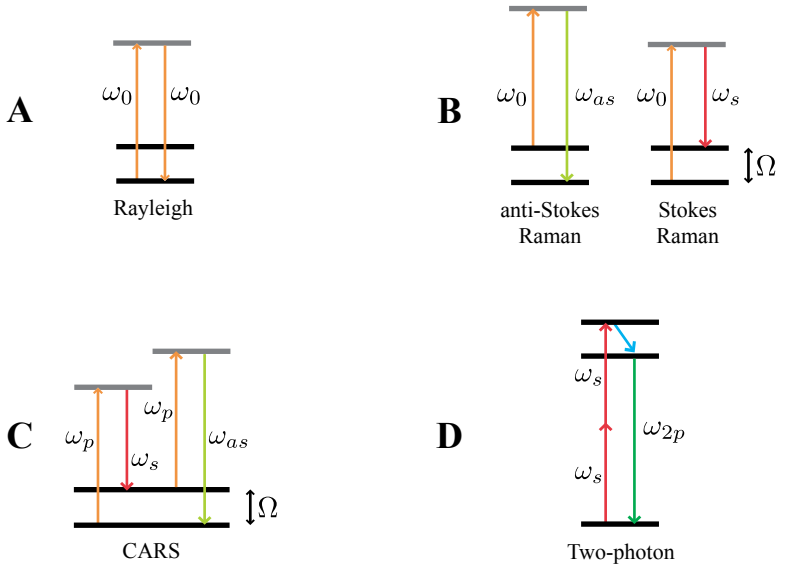

Figure 2.1: Energy diagrams of scattering processes (A–C) and two-photon fluorescence (D). Two-photon excitation is shown using the Stokes frequency (see Section 5.3.2). Unlike the scattering processes (A–C) two-photon fluorescence (D) produces a broad spectrum of emission frequencies ω_{2p}.

2.2.2 CARS

CARS is a four-wave mixing process. Three fields—*pump, Stokes* and *probe*—are mixed in a sample producing a fourth *anti-Stokes* (CARS) field. In most set-ups the pump and probe photons derive from the same laser beam, with the same frequency ω_p, and both are referred to as *pump*. The Stokes field comes from a separate laser and has a frequency ω_s, which is lower than the pump frequency. The mixing process produces a CARS field with frequency ω_{as}. An energy diagram of the process is shown in Figure 2.1(C) from which the frequency of the CARS field can be determined

$$\omega_{as} = 2\omega_p - \omega_s \tag{2.5}$$

The CARS field is resonantly enhanced when the frequency difference Ω between the pump and Stokes fields is tuned to a vibrational resonance of the sample molecules

$$\Omega = \omega_p - \omega_s \tag{2.6}$$

In contrast to Raman scattering, CARS is a coherent technique. The pump and Stokes fields drive all resonant oscillators in the excitation volume at frequency Ω with a well-defined phase. The CARS field results from the combined radiation from these oscillators. As a consequence

the signal cannot be considered from a single molecular dipole alone, but must be expressed as the superposition of the signals from an ensemble of dipoles. The expansion shown in Equation 2.1 is therefore rewritten in terms of the dipole moment per unit volume, i.e. the polarization

$$\mathbf{P} = \mathbf{P}^{(1)} + \mathbf{P}^{(2)} + \mathbf{P}^{(3)} + \dots \tag{2.7}$$

CARS is a third-order process, with the signal originating from the induced third-order polarization $\mathbf{P}^{(3)}$. The electric field resulting from the third-order polarization of a material is the sum of 44 different frequency components representing different mixing combinations of the three fields [12]. In CARS, the anti-Stokes frequency is produced by frequency mixing of the wavelength combination given by Equation 2.5. The corresponding relationship between the third-order polarization and the applied field is

$$P^{(3)} = 3\epsilon_0 \chi^{(3)} E_{\mathrm{p}}^2 E_{\mathrm{s}}^*$$

where $\chi^{(3)}$ is the third-order electric susceptibility tensor and E_p and E_s are the pump and Stokes fields. Other third-order processes will also be present, however the CARS process can become significant when exciting a resonance of $\chi^{(3)}$, although an appreciable nonresonant polarization will also be caused. The general form for $\chi^{(3)}$ was derived by Lotem et al. [13]. The full expression may be simplified by separating it into nonresonant (NR) and resonant (R) parts

$$\chi^{(3)} = \chi_{\mathrm{NR}}^{(3)} + \frac{\chi_{\mathrm{R}}^{(3)}}{\Delta - i\Gamma} \tag{2.8}$$

where Δ is the detuning from the Raman vibrational energy Ω

$$\Delta = \omega_p - \omega_s - \Omega$$

and Γ is the half-width of the resonance.

The relative intensity of the CARS field I_{as} can be found by solving the wave equation with the assumption that the pump and Stokes fields are plane waves [5]

$$I_{as} \propto \left|\chi^{(3)}\right|^2 I_p^2 I_s \left(\frac{\sin\frac{\Delta k z}{2}}{\frac{\Delta k}{2}}\right)^2 \tag{2.9}$$

where z is the sample thickness and Δk is the magnitude of the wavevector mismatch

$$\Delta k = |\mathbf{k}_{as} - (2\mathbf{k}_p - \mathbf{k}_s)| \tag{2.10}$$

Equation 2.10 is known as the phase-matching condition and depends on the beam frequencies, the refractive index of the nonlinear material and the angular relationship between

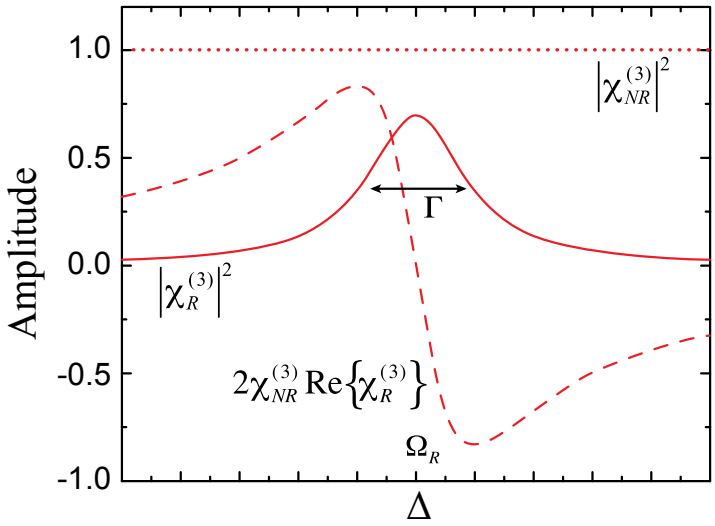

Figure 2.2: Graph of the magnitude of the susceptibility (in arbitrary units) against the detuning $\Delta = \omega_p - \omega_s - \Omega$ showing the three terms in Equation 2.11. This figure is reproduced from Evans [5].

the beam directions. The efficiency of nonlinear optical processes is maximal when perfect phase-matching is achieved, $\Delta k = 0$ [12]. This is often difficult to arrange experimentally and is generally achieved by careful angular tuning of the beam directions to optimize the nonlinear signal generated. Early experiments in CARS spectroscopy [14] and microscopy [3] used complex beam geometries to allow efficient signal generation. Whilst Equation 2.9 describes the intensity for plane waves, the conditions for efficient signal generation are altered when the beams are focused. For the CARS process specifically, the efficiency depends on the tightness of the beam focus [15]. The tightness of focusing is defined by the numerical aperture, $\mathrm{NA} = n \sin\theta$, where θ is the half-angle of the cone of focused light and n is the refractive index of the material. If using a lens with a high NA the wide angular spread of the wavevectors of the incident light ensures there are rays which will satisfy the phase-matching condition allowing efficient signal generation without a complex geometric beam configuration. In 1999, over a decade after the invention of CARS microscopy [3], Zumbusch et al. [4] reported a CARS microscope which used a collinear beam geometry and focused the beams with a high NA microscope objective lens. This set-up, with its simpler arrangement of the laser beams, immediately rekindled interest in CARS microscopy.

The proportionality relationship between the CARS signal intensity (I_{as}) and the nonresonant and resonant susceptibilities can be determined by substituting Equation 2.8 into 2.9. This gives the relative intensity as a function of the detuning Δ

$$I_{as}(\Delta) \propto \left|\chi^{(3)}_{\mathrm{NR}}\right|^2 + \left|\chi^{(3)}_{\mathrm{R}}(\Delta)\right|^2 + 2\chi^{(3)}_{\mathrm{NR}}\mathrm{Re}\left\{\chi^{(3)}_{\mathrm{R}}(\Delta)\right\} \tag{2.11}$$

The three terms in this equation are graphed separately in Figure 2.2. The first term, which

is nonresonant, does not depend on the detuning. Its effect is to add a constant background to CARS measurements. It contains no chemical information and is, from an experimental perspective, useless. The second term is resonant and does depends on the detuning. The third term indicates that there is interference between the nonresonant and resonant parts of the signal. As this term depends linearly on $\chi_{\mathrm{R}}^{(3)}$ it becomes particularly significant at low concentrations or when imaging weaker Raman bands.

2.2.3 Comparison of CARS with other optical processes

This section will provide a brief comparison of CARS with other nonlinear imaging techniques, i.e. those in which the detected signal results from a higher-order polarization of the material (Equation 2.7). Besides CARS, these methods include two-photon [8], second harmonic generation [16] and third harmonic generation [17] microscopies. Whilst the technologies and methods applied for CARS imaging are broadly similar to these other techniques, there are distinct features, the experimental implications of which are discussed in the following section. In this section, a brief comparison is made in order to highlight these distinctions and place CARS in the context of other nonlinear techniques. A comparison is also made with Raman spectroscopy as the two techniques are complimentary and are often used side-by-side.

Whilst both Raman and CARS target the same vibrational bands, there are differences in the spectra caused by the presence of the nonresonant background in CARS. In contrast, Raman is background-free. The nonresonant background is a significant complication in CARS microscopy as it can mask the resonant CARS signal, especially when imaging weak Raman bands or low molecular concentrations. It also distorts CARS spectra slightly when compared to their equivalent Raman spectra. The differences arise from the interference between the resonant and nonresonant parts of the signal (the third term in Equation 2.11). As a result, the shape of the CARS resonance has two distinct characteristics when compared with the Raman:

- The peak is redshifted (i.e. to a lower energy).
- There is a sharp dip on the blue side.

These features can be seen in Figure 2.2. For this reason it is not possible to compare Raman and CARS spectra directly. This limits the utility of CARS as a spectroscopic technique and means care must be taken when imaging to correctly locate peaks in the CARS spectrum.

CARS imaging can be performed on an adapted two-photon (or confocal) microscope, however there are significant differences between CARS and processes which rely on fluorescence. Specifically, the coherent nature of CARS means that the signal is the result of constructive interference from all the oscillators in the excitation volume. As a consequence the signal is highly directional, with the direction depending on the size and shape of the scatterer. In techniques which excite fluorescent molecules, such as two-photon microscopy, the excited fluorophore molecules emit in all directions.

Unlike Raman and two-photon microscopies, in CARS the intensity of the signal is proportional to the square of the number of oscillators in the excitation volume ($|\chi^{(3)}|^2$ in Equation 2.9). This gives a signal that scales nonlinearly with the concentration of sample molecules which can complicate the interpretation of CARS images. The scaling law also results in a rapid drop-off in signal as concentration is lowered.

2.3 Instrumentation

The theory outlined in the previous section enables a concrete specification of the instrumentation required for CARS microscopy. The most significant advances over the past decade have been due to improvements in the laser technology. This section will provide a brief review of these developments, then describe the broad features of the CARS microscope. The specific details of the set-up used in this thesis will be explained in Chapter 3.

2.3.1 Laser source: requirements

The laser source for CARS has the following requirements:

- It must provide two frequencies ω_p and ω_s. At least one frequency must be tunable such that the difference $\Omega = \omega_p - \omega_s$ (Equation 2.6) can be arranged to exactly coincide with the selected Raman vibration.
- The laser light must be pulsed to provide the high peak power required for effective nonlinear signal generation whilst maintaing a moderate average power which will not destroy the sample.
- The pulses must be temporally synchronized in both separation and phase, and spatially overlapped when focused into the sample. This enables pulses of each frequency to mix.

In addition to these absolute requirements there are a number of desirable properties that the sources should have. These are discussed in more detail below.

Wavelengths

The first CARS microscope was implemented with visible lasers [3]. However visible wavelengths are not ideal for CARS due to the photodamage they cause to biological specimens. Switching to infrared wavelengths, in the range 780–$1300\,\mathrm{nm}$, provides a number of advantages. Biological specimens generally have lower absorption at these wavelengths, minimizing sample heating effects and reducing photodamage. Additionally there is reduced *nonlinear* absorption, such as two-photon, reducing the chance of *nonlinear* photodamage [18]. There are also fewer two-photon electronic resonances which contribute to the nonresonant background [19]. Finally, Rayleigh scattering of light within the sample, with wavelength λ,

scales as λ^{-4}. Moving to longer wavelengths therefore increases the penetration depth as both the excitation beams and the CARS signal suffer less scattering. The penalty of moving into the infrared is a reduction in spatial resolution, however this drawback is generally offset by the advantages and most CARS microscopes therefore use infrared excitation.

Pulse duration

Most nonlinear imaging techniques such as two-photon microscopy utilize the shortest possible laser pulses to provide the maximum peak power and hence optimize the efficiency of nonlinear signal generation. Titanium-sapphire (Ti:sapphire) lasers [20] are a popular choice for two-photon microscopy due to their tunability over a range of red-to-infrared (660–$1180\,\mathrm{nm}$) wavelengths. The short pulse duration, typically $\Delta\tau = 100\,\mathrm{fs}$ or shorter, provides efficient signal generation whilst maintaing a modest average power that will not damage photosensitive samples. In contrast, the nature of CARS is more complex and requires a careful selection of the pulse duration to optimize the sensitivity.

Light emitted by pulsed lasers consists of a range of frequencies which define the pulse spectral bandwidth $\Delta\omega$, usually specified in units cm^{-1}. When the shortest possible pulse is generated from the available bandwidth the pulse is *transform-limited*. The time-bandwidth product [21] defines the inverse relationship between the shortest pulse duration $\Delta\tau$ and the minimum spectral bandwidth with the constant determined by the pulse shape. For pulses with a sech^2 profile

$$\Delta\tau\Delta\omega = 1.98 \tag{2.12}$$

where both $\Delta\tau$ and $\Delta\omega$ are the full width of the range at half the maximum (FWHM) intensity.

The spectral bandwidth of a typical $100\,\mathrm{fs}$ pulse used for nonlinear imaging is $100\,\mathrm{cm}^{-1}$. This is much wider than many Raman vibrational linewidths (10–$20\,\mathrm{cm}^{-1}$) and is therefore less suitable for CARS. As well as compromising spectral resolution, such short-duration pulses will cause nonresonant excitation outwith the CARS resonance, giving a large nonresonant background which can swamp the resonant signal. Cheng et al. [22] calculated, by numerical simulation, the relative intensities of the resonant and nonresonant contributions to the signal as a function of the pulse duration, or equivalently (Equation 2.12) the pulse spectral bandwidth. Their graph is shown in Figure 2.3.

The pulse duration should be selected not to maximize the overall signal, but to optimize the ratio of resonant signal to nonresonant background. In practice pulse durations in the range 2–$7\,\mathrm{ps}$ (2–$5\,\mathrm{cm}^{-1}$ spectral bandwidth) provide a good balance, producing sufficient resonant signal for imaging whilst maintaining the spectral resolution that gives chemical contrast.

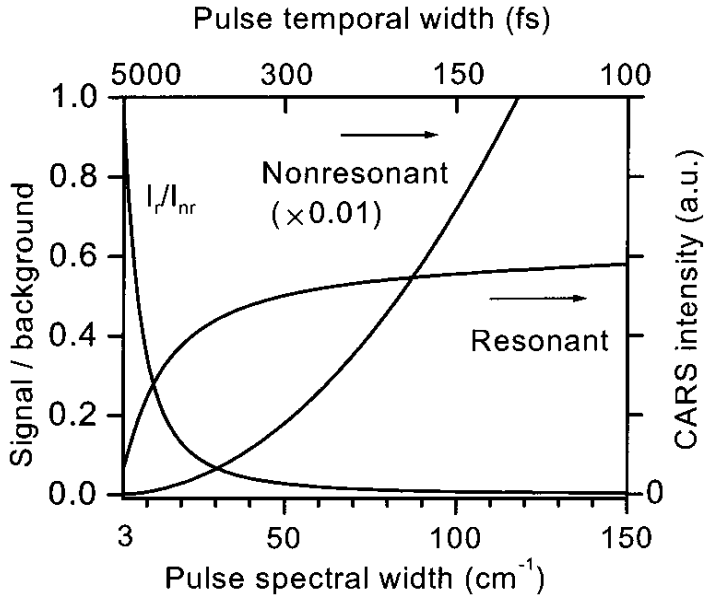

Figure 2.3: Graph of the intensities of the nonresonant (I_{NR}) and resonant (I_{R}) parts of the CARS signal, and their ratio $I_{\mathrm{R}}/I_{\mathrm{NR}}$, as a function of the pulse spectral width or, equivalently, the pulse duration (Equation 2.12). The intensity units are arbitrary. This figure is reproduced from Cheng [22].

Repetition rate

Most mode-locked lasers used for two-photon imaging have a repetition rate of around $80\,\mathrm{MHz}$. Whilst this is partly for historical reasons [23] it also provides a reasonable compromise between the high peak power required for efficient two-photon excitation whilst maintaining a pulse spacing longer than typical fluorescence lifetimes to avoid saturation. Higher repetition rates (for the same average power), also carry a greater risk of photodamage to specimens. The compromise (at $80\,\mathrm{MHz}$) for two-photon imaging is also suitable for CARS. Where samples are particularly sensitive to damage the repetition rate can be reduced with a pulse picker, but the reduced rate must be carefully chosen to provide the ideal balance between average power, peak power and image acquisition speed [24].

2.3.2 Laser source: implementations

The ideal light source for CARS microscopy would be a compact turnkey laser system tuneable over a wide range of Raman shifts (500–$3600\,\mathrm{cm}^{-1}$) with all the properties described above. As yet there is no single light source which can provide this, though the demands of CARS microscopy are motivating the development of new lasers which may yet achieve this ideal. As there is no universally-adopted laser source for CARS it will be useful to outline the salient features of some of the laser systems which have been implemented. These fall into several broad classes which are represented in Figure 2.4.

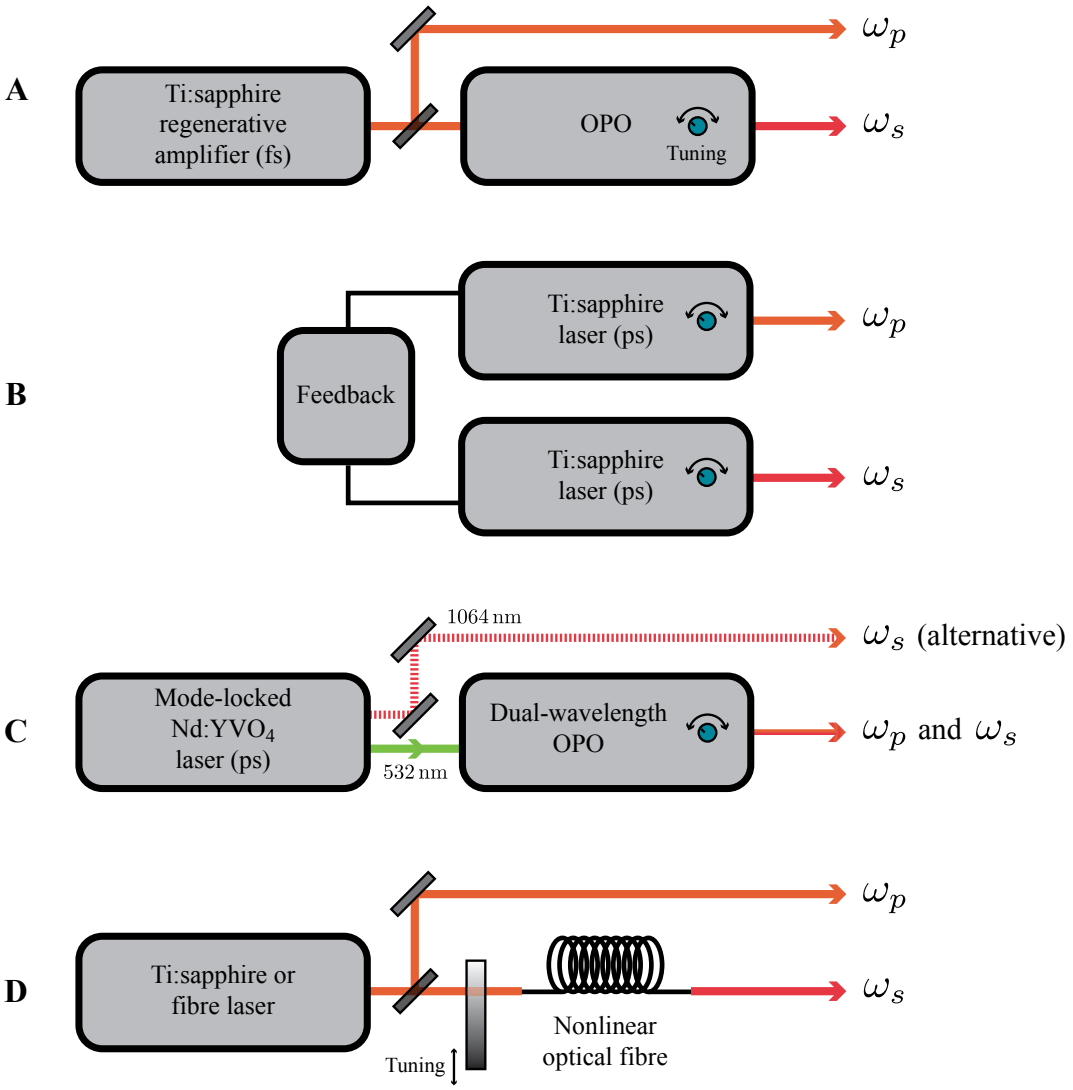

Figure 2.4: Illustration of several laser sources for CARS microscopy. CARS requires two pulsed synchronized beams at the pump (ω_p) and Stokes (ω_s) frequencies. At least one of these must be tunable. The first CARS microscopes used an optical parametric oscillator (OPO) pumped by a Ti:sapphire amplifier (A). CARS can be implemented with a pair of independent Ti:sapphire lasers with active feedback to synchronize pulses (B). A dual-wavelength OPO can provide synchronized and overlapped pump and Stokes pulses (C). A nonlinear fibre can be used to shift the pump wavelength to generate an inherently synchronized Stokes wavelength (D). For CARS microscopy the two frequencies must be overlapped both spatially and temporally with a beam-splitter and optical delay line (not shown in the diagram). Source (C) is an exception to this, as the two frequencies are inherently overlapped when they exit the OPO.

The rediscovery of CARS microscopy in 1999 used a Ti:sapphire regenerative amplifier and an optical parametric oscillator (OPO) to generate the pump and Stokes pulses respectively [4]. This setup is illustrated in Figure 2.4(A). The synchronous pumping of the OPO produced femtosecond pulses at the Stokes wavelength that were inherently synchronized to the pump pulses from the amplifier. Tuning the OPO adjusted the difference between the Stokes and pump frequencies (Equation 2.6) allowing selection of specific Raman shifts in the range 2600–3300 cm^{-1}. The two output beams were combined collinearly on a dichroic mirror and temporally overlapped by adjusting an optical delay line inserted into one of the beam paths (not shown in the diagram).

The revival of CARS microscopy immediately triggered efforts in several research groups to find more suitable laser sources. Hashimoto et al. [25] extended the range of the laser source into the *fingerprint region,* the congested spectral range 500–1800 cm^{-1} where many chemically important vibrational bands reside. Cheng et al. [22] reported a microscope based on a pair of synchronized Ti:sapphire lasers with an electronic feedback system to maintain a pulse separation and phase lock, Figure 2.4(B). However the relatively large timing jitter (0.5 ps) between the pump and Stokes pulses caused the appearance of visible noise in images. Subsequent improvements in the synchronization method [26] reduced the jitter, leading to CARS images free of jitter noise [27]. Ganikhanov et al. [28] developed a tunable OPO in which *both* the outputs, signal and idler, are used as the pump and Stokes frequencies respectively, Figure 2.4(C). The OPO was synchronously pumped by a mode-locked frequency-doubled neodymium:yttrium orthovanadate (Nd:YVO_4) laser [29] at a wavelength of 532 nm, a commonly-used pump for modern Ti:sapphire lasers and ultrafast OPOs. Ganikhanov's OPO source is elegantly simple; the two beams are spatially and temporally overlapped when they exit the OPO and can be coupled directly into a microscope, obviating the need for an optical delay line. Unfortunately the output wavelengths from the OPO are further into the infrared (900–1300 nm) than ideal, reducing the spatial resolution and requiring major modification to commercial microscopes to accommodate the long wavelengths. At Raman shifts below 1600 cm^{-1} the CARS signal is above 850 nm, pushing it into a spectral region problematic for photomultiplier detectors. To work around some of these difficulties a subsequent development of the source included the option to use the fundamental wavelength of the Nd:YVO_4 laser at 1064 nm, illustrated by the dashed line in Figure 2.4(C), as an alternative shorter-wavelength source for the Stokes [30]. When mixed with the pump wavelength from the OPO output this gave improved resolution and better access to the fingerprint region. However, this modification reinstates the practical complexities of maintaining spatial and temporal overlap between the two beams, including the need for an optical delay line. Extensive automation could make this system more practical; at the time of writing, a commercial version of this light source is under development (picoEmerald, Angewandte Physik und Elektronik [31]).

The cost and complexity of the sources described so far have been the main obstacle to the widespread adoption of CARS microscopy. Accordingly extensive effort has been made

in searching for simpler, more affordable lasers. A variety of solutions have been proposed. Silberberg et al. [32] synthesized the pump and Stokes wavelengths from a single femtosecond pulse using pulse-shaping techniques on a spatial light modulator. However the accessible Raman shifts were limited by the available spectral bandwidth in the pulse (around $800\,\mathrm{cm}^{-1}$). Andresen et al. [33] demonstrated the implementation of CARS microspectroscopy (see Section 2.4.2) with a single-laser source and a nonlinear optical fibre. A femtosecond Ti:sapphire laser was used to provide the pump frequency, whilst part of the beam was frequency-shifted with a short length of photonic crystal fibre to produce the Stokes frequency. This scheme is illustrated in Figure 2.4(D). Generally, the magnitude of the wavelength shift in a nonlinear fibre can be controlled by varying the input power, providing the tuning capability in this type of set-up. The same group later implemented CARS microspectroscopy with a fibre laser providing both the pump and Stokes frequencies, again by exploiting the frequency-shifting properties of nonlinear fibres [34]. Very recently, Pegoraro et al. [35] demonstrated CARS imaging using a light source based only on fibre components. An all-fibre light source holds the promise of developing into a low-cost and alignment-free laser that can be fitted onto existing confocal or two-photon microscopes. As yet these sources are not sufficiently robust for reliable imaging but are likely to become the lasers of choice in the near future. For the time being, most applications of CARS continue to rely on 'big' laser systems.

2.3.3 Microscope

Whilst the laser source is the defining feature of a CARS imaging system, the microscope is largely similar to a standard confocal or two-photon set-up and most CARS imaging systems are based around such commercial systems. The background information on laser scanning microscopes will not be given here, but is covered in detail by Pawley [36]. This section will restrict the discussion to the aspects of the design and use of the microscope that are distinct to CARS by comparison with more standard techniques.

Resolution

The resolution of a microscope is usually specified by the Rayleigh condition [1]. This is the closest that two incoherently emitting point sources can be whilst remaining distinguishable. The resolution r depends on the wavelength of the illumination λ and the numerical aperture of the objective lens $\mathrm{NA}_{\mathrm{obj}}$

$$r = \frac{0.61\lambda}{\mathrm{NA}_{\mathrm{obj}}} \tag{2.13}$$

In confocal microscopy the resolution can be slightly enhanced by placing a pinhole (of correct diameter) in front of the detector. The combination of point-like illumination and point-like detection leads to an improvement in the resolution [37]

$$r_{\text{confocal}} = \frac{0.61\lambda}{\sqrt{2}\text{NA}_{\text{obj}}} \tag{2.14}$$

This resolution enhancement is also realized in two-photon microscopy (without a pinhole). As the excitation of fluorescent molecules depends quadratically on the beam intensity the spatial width of the excitation is narrower than the intensity [38]. Similarly, in CARS microscopy the same resolution enhancement occurs due to the quadratic dependence of the signal on the number of vibrational modes [39]. CARS therefore provides resolution comparable to that of confocal and two-photon microscopes.

Wavelengths

CARS excitation involves two different wavelengths, the pump and Stokes. For effective mixing the two wavelengths must be focused together by a microscope objective lens to create overlapping focal spots. However the presence of any aberrations in the system may cause this overlap of the foci to be less than perfect.

Although the highest-corrected microscope objective lenses are generally corrected for chromatic aberration at 4–5 wavelengths and spherical aberration at 3–4 wavelengths [40] the pump and Stokes wavelengths may lie outwith these values, causing inherent aberrations to become more severe. Longitudinal chromatic aberration in particular is likely to affect the overlap of the two foci [41]. Spherical aberration in the objective lens generally limits the imaging depth that can be achieved in CARS microscopy, although additional correction with adaptive optics can be applied [42]. Note that the CARS signal is usually (though not always) collected by a separate condenser lens. The objective must provide good performance at the pump and Stokes wavelengths, but need not necessarily provide good performance at the signal wavelength. In contrast, in two-photon microscopy the objective also functions as the condenser.

As well as the objective lens, aberrations may result from other lenses in the system. This is particularly true when confocal or two-photon microscopes are used for CARS imaging. Whilst two-photon microscopes are built to accommodate the wavelength range of Ti:sapphire sources (702–925 nm) some modification of the microscope is generally required, either to replace lenses in the laser scanning system or to interface with the more specialized detectors required for CARS (discussed later). Additionally, some of the laser sources outlined in Section 2.3.2 provide longer wavelengths requiring more extensive customization to commercial microscopes [30]. As the transmission of objectives at infrared wavelengths is generally poor [41] this may also be a limitation where available laser power is low.

Very recently the first off-the-shelf CARS microscope (Fluoview FV1000MPE femtoCARS, Olympus) has been developed; however this is a fixed-wavelength system with a limited range of applications. The use of a modified confocal or two-photon microscope provides more flexibility, however some degree of customization is invariably required to accommodate the

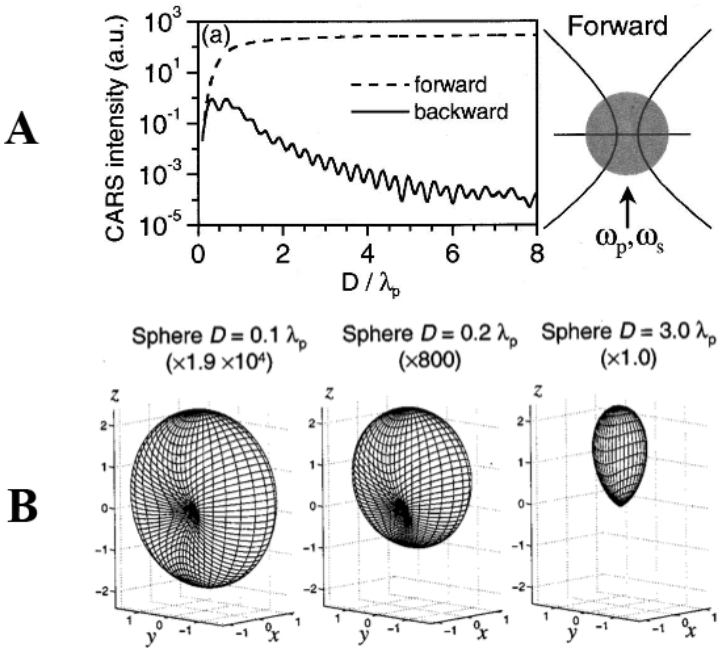

Figure 2.5: Graph of the relative intensities of the forward and backward signals from a spherical scatterer at the focus (A). The horizontal axis is the scatterer's diameter D relative to the pump beam wavelength λ_p. Radiation pattern from spherical scatterers of increasing size (B). This figure is reproduced from Cheng [43].

wavelengths used for CARS. The greatest flexibility is provided by a custom-built microscope (see next chapter), at the expense of the greater complexity and maintenance required of this set-up.

Forward and backward detection

In many imaging techniques, such as confocal and two-photon microscopies, the signal is emitted in all directions and can therefore be most efficiently collected by a lens with a high numerical aperture (NA), usually the same microscope objective lens which focuses the excitation beam. With CARS the signal arises from the coherent superposition of the radiation from all oscillators in the excitation volume. Therefore the signal direction depends on the size (relative to the pump beam wavlength λ_p) and the shape of the scatterer, as well as the nonlinear susceptibilities ($\chi^{(3)}$) of objects in the excitation volume. This gives a strongly directional signal which can be collected in either direction: forward (F-CARS) or backward (E-CARS). The F-CARS signal arises from the constructive interference of the signal from dipoles throughout the excitation volume. The directional nature of this signal means that a standard air condenser provides sufficient numerical aperture to effectively collect the signal. For small (relative to λ_p) objects an E-CARS signal is generated which is collected by the objective lens. However, for larger objects destructive interference causes cancellation of the E-CARS signal. The relative intensities of the two directional signals were calculated by Cheng et al. [43] and are shown in

Figure 2.5 for a spherical scatterer of diameter D.

In experiments a backward signal has been observed through three different mechanisms [5]:

1. Objects of small size ($< \lambda_p/3$) produce a significant E-CARS signal.
2. Sudden discontinuities in $\chi^{(3)}$, such as at the interface of the sample and coverslip, generate a strong E-CARS signal.
3. Thick or turbid samples can cause considerable scattering of the F-CARS signal, some of which will be collected by the objective lens and thus detected in the backward direction.

Where samples are imaged in a medium (typically water) a strong non-resonant signal is generated by the medium. This undergoes constructive interference in the forward direction, and is cancelled by destructive interference in the backward direction. Therefore E-CARS images can provide greater contrast than F-CARS due to the absence of this background. Despite this, in general, the weakness of the E-CARS signal and its size-dependence limit its utility. When imaging thick samples detection in the forward direction is not possible and the backward signal must be recorded. When this is done it is usually the third of the above mechanisms that is responsible for most of the signal [44].

Optical sectioning

The nonlinear nature of CARS and the use of a high-NA objective lens to focus the beams means that excitation only takes place within the focal volume ($< 1\,\mu\mathrm{m}^3$). This gives CARS inherent 3-D optical sectioning capability. As with two-photon microscopy (and unlike confocal) there is no need for a pinhole to block light from out-of-focus planes, and the use of large-area direct (non-descanned) detectors, positioned close to the sample, improves the detection efficiency.

Detectors

Asides from a large active area, the detectors for the CARS signal need a high quantum efficiency across the range of CARS signal wavelengths. Detectors used for confocal microscopy are typically selected for sensitivity to visible-wavelength fluorescence emission, whereas the CARS signal can be visible or near infrared depending on both the specific laser source used and the selected Raman shift (Equation 2.5). For Ti:sapphire lasers the signal (anti-Stokes) wavelength falls in the range 570–$680\,\mathrm{nm}$ and a photomultiplier detector with a photocathode made from multiple alkali metals can provide high detection sensitivity over this range. However these detectors suffer from a sharp infrared cut-off at $850\,\mathrm{nm}$ [45], which limits their application for CARS imaging if using a longer-wavelength laser source.

Image processing

Confocal and multiphoton microscopy make use of deconvolution techniques whereby the recorded pixel values are deconvolved with the measured (or estimated) point-spread function [46]. The coherent nature of CARS in which the signal intensity depends on the interference of the field from oscillators in different parts of the excitation volume means that this cannot be applied. However other 3-D image processing techniques [47], such as volume rendering from optically sectioned stacks, are equally applicable to CARS.

2.4 Techniques

This section will provide an overview of a few of the specific techniques which have been applied to develop, modify or improve CARS microscopy.

2.4.1 Suppression of the nonresonant background

The presence of the nonresonant background is the most significant drawback of CARS and many technical developments have concentrated on addressing this problem.

Polarization CARS (P-CARS) takes advantage of the difference in the polarization between the nonresonant and resonant parts of the signal. First demonstrated for spectroscopy in the 1970s [48], P-CARS has been applied to CARS imaging to effectively suppress the nonresonant background [49]. A half-wave plate is inserted into the Stokes beam to rotate its polarization relative to the pump in order to produce the optimum extinction ratio for the nonresonant background when the signal is detected through an analyzer. However the improved contrast offered by P-CARS comes at the expense of attenuating the resonant signal as well. It is a convenient method to distinguish nonresonant and resonant parts of an image, but is unsuitable for imaging damage-sensitive samples where it is critical to minimize laser power.

The simplest method to identify nonresonant and resonant components is to record images on- and off-resonance and subtract them [50]. This is effective because the resonant part of the CARS signal ($\chi_{\mathrm{R}}^{(3)}$) depends on detuning, whilst the nonresonant part ($\chi_{\mathrm{NR}}^{(3)}$) is essentially spectrally flat (see Equation 2.11 and Figure 2.2). Applying this technique to every recorded CARS image would be tedious. Instead the subtraction can be achieved automatically by modulating the frequency of one of the excitation lasers (typically by around $3\,\mathrm{nm}$) such that the Raman shift moves rapidly on and off the CARS resonance and extracting the background-free CARS signal with a lock-in amplifier on the detector. This technique is known as frequency modulation CARS (FM-CARS) [51]. The implementation requires a total of three synchronized excitation frequencies to be able to perform the modulation. This further complicates the laser source, though recently-developed specialized sources for FM-CARS are making it a more viable option. For example, Saar et al. [7] have implemented an FM-CARS system using an OPO with intracavity wavelength modulation.

Other techniques for background suppression include interferometric methods [52, 53, 54], time-resolved detection [55], and spectral [56] and spatial [57] phase control of the excitation beams. These methods have been widely demonstrated on test samples, but less widely used for biomedical imaging due their relative complexity.

2.4.2 Microspectroscopy

CARS microspectroscopy is the recording of a (CARS) spectrum at a selected point in a microscopic sample; or the recording of one spectrum for every pixel of a microscope image.

Whilst a CARS spectrum can be recorded by step-by-step tuning of the Stokes (or pump) laser [25], this method is time-consuming and only practical over a small spectral region. The development of multiplex CARS (M-CARS) [58] made fast acquisition of CARS spectra possible. In M-CARS, multiple Raman vibrations are excited by a narrowband picosecond pump pulse (around $3\,\mathrm{cm}^{-1}$ spectral bandwidth) and a broadband femtosecond Stokes pulse ($\sim 160\,\mathrm{cm}^{-1}$). The resulting CARS spectrum is recorded with a spectrograph. This method can be used for fast characterization of the chemical properties of samples. Where two Raman bands reside within the spectral bandwidth—which is usually no more than $300\,\mathrm{cm}^{-1}$—it can be used for quantitative imaging by comparing the intensities of different bands. For example, Bonn et al. [59] applied M-CARS for imaging the ratio of two CARS resonances to map out the degree of unsaturation in cellular lipid droplets.

As M-CARS requires a femtosecond pulse and a picosecond pulse it lends itself to the use a laser-and-fibre type source, as illustrated in Figure 2.4(D). The high peak power available in the femtosecond pulse allows easier exploitation of nonlinear effects the fibre. In one such system, demonstrated by Andresen et al. [33], a broadband Stokes pulse was generated by frequency-shifting the femtosecond pump pulse in the fibre. Meanwhile the residual femtosecond pump pulse was spectrally filtered by a separate fibre to provide the required spectral resolution.

Despite the rich chemical information on offer and the relative simplicity of single-laser CARS sources, M-CARS has not enjoyed widespread application for CARS imaging. Acquiring a spectrum at each pixel in an image requires acquisition times of milliseconds per pixel or greater, leading to significant photodamage and resulting in overall image acquisition times that are too slow for many applications in biomedical imaging [5]. Additionally the collected CARS spectra cannot be directly compared with the vast literature on Raman spectra due to the inherent differences between the two (see Section 2.2.3). Whilst Raman spectra can be extracted by a detailed analysis of CARS spectra [60] this requires significant offline processing.

2.4.3 Multimodal microscopy

The combination of CARS microscopy with other better-established nonlinear imaging techniques increases the scope and versatility of CARS imaging. CARS has been combined with fluorescence imaging methods such as two-photon, and with other label-free techniques such

as second and third harmonic generation (SHG, THG) and sum frequency generation (SFG). Where multiple modalities have been combined on the same microscope images may be recorded *sequentially* (i.e. one modality after the other) or *simultaneously*. Simultaneous imaging relies on the ability to physically separate the light from different processes into different detection channels. This is generally achieved by having separate forward and backward detectors and using filters to sort signals by wavelength. Whilst CARS relies on picosecond pulses to maximize contrast in images (Section 2.3.1), femtosecond pulses are preferred for other nonlinear imaging modalities as they maximize the signal generated. Multimodal microscopy inevitably involves a compromise and several different approaches have been taken.

Le et al. [61, 62] combined CARS with both SHG and two-photon imaging by attaching two laser sources to the one microscope. A flip mirror was used to switch between the two, providing sequential imaging. Several applications have used combined CARS and two-photon for simultaneous imaging [63, 64]. For example Nan et al. [24] used CARS to image lipid droplets and simultaneous two-photon to record mitochondria (labelled with MitoTracker Red) in mouse cortical adrenal cells. A pair of synchronized picosecond Ti:sapphire lasers provided the pump and Stokes wavelengths for CARS, whilst the Stokes laser wavelength also excited the fluorescent dye. Energy diagrams for this excitation scheme are shown in Figure 2.1(C) and (D). Using a similar method, Wang et al. [65] demonstrated the application of simultaneous CARS and SFG imaging.

The use of picosecond pulses, whilst advantageous for CARS, results in lower nonlinear signal generation for SFG, SHG and two-photon [66]. Chen et al. [67] reverted to using femtosecond pulses for CARS. Their laser source produced synchronized pulses at four different wavelengths creating a microscope that can perform SHG, THG, two-photon and CARS. The shorter pulses provided enhanced nonlinear signal generation, however the large spectral width of the CARS pulses limited its application to broad Raman bands ($> 50\,\mathrm{cm}^{-1}$). In a recent development, Pegoraro et al. [68] showed that the limited spectral resolution available from femtosecond pulses can be enhanced by controlling the pulse's chirp.

Clearly there is a trade-off between accommodating the different modalities, and the ideal laser configuration has yet to be realized. Nonetheless, multimodal microscopy has already pushed CARS imaging into new areas of application. As many laboratories are already equipped with confocal or two-photon imaging systems, and researchers are often familiar with these methods, the integration of CARS with established techniques—and onto existing microscopes—holds exciting possibilities.

2.5 Applications

CARS microscopy has found applications across a diverse range of research topics. This section will present a brief review of the two that have most benefited: biology and medicine. Despite the limitations of photodamage and the stringent demands of minimizing laser power

these areas have developed rapidly over the past decade. Several applications of CARS imaging to non-living materials, which may have higher damage thresholds, include imaging materials such as photoresists [69] and liquid crystals [70]. This review will concentrate on biological and medical applications as these are most relevant to the application developed for this thesis.

The first tests of CARS microscopy (with a collinear beam geometry) [4, 25] applied the technique to model systems to determine the basic imaging properties, including the contrast, spatial resolution and spectral resolution; and to demonstrate the optical sectioning capability of CARS. Polystyrene beads were extensively used due to the presence of a number of Raman bands which could be targeted [71]. These samples provided the basis for further development of microscope systems to reach a level of refinement suitable for more interesting studies.

Of all the Raman bands that produce useful CARS images the C–H stretch, around $2845\,\mathrm{cm}^{-1}$, is such a strong vibration that the resonant CARS signal is dominant in images, even without subtraction or suppression of the nonresonant background [50]. As lipids contain a high density of these bonds, imaging lipid-rich samples has proved a fruitful area for CARS. In model membrane systems CARS imaging of lipid domains was used to push the sensitivity to a level that can detect single lipid bilayers [72, 64]. In cellular studies, lipid droplets have been shown to provide high contrast in CARS images allowing investigation of their transport and biogenesis [73, 24]. Both fixed and live cells have been studied. Imaging live cells is clearly advantageous as it avoids anomalies introduced by the fixing process [74], although an assessment must be made of the 'safe' power level to ensure photodamage does not occur [24, 75]. The combination of CARS with other label-free techniques, discussed in the previous section, has provided a means to conduct studies into the effects of obesity on cancerous tumours [61] and the composition of atheromata [62]. These studies suggest that CARS may be able to play a role in elucidating the link between obesity and disease, including certain types of cancer and atherosclerosis. CARS also shows promise in the investigation of other diseases. For example, CARS is a good means to image myelin, which is $70\,\%$ lipid. This could assist with the studies of demyelination disorders of the nervous system [76]. As myelin is also present in brain tissue it provides a good target for brain imaging. For example, Evans et al. [30] used a motorized stage to record a mosaic of CARS images showing a full mouse brain section.

The inherent difficulties of fluorescent labelling are compounded when working in the complex *in vivo* environment. There is therefore significant interest using CARS for label-free *in vivo* imaging. By reconstructing stacks of CARS images, Evans et al. [44] created three-dimensional images of mouse skin showing the skin layers to a depth of $100\,\mu\mathrm{m}$. In the same experiment they applied baby oil to the skin and were able to track its diffusion. This could open up new ways to study drug delivery in living systems, especially if methods are used to improve the depth penetration of CARS [42, 77]. More generally, skin is an important medical application for nonlinear microscopy [78] as it is both the largest organ of the body and the most accessible. Imaging other organs requires adapting CARS for endoscopic imaging,

and some progress has been made towards this goal [79]. The use of fibre-based delivery [80] could eventually allow CARS to be used for *in situ* medical diagnosis. Meanwhile improvements in laser sources are making CARS simpler and more cost-effective, opening avenues to new biomedical applications.

2.6 Stimulated Raman scattering

Recently, the drawbacks of CARS microscopy have been addressed by the development of stimulated Raman scattering (SRS) microscopy [6, 81]. SRS is the Raman analogue of stimulated emission. As with CARS, the sample is excited with two frequencies, ω_p and ω_s, arranged such that their difference corresponds to the Raman shift to be imaged, $\Omega = \omega_p - \omega_s$. The amplification of the Raman shift by stimulated Raman gain causes an increase in the intensity of the Stokes beam, and a corresponding loss in intensity of the pump beam. The effect is measured by modulating the intensity of the Stokes beam with an an electro-optic modulator. The modulated loss in the intensity of the pump beam is detected by a lock-in amplifier. (Alternatively the converse effect, stimulated Raman loss, can be measured.)

Unlike CARS, SRS is not afflicted by a nonresonant background, so SRS spectra correspond directly with Raman spectra, allowing the two techniques to be used together more easily and eliminating problems associated with the background. Additionally the signal scales linearly with concentration of sample molecules, improving the sensitivity at low concentrations and making image interpretation easier.

The advantages of this techniques are clear and its initial applications look promising. It remains to be seen whether it will supersede CARS. As both processes use the same frequencies existing microscopes can be adapted to it without replacing the laser source.

2.7 Conclusions

The theory of CARS presented here allows an understanding and interpretation of recorded images. Raman spectroscopy is a valuable tool for selecting target bands for CARS, however there are significant differences between the spectra of the two processes due to the interference of the nonresonant background in CARS. Given the complexity of the light source, laser parameters must be carefully selected to provide good performance of the whole imaging system. When CARS microscopy is implemented with (or added to) a confocal or two-photon microscope some modification is required to accommodate the wavelengths involved in the CARS process, and the directionality of the CARS signal.

CARS microscopy is a rapidly-developing field. Recent developments have focused on finding simpler, more robust laser sources and combining CARS with other nonlinear techniques to improve its versatility. Advances in the implementation of the technique, particularly those related to optical fibres, are reducing cost and complexity, and opening up new biomed-

ical applications. At the same time efforts to address the shortcomings of CARS have resulted in a variety of techniques to suppress the nonresonant background, and the development of stimulated Raman scattering.

3

The CARS microscope

3.1 Introduction

This chapter will describe the set up, operation and testing of the CARS microscope. It will start with a general overview of the complete set-up. The detailed explanation will be divided into two parts: the laser system (Section 3.3) and the microscope system (Section 3.4). The laser system comprises a number of commercial units which will be described only briefly. The microscope system was constructed from components and will be described in greater detail. The operation of the set-up will be explained with particular focus on the unique aspects of CARS microscopy which differentiate it from other techniques. The results of characterization of the microscope's performance will be presented here, including measurement of the spatial resolution. All experiments in this chapter were conducted on test samples, including solvents and polystyrene beads. Chapter 4 will test the microscope's capability for imaging cellular specimens and a specific application will be developed in Chapters 5 and 6.

3.2 Overview

A diagram of the CARS microscope is shown in Figure 3.1; a photograph is shown in Figure 3.2. The pump wavelength λ_p and the Stokes wavelength λ_s are provided by a pair of Ti:sapphire lasers. The pair are powered by a frequency-doubled 10 W Nd:YVO_4 laser (not shown) split fifty-fifty between the two. A portion of each beam is picked off and used to generate a pulse separation error signal between the two lasers which is minimized through a

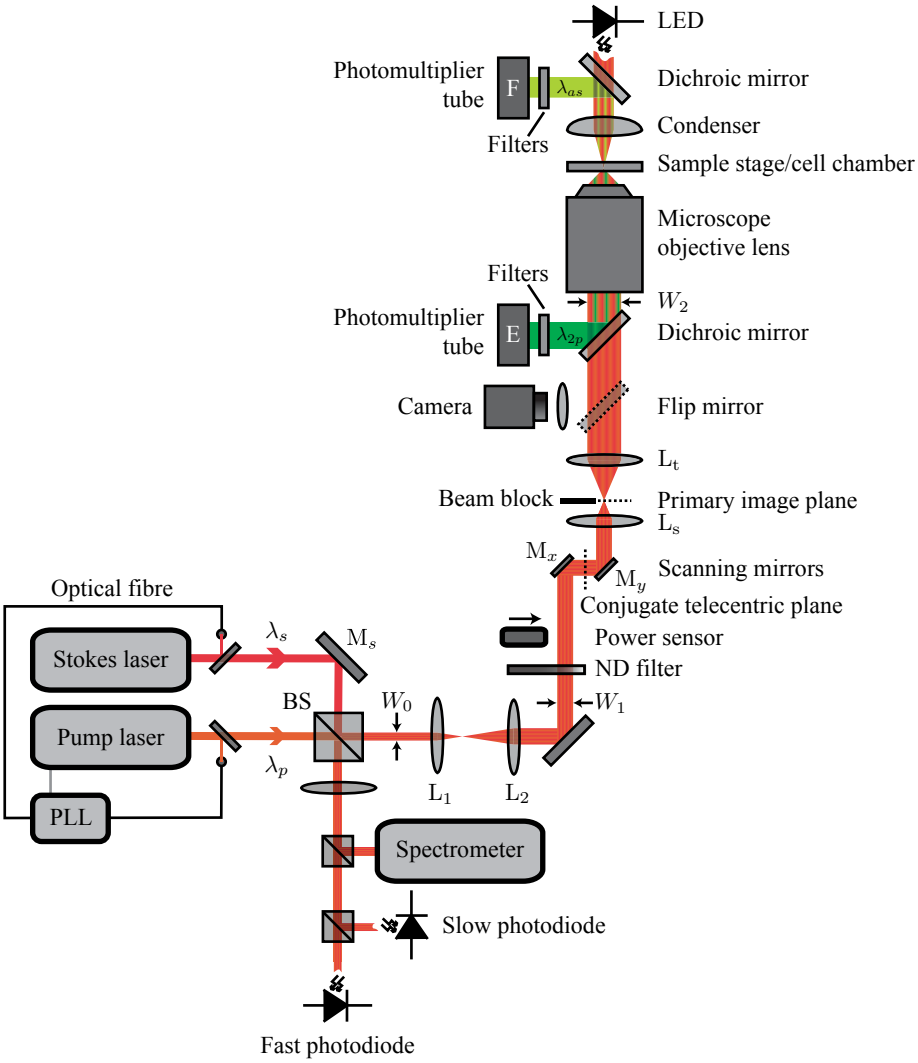

Figure 3.1: Diagram of the CARS microscope. Symbols are defined in Section 3.2. The backward (E) detector was used for detection of the E-CARS signal (not shown) in Section 3.5.8. It was later adapted for detection of a two-photon signal (λ_{2p}), as described in Chapter 5. The cell chamber is an optional addition for live cell imaging and is described in Chapter 6. A photograph of the system is shown in Figure 3.2.

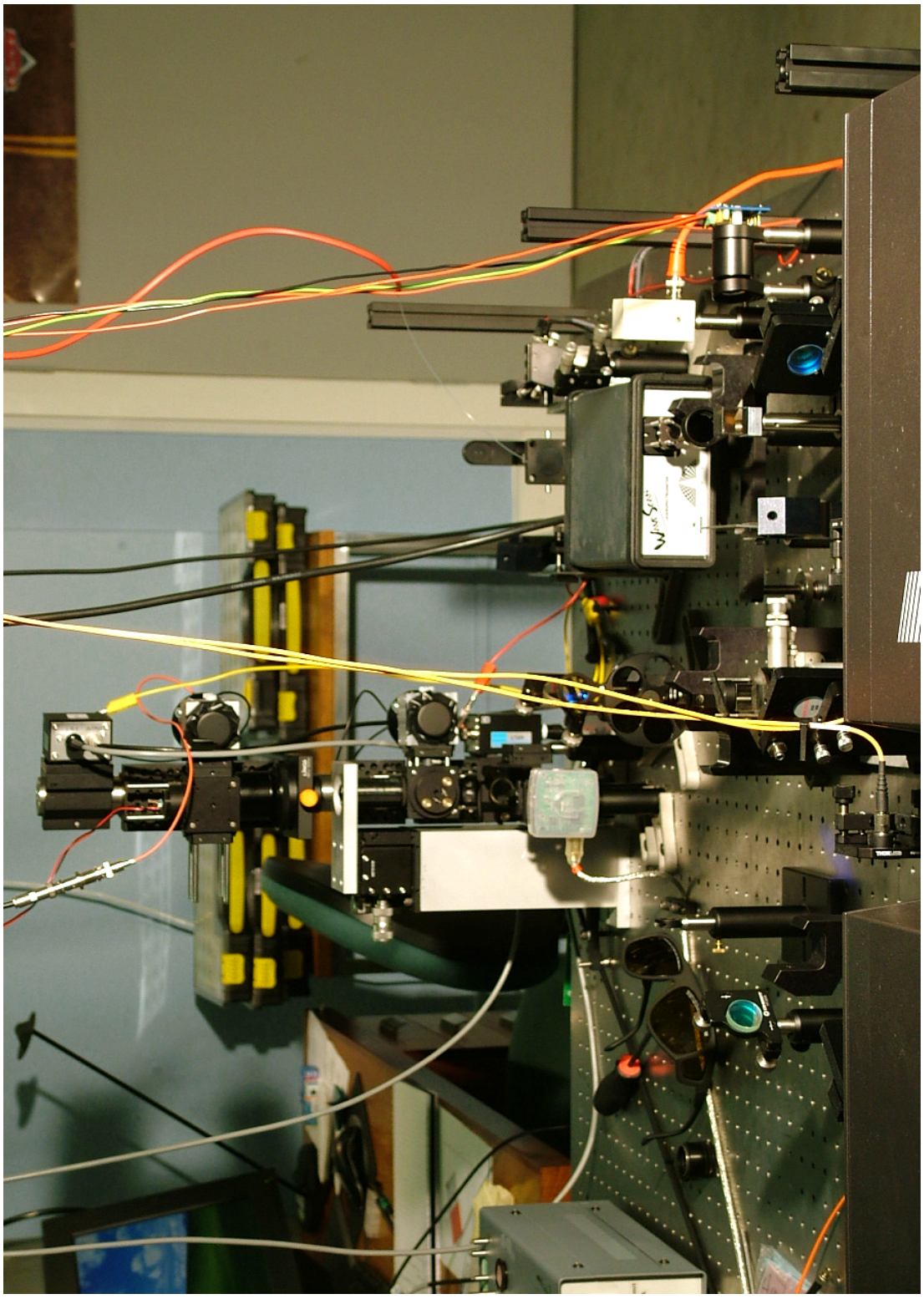

Figure 3.2: Photograph of the CARS microscope.

phase-locked loop system (PLL) keeping the pulses synchronized. The Stokes laser is reflected from mirror M_s into a beam-splitting cube (BS) which combines the two collinearly. Half of this combined beam is used to monitor the laser wavelengths and synchronization, using a spectrometer and two photodiodes. The other half is expanded with a pair of lenses, L_1 and L_2, from a diameter of W_0 to W_1. The beam is attenuated by a variable neutral density (ND) filter and directed onto a pair of galvanometer scanning mirrors, M_x and M_y. Further beam expansion occurs through the scan and tube lenses, $\mathrm{L_s}$ and $\mathrm{L_t}$, to give a beam diameter W_2 at the back aperture of the microscope objective lens. The beam is scanned in the sample plane by driving the scanning mirrors through a computer interface (not shown). The same interface controls the image acquisition.

The CARS signal, with wavelength λ_{as}, is detected with a photomultiplier tube which can be set up for detection in the forward (F) or backward (E) directions. In the forward direction the signal is collected by a condenser lens and in the backward by the microscope objective lens. It is separated from the laser wavelengths by reflection from a long wave pass dichroic mirror and additionally filtered with multiple band pass filters.

For heterogeneous samples bright field imaging is used to identify interesting regions and to focus the sample prior to CARS imaging. Translation and focusing of the sample are performed by a manual three-axis stage. An infrared light-emitting diode (LED) provides illumination through the dichroic mirror and condenser lens. The magnified image is directed from a flip mirror below the objective lens onto a camera.

3.3 The laser system

This section will outline the aspects of the laser system which are specifically relevant to the operation of the CARS microscope. This includes a description of mode-locking, an explanation of the phase-locked loop (PLL) system used for synchronization, and a discussion of how the laser wavelengths are tuned for CARS.

The laser system is based around a number of commercial units manufactured by Coherent. A frequency-doubled Nd:YVO_4 (Verdi V10) powers the pump (Mira 900-D) and Stokes Ti:sapphire lasers (Mira 900-P) and a PLL system (Synchrolock) synchronizes the output pulses. The description given in this section will cover only some aspects of the laser system's capabilities; full technical documentation is provided by the manufacturer [82, 83]. A diagram of the Ti:sapphire laser cavity is shown in Figure 3.3. The devices marked in green are part of the PLL system; they are present in the pump laser, but not the Stokes.

3.3.1 Mode-locking

Both lasers use passive Kerr-lens mode-locking [20]. Self-focusing in the Ti:sapphire crystal due to the optical Kerr effect causes high-intensity pulses to be focused more than continuous wave (c.w.) light. An adjustable slit inserted before the output coupler (at the position shown

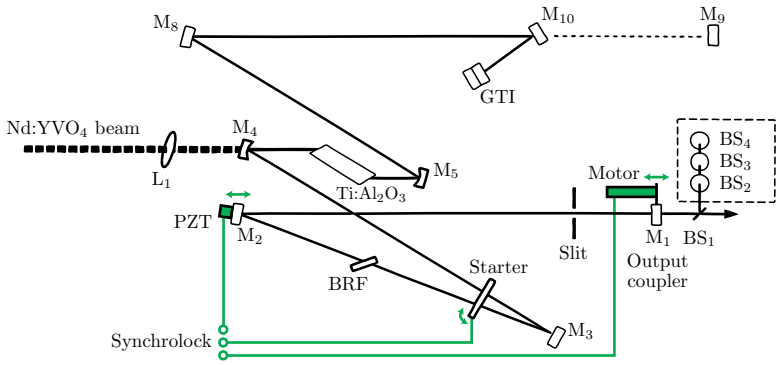

Figure 3.3: The cavity of the pump and Stokes Ti:sapphire (Ti:Al_2O_3) lasers powered by an Nd:YVO_4 laser. Devices marked in green are present in the pump cavity only. Key: M_1 to M_{10} cavity mirrors, GTI Gires–Tournois interferometer, BRF birefringent filter, BS_1 to BS_4 beam-splitters, PZT piezoelectric transducer. This Figure is adapted from the *Mira 900-P Operator's Manual* [82].

in the cavity diagram, Figure 3.3) blocks the c.w. components whilst preferentially transmitting the slightly focused pulses. The alignment of this slit is achieved using a power meter built into the laser head (off BS_3). As Kerr-lens mode-locking employs a passive shutter, the cavity must be momentarily disturbed to initiate the first pulse that will start mode-lock. This is achieved by vibrating a butterfly-shaped *starter*, shown in Figure 3.3, causing a slight but rapid variation in the optical path length of the cavity sufficient to initiate mode-lock. To determine when the cavity has mode-locked a Fabry–Pérot etalon, built into the laser head (off BS_4), detects the presence of any c.w. component in the output beam. The etalon automatically activates the starter whenever c.w. is detected, and switches it off once mode-locking is established. During mode-locking a Gires–Tournis interferometer (GTI) actively compensates for intracavity dispersion [84].

Water absorption is high at certain infrared wavelengths, especially above $870\ \mathrm{nm}$ [85]. The losses can be significant enough to make mode-locking impossible. To minimize the water absorption the cavity humidity can be reduced (to $< 5\ \%$) by purging with dry nitrogen gas for around $1\ \mathrm{h}$ before use.

3.3.2 Synchronization

The CARS process involves the mixing of two different wavelengths, the pump and the Stokes, from pulsed sources. Pulses of each wavelength must therefore arrive in the sample at the same time, requiring careful synchronization of the laser system.

The need for synchronization becomes evident when comparing the pulse separation to the pulse duration. The pulse separation is the time taken for a single pulse to make a round trip of the laser cavity [20]

$$t_{sep} = \frac{2L}{c}$$

where L is the optical path length of the cavity and c is the speed of light. The Ti:sapphire lasers used here both have cavity lengths (and also optical path lengths) of approximately $2\,\mathrm{m}$. This length can be manually adjusted over a limited range by translating the output coupler ($\mathrm{M1}$ in Figure 3.3). The pulse separation is therefore approximately $13\,\mathrm{ns}$. Equivalently, the repetition rate ($1/t_{sep}$) is $75\,\mathrm{MHz}$ which is standard for this type of laser [23]. Pulse durations used for CARS are typically in the range 2–7 ps as this choice maximizes the ratio of the resonant signal to the non-resonant background (see Section 2.3.1). The lasers used here both have pulse durations around $2\,\mathrm{ps}$ (measured later, in Section 3.5.1). The pulse duration is therefore $0.01\,\%$ of the pulse separation. If the pulses derive from independent laser cavities (as in this system[1]) the slightest disturbance to the cavity length of either laser will quickly cause the overlapped pulse trains to walk off from each other. Such disturbances are caused by environmental conditions such as vibrations and temperature changes and are impossible to eliminate completely. To achieve any kind of sustained overlap therefore requires active synchronization.

The techniques for active synchronization of pulsed lasers running at different wavelengths have been developed for a variety of applications, including two-colour pump-probe spectroscopy [86, 87] and difference frequency generation of mid-infrared pulses [88]. The development of CARS microscopy has also motivated improvements to the technique [89]. The general design involves mounting one of the cavity mirrors (usually the output coupler) on a piezoelectric transducer (PZT) in order to control the length of the laser cavity. A feedback loop drives the PZT to synchronize the laser to a stable reference signal, or to another laser.

The system used here is a commercial feedback device (Synchrolock, Coherent) which synchronizes the Stokes laser (the master) to the free-running pump laser (the slave). Mirror $\mathrm{M_2}$ in the pump laser cavity (Figure 3.3) is attached to a PZT to provide precise control of the cavity length. It is important to note that, whilst the PZT must provide nanometre-precision control of the cavity length, the acoustic vibrations which disturb the cavity occur on millisecond timescales [90]. The response speed of the PZT ($200\,\mu\mathrm{s}$ [83]) must therefore be faster than these disturbances, but need not be as fast as the pulse separation ($13\,\mathrm{ns}$).

The PZT provides only a limited range of movement, $8\,\mu\mathrm{m}$. To enable a wider range of adjustment an additional cavity length actuator is also required. The starter is used for this, thus serving dual roles: first in mode-locking (Section 3.3.1) and then in synchronization. This is possible as once mode-locking has been achieved the starter is free to assist in synchronization. Rotating the starter, through a motor drive, changes the optical path length of the laser cavity. It is driven continuously so as to keep the PZT near the centre of its $8\,\mu\mathrm{m}$ range.

[1] In contrast, laser sources in which a portion of a pulsed laser output is used to seed an optical parametric oscillator are inherently synchronized and require only an optical delay line to overlap pulses. This type of source was discussed in Section 2.3.2.

Finally, for the most coarse level of cavity length adjustment, the pump laser's output coupler (M1) is fitted to a stepper motor with $25\,\mathrm{mm}$ of travel. The stepper motor is not part of the active feedback loop; it is used to achieve a rough equalization of cavity lengths before enabling the synchronization system.

The actuators in the pump laser cavity are driven by phase-locked loops (PLLs). A portion of each of the beams is picked off into optical fibres outside the cavity (see Figure 3.1) and detected with fast photodiodes. By electronically mixing the two signals an error signal is generated which contains information about the differences between the lasers' repetition rates as well as the phase relationship between the two pulse trains. The calculation of the error signal is described in detail by Yu et al. [87]. The signal is forced to zero through a PLL at the fundamental frequency of the repetition rate ($75\,\mathrm{MHz}$). To achieve tighter synchronization the system is then switched over to a PLL on the ninth harmonic ($675\,\mathrm{MHz}$) of the repetition rate. The use of higher harmonic locking is an established technique for CARS imaging [89]. The ninth-harmonic lock reduces the jitter to $215\,\mathrm{fs}$ [91] which is sufficient to eliminate jitter noise from CARS images. Methods to measure the timing jitter are described by Ma et al. [26].

To summarize, there are three stages to achieving the synchronization. First the stepper motor is driven to minimize the initial cavity length difference. Then active synchronization is enabled using a PLL on the fundamental frequency of the error signal. Once this has been achieved, a second PLL is switched on operating on the ninth harmonic of the error signal. The fundamental loop is then switched off. This procedure locks the pulse separation and phase relationship between the two lasers. However to ensure overlap in the sample, the phase shift in the *combined* beams must also be adjusted. Whilst this could be achieved with an optical delay line, the PLL includes a phase shifter which allows the addition of an arbitrary phase (0–$360°$) between pulse trains. This final stage of the process requires an external detector to monitor the overlap. It is described later, in Section 3.4.2.

3.3.3 Wavelength tuning

To image a specific vibration the difference in frequency (Ω) between the pump and Stokes lasers must match the energy of the chosen Raman band. Rewriting Equations 2.6 and 2.5 from Chapter 2 in terms of wavelength gives the required condition, and the corresponding wavelength of the CARS signal

$$R = \frac{1}{\lambda_p} - \frac{1}{\lambda_s} \tag{3.1}$$

$$\frac{1}{\lambda_{as}} = \frac{2}{\lambda_p} - \frac{1}{\lambda_s} \tag{3.2}$$

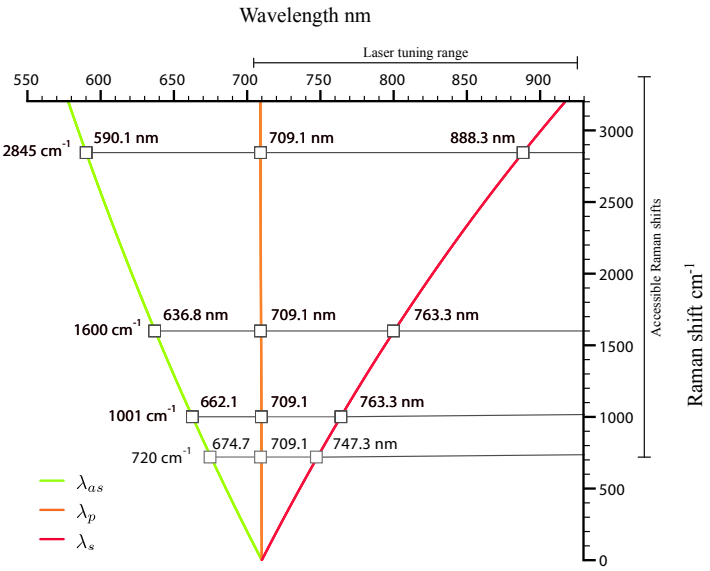

Figure 3.4: Illustration of the relationship between the pump λ_p, Stokes λ_s and CARS λ_{as} wavelengths and the corresponding Raman shift. The pump laser wavelength is fixed near the short wave edge of its tuning range. The maximum accessible Raman shift, $3370\,\mathrm{cm}^{-1}$, is determined by the laser tuning range. The minimum, $720\,\mathrm{cm}^{-1}$, is determined by the properties of the filters used to separate λ_{as} from λ_p, see Section 3.4.6.

where λ_p, λ_s and λ_{as} are the pump, Stokes and CARS wavelengths. The symbol $R = \Omega/2\pi c$ is used here to denote the Raman shift; cm^{-1} is the usual unit[2]. The Ti:sapphire lasers can be tuned over the range 705–$925\,\mathrm{nm}$ by rotating a birefringent filter in the laser cavity (BRF in Figure 3.3). This allows imaging at Raman shifts up to $3370\,\mathrm{cm}^{-1}$. The above equations are illustrated in Figure 3.4 for a fixed pump wavelength of $709.1\,\mathrm{nm}$.

CARS requires very precise tuning of the lasers, especially when targeting a narrow Raman band. Assuming the wavelengths of each laser can be measured with equal precision, i.e. $\Delta\lambda \equiv \Delta\lambda_p = \Delta\lambda_s$, the error in the Raman shift is

$$\Delta R = \sqrt{\frac{1}{\lambda_p^4} + \frac{1}{\lambda_s^4}}\Delta\lambda$$

An external laser spectrometer (WaveScan, Angewandte Physik und Elektronik), positioned as shown in Figure 3.1, was used to measure the laser wavelengths with a specified precision of $0.2\,\mathrm{nm}$. However this precision is not sufficient to tune to the narrow Raman bands in some samples. For example, the width of the ring breathing mode in toluene[3] at $1001\,\mathrm{cm}^{-1}$ is $2\,\mathrm{cm}^{-1}$. When tuning the lasers to this band the error in the Raman shift is $5\,\mathrm{cm}^{-1}$. However, as the spectral bandwidth of the laser pulses (measured in Section 3.5.4) is also around $5\,\mathrm{cm}^{-1}$ the laser tuning is unlikely to miss the band completely and should at least generate a detectable

[2] If λ_p and λ_s are in nm, the Raman shift in cm^{-1} is $10^7\left(\frac{1}{\lambda_p} - \frac{1}{\lambda_s}\right)$

[3] The full Raman spectrum of toluene is shown in Figure 3.10(A).

CARS signal. Once detected the wavelength of one of the lasers can be adjusted slightly, maximizing the CARS signal to ensure they are tuned precisely on the Raman band.

3.4 The microscope system

The microscope system was constructed from a number of components which will be described in this section. The methods of operation will also be detailed here.

3.4.1 Collinear overlap of pump and Stokes beams

The CARS microscope requires the pump and Stokes lasers to be combined collinearly and overlapped. The beam-splitter (BS in Figure 3.1) is mounted on a kinematic stage allowing it to be rotated and tilted with high precision. The pump beam is used as a fixed reference, and the Stokes beam alignment is set up to achieve approximate overlap with the pump when viewed over a distance of around $4\,\mathrm{m}$. This alignment method is sufficient to generate a detectable CARS signal in a solvent such as toluene. Once detected, the signal is progressively optimized by 'walking' the beam between M_s and BS to find the position of optimum overlap.

3.4.2 Detection of synchronization

The PLL system can lock with an arbitrary constant phase shift, $0°$ to $360°$, between the two pulse trains. To determine when the two pulse trains are in phase in the *overlapped* beam, i.e. downstream of the beam-splitter, two photodiodes are set up

- a fast photodiode and
- a slow photodiode

at the positions shown in Figure 3.1.

The fast photodiode, a silicon P-I-N type (818-BB-02, Newport), has a spectral response range of 300–$1100\,\mathrm{nm}$. The rise time, $0.2\,\mathrm{ns}$, is less than the pulse spacing ($13\,\mathrm{ns}$), but greater than the pulse duration ($2\,\mathrm{ps}$). It is therefore fast enough to resolve individual pulses, but not fast enough to completely overlap them. The signal, viewed on an oscilloscope, is shown in Figure 3.5. The phase shift is adjusted through the PLL system to bring the pulses approximately into phase, whereupon a signal is detected on the slow photodiode.

The slow photodiode is a GaAsP type (G1116, Hamamatsu) and has a rise time of $4000\,\mathrm{ns}$. It therefore integrates the signal over several hundred pulses. The photocurrent is converted to a voltage by a transimpedance amplifier (LF351, ST Microelectronics)[4]. The spectral response range is 300–$680\,\mathrm{nm}$. As the pump and Stokes wavelengths both lie outside of this range,

[4]The diagram of the amplifier circuit was provided by Douglas Munro of the School of Physics and Astronomy's Electronics Workshop.

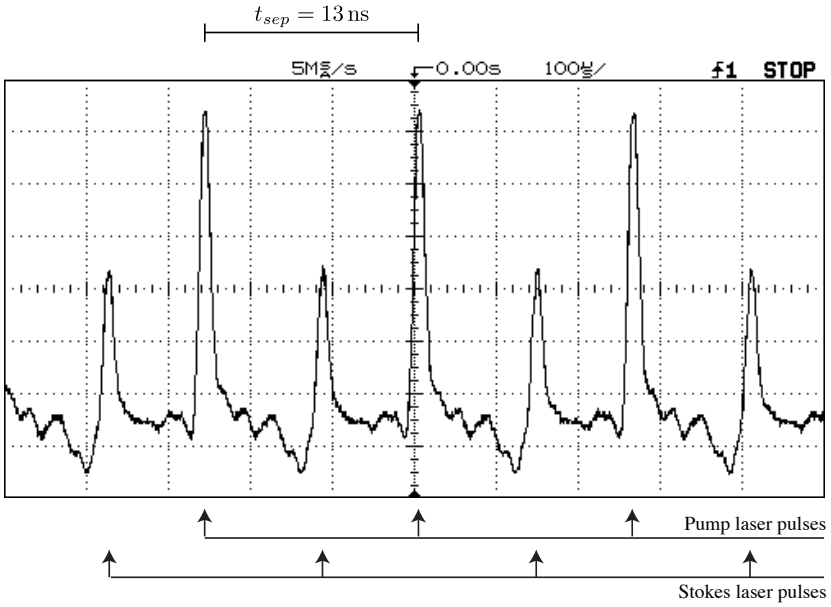

Figure 3.5: Oscilloscope screen showing the signal from the fast photodiode (positioned as shown in Figure 3.1). The pump and Stokes pulses trains shown here are approximately 180° out of phase.

any signal generated is due to multiphoton processes such as two-photon absorption [92]. The signal detected on the photodiode is given by [93]

$$S(\tau) = \int |g_p(t)|^2 \,\mathrm{d}t + \int |g_s(t)|^2 \,\mathrm{d}t + \int g_p(t) \times g_s(t-\tau)\mathrm{d}t$$

where g_p and g_s are the pump and Stokes fields and τ is the (constant) delay between the two pulses. The final term is the cross-correlation between the two beams, with the first two simply adding a constant background to the measurement. The maximum value of the signal therefore occurs when g_p and g_s have the greatest area of overlap, i.e. when $\tau = 0$. This condition occurs when the pulses are completely in phase. The signal can therefore be used to optimize the phase shift to bring it to zero.

To summarize, two photodiodes enable overlap of the beams by adjusting the PLL phase shift between the two. The beams are first brought approximately into phase using the signal on the fast photodiode. The signal from the slow photodiode is then used to fine-tune the phase shift.

3.4.3 Beam expansion

Ideally the light incident on the back aperture of the microscope objective lens will be a collimated beam with uniform intensity across the aperture. To achieve an approximation to this the laser beam, which has a Gaussian intensity profile, must be expanded to fill the aperture. A beam which does not fill the back aperture will not use the full numerical aperture of the lens,

MAG.	MAN.	NA	IMMERSION	BACK APERTURE Ø	RESOLUTION
60x	Nikon	1.20	water	$9.3\,\mathrm{mm}$	$0.26\,\mu\mathrm{m}$
100x	Nikon	1.4	oil	$7.2\,\mathrm{mm}$	$0.22\,\mu\mathrm{m}$

Table 3.1: The microscope objective lenses used for CARS: magnification, manufacturer, numerical aperture, immersion fluid, diameter of the back aperture and the diffraction-limited resolution calculated by Equation 2.14 with a pump wavelength of $709\,\mathrm{nm}$.

resulting in an increased focal spot size and lower resolution.

The diameter of a Gaussian beam is defined as the full width of the intensity profile at $\frac{1}{e^2}$ of the maximum intensity. A common arrangement in confocal microscopes is to expand the beam to twice the diameter of the objective lens back aperture [94]. This arrangement leads to a variation in intensity of $40\,\%$ over the aperture and transmits $70\,\%$ of the incident light into the objective.

In this set-up the beam expansion occurs in two stages, before and after the scanning mirrors (Figure 3.1). Lenses L_1 and L_2 expand the beam width from W_0 to

$$W_1 = \frac{f_2}{f_1} W_0$$

This must be less than $5\,\mathrm{mm}$ to ensure the beams fit onto the scanning mirrors. Further expansion is provided by the scan lens $\mathrm{L_s}$ and tube lens $\mathrm{L_t}$ to give

$$W_2 = \frac{f_t}{f_s} W_1 = \frac{f_t f_2}{f_s f_1} W_0$$

The diameter at L_1 was measured, by scanning a knife-edge across the beam [95], as $W_0 = 2.1\,\mathrm{mm}$. The back aperture diameters of the two objective lenses used in this thesis are listed in Table 3.1. The focal lengths of lenses L_1, L_2 and $\mathrm{L_s}$ were are chosen to overfill the back aperture of the 100x objective lens; the focal length of $\mathrm{L_t}$ is fixed by the objective manufacturer:

First beam expanding lens	f_1	$60\,\mathrm{mm}$
Second beam expanding lens	f_2	$150\,\mathrm{mm}$
Scan lens	f_s	$75\,\mathrm{mm}$
Tube lens	f_t	$200\,\mathrm{mm}$

This gives a final beam diameter of $14\,\mathrm{mm}$. This is ideal for the 100x objective lens, but underexpanded for the 60x. Although a greater beam expansion would provide more even intensity across the objective lens back apertures this can only be achieved by reducing the focal length of the scan lens. In practice this did not lead to any improvement in image quality or resolution. This could be due to aberrations introduced when using a scan lens with a short focal length.

3.4.4 Beam attenuation

A linear gradient ND filter (NDL-25C-4, Thorlabs) was set up to control laser power, as shown in Figure 3.1. The filter allows continuously variable adjustment down to a minimum of $0.01\,\%$ of full power. The power is measured with a thermopile sensor (PowerMax PM3, Coherent) positioned before the scanning mirrors. The power incident on the sample will be lower than the measured power due to losses in the optical system:

- There may be losses in reflection from the scanning mirrors. These are assumed to be negligible.
- There are losses in transmission of the beam through the scan and tube lenses. These are also assumed to be negligible.
- The beam overfills the back aperture of the objective lens. Around $70\,\%$ of the incident beam enters the objective.
- The objective lens has a transmission of approximately $65\,\%$ at infrared wavelengths [96].

As a result of these losses it is estimated that the power at the sample is $46\,\%$ of that incident on the scanning mirrors.

3.4.5 Beam scanning

The scanning mirrors set up for CARS imaging are arranged as a closely-spaced pair, illustrated in Figure 3.6. The microscope system is configured so that the telecentric plane of the microscope objective lens is conjugate to the plane between the mirrors (see Figure 3.1). This arrangement closely approximates telecentricity [94].

The mirrors M_x and M_y are mounted on scanners (6215HSM60, Cambridge Technology). Each scanner has a motor, and a rotary optical encoder which measures the angle of the shaft. The mirror scanners are controlled through two servoamplifier circuits (677215HHJ, Cambridge Technology), one for each mirror, to which *command signals* are applied as voltages. The servo generates an error signal using the feedback from the optical encoder. It then drives the scanner to force the error signal to zero. By applying a pair of time-varying command signals (V_x, V_y) the mirrors can be rotated to scan the beam focus in a raster pattern through the sample plane. The generation of the command signals and the simultaneous acquisition of the photomultiplier signal are performed by a data acquisition device (PCIe-6251, National Instruments) controlled by a computer program[5].

[5]The software is a modified version of *Nonlinear Optical Microscopy Scanning and Imaging System (NOMSIS)*, version 1.9, provided by Anthony Lee of Texas A&M University. Jochen Arlt, from University of Edinburgh, modified the software to acquire data from current mode photomultipliers.

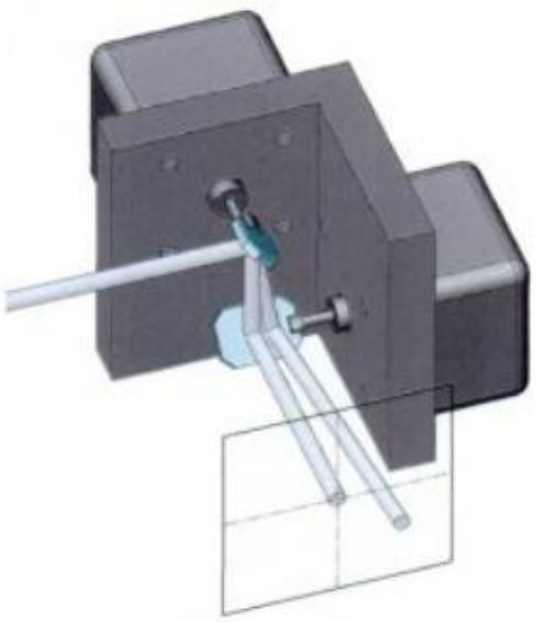

Figure 3.6: An illustration of the scanning mirrors: M_x (upper) and M_y (lower). This figure is reproduced from Stelzer [94].

SCANNING PARAMETERS		EXAMPLE	TYPICAL
Image size	L	$64 \times 64\,\mathrm{pixel}$	$512 \times 512\,\mathrm{pixel}$
Pixel acquisition time	T_p	$40\,\mu\mathrm{s/pixel}$	$40\,\mu\mathrm{s/pixel}$
Line acquisition time	T_l	$2.6\,\mathrm{ms/line}$	$20\,\mathrm{ms/line}$
Image acquisition time	T_i	$164\,\mathrm{ms/scan}$	$10\,\mathrm{s/scan}$
Maximum command signal	V_0	$1.1\,\mathrm{V}$	$0.8\,\mathrm{V}$
Scanning offset	(O_x, O_y)	$(0, 0)\,\mathrm{V}$	$(0.12, -0.08)\,\mathrm{V}$
Park position	(P_x, P_y)	$(2, 0)\,\mathrm{V}$	$(2, 0)\,\mathrm{V}$

Table 3.2: The scanning parameters which determine the image dimensions and the acquisition time. A graph of the mirror scanning functions for the example parameters is shown in Figure 3.7. The typical values are those used for most of the CARS images in this thesis.

The laser beam should not be incident on the sample when not acquiring images. At the end of each scan the beam is moved to a defined park position (P_x, P_y) where it rests on a beam block positioned in the primary image plane, as shown in Figure 3.1.

The absolute value of the maximum command signal voltage applied to the mirrors, V_0, determines the size of the region that will be scanned. As the region is square, this value is the same for both mirrors. It is essential to have a precise knowledge of the size of the scanning region in order to be able to measure the size of objects in images. The relationship between V_0 and the dimensions of the scanning region (in μm) must be measured. The method is given in Section 3.5.6.

The scanning region is divided into $L \times L$ pixels. The pixel acquisition time is T_p. The line and image acquisition times are therefore $T_l = LT_p$ and $T_i = L^2 T_p$. M_x is the *fast* mirror; it

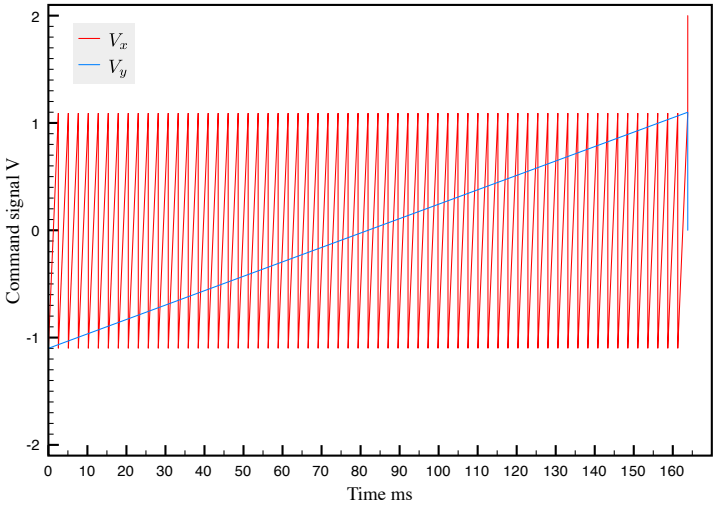

Figure 3.7: The command signals sent to the scanning mirrors to scan a 64×64 pixel image. The scanning parameters are given in the example column of Table 3.2.

scans the beam across each line, then returns to the start position for the next line. Its command signal has the shape of a saw-tooth wave. M_y is the *slow* mirror: it makes one continuous movement for each scan. The following functions are used to calculate the command signal voltages as a function of time t

$$V_x(t) = \begin{cases} 2V_0 \left(\frac{t}{T_l} - \left\lfloor \frac{t}{T_l} \right\rfloor - \frac{1}{2} \right) + O_x & \text{for } 0 \leq t \leq T_i \\ P_x & \text{for } t > T_i \end{cases}$$

$$V_y(t) = \begin{cases} 2V_0 \left(\frac{t}{T_i} - \frac{1}{2} \right) + O_y & \text{for } 0 \leq t \leq T_i \\ P_y & \text{for } t > T_i \end{cases}$$

The values (O_x, O_y) in these functions are a programmable offset which can assist with centering the beam in the sample plane. Some values of the *scanning parameters* to these functions are shown in Table 3.2. The graph in Figure 3.7 shows an example of the command signals used to scan a 64×64 pixel image.

The maximum scanning rate is limited by the response speed of the mirrors. When scanning a saw-tooth pattern the discontinuity in the signal at the end of each line causes M_x to travel back across the line to start the next line. This limits the fastest practical pixel acquisition time to $T_p = 10\,\mu\mathrm{s/pixel}$, which is $T_i = 2.6\,\mathrm{s/scan}$ for a 512×512 pixel image. Faster pixel acquisition times could be achieved by changing the command signal V_x from a saw-tooth wave to a triangle wave. In practice slower scanning rates than this, typically $T_p = 40\,\mu\mathrm{s/pixel}$, were used to minimize visible noise in CARS images.

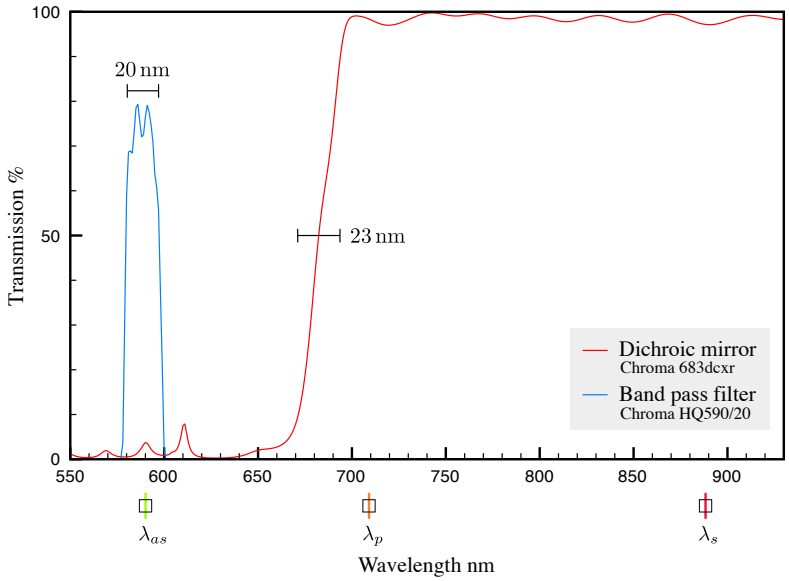

Figure 3.8: Transmissions of dichroic mirrors used to separate the CARS signal, and transmission of the band pass filters used when imaging at $2845\,\mathrm{cm}^{-1}$. Typical pump λ_p, Stokes λ_s and CARS λ_{as} wavelengths are shown. The width of the filter's pass band is $20\,\mathrm{nm}$. The transition width of the dichroic mirror is $23\,\mathrm{nm}$. Data were supplied by the manufacturer [97].

3.4.6 Selection of filters

The CARS signal must be separated from the pump and Stokes wavelengths before detection. This is achieved with filters and dichroic mirrors. In the backward (E) direction the signal is collected by the objective lens, along with some backscattered laser light. In the forward (F) direction the condenser lens collects both the lasers and the CARS signal together. Separation in the forward direction therefore requires more filtering than in the backward.

Two identical long wave pass dichroic mirrors (683dcxr, Chroma) were set up at $45°$, as shown in Figure 3.1, to reflect the CARS signal out of the beam path. A stack of two band pass filters were used to further filter the CARS signal wavelength (λ_{as}). The selection of these filters depends on the wavelength λ_{as} which in turn depends on the Raman shift at which the microscope is operated (Equation 3.2). Therefore different band pass filters were required for each Raman shift. Although in principle short pass filters could be used to cover all Raman shifts, the use of narrow band pass filters helps to eliminate stray light from the photomultiplier tube by restricting the wavelengths that can be detected. Figure 3.8 shows the transmission of the dichroic mirrors, along with the transmission of the band pass filters used for imaging at $2845\,\mathrm{cm}^{-1}$ (HQ590/20, Chroma).

When operating at lower Raman shifts, the pump laser (λ_p) and CARS signal (λ_{as}) wavelengths move closer together (illustrated in Figure 3.4). For example, at $720\,\mathrm{cm}^{-1}$ λ_p and λ_{as} are spectrally separated by only $34\,\mathrm{nm}$. This is close to the practical limit for separating two wavelengths with optical filters. It is therefore the transition widths of the dichroic

mirrors and filters used which determine the smallest Raman shift that can be imaged, whilst the laser tuning range determine the largest (Equation 3.1). Thus the range of accessible Raman shifts for this set-up is 720–3370 cm^{-1}.

3.4.7 Detection and acquisition

The CARS signal is detected by a photomultiplier tube (R3896, Hamamatsu). The tube can be positioned for forward or backward detection, F and E in Figure 3.1. The tube has a multi-alkali photocathode with a high quantum efficiency over the range 250–850 nm, covering the full range of CARS wavelengths. A voltage between 0 and 1250 V can be applied between the anode and cathode. An amplifier with a gain of $10^7\,\mathrm{V/A}$ converts the photocurrent to a voltage. The frequency bandwidth is 200 kHz allowing oversampling by a factor of 2 at the fastest pixel acquisition rate of $10\,\mu\mathrm{s/pixel}$. The amplified signal is digitized by the same data acquisition card (PCIe-6251, National Instruments) that controls the scanning mirrors, allowing the two to be synchronized by an on-board clock. The samples, which are acquired continuously during scanning, are binned and summed to give the intensity value for each pixel. The average of several scans is typically recorded to reduce the effects of noise.

3.4.8 Bright field imaging

Bright field microscopy is the simplest technique for microscopic imaging [1]. For transmission imaging, the sample is illuminated through the condenser. The light is transmitted through the sample and detected with a camera. Contrast is caused by differences in the absorbances of objects in the specimen. Although this contrast is very limited for thin samples, it is generally sufficient to enable alignment, centering and approximate focusing of the sample without the need to expose it to laser radiation. This becomes extremely useful when working with photodamage-sensitive samples as discussed later, in Chapter 6.

In this set-up the sample is illuminated with an infrared LED (L8957, Hamamatsu) with a (peak) wavelength of 870 nm. Infrared light is used as it must be transmitted through two long wave pass dichroic mirrors before reaching the camera (see Figure 3.1). The camera has a silicon charge-coupled device (ICX098BL, Sony) sensitive to this wavelength.

3.5 Testing and characterization

This section describes the testing and characterization of the laser system and the microscope system. These were carried out to assess the performance, to measure important parameters, and to confirm that the detected signal is caused by CARS.

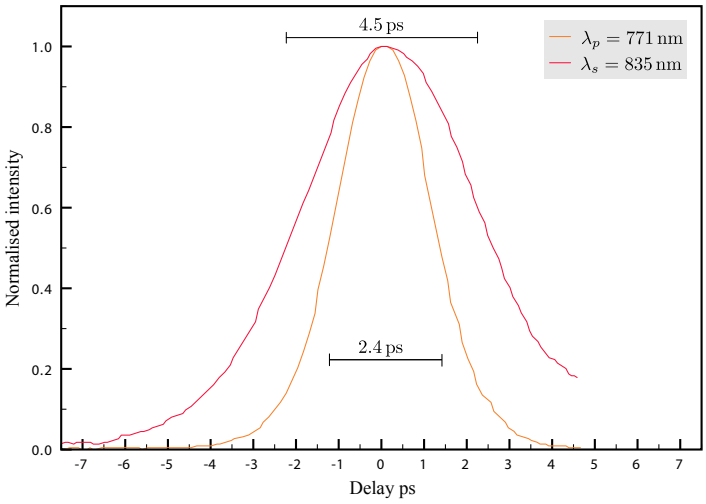

Figure 3.9: Autocorrelation traces at the pump and Stokes laser wavelengths for a Raman shift around $1000\,\mathrm{cm}^{-1}$. The widths (FWHM) of the two traces are shown.

3.5.1 Pulse duration

The pulse duration affects the ratio of resonant CARS signal to nonresonant background as described in Section 2.3.1. The pulse duration of the Ti:sapphire lasers is typically $2\,\mathrm{ps}$, but varies with wavelength. The pump and Stokes lasers were tuned to a Raman shift of around $1000\,\mathrm{cm}^{-1}$ and their respective pulse durations measured with an autocorrelator ('Mini', Angewandte Physik und Elektronik). The two traces are shown in Figure 3.9. Assuming the pulses have sech^2 intensity profiles, the width of the autocorrelation will be larger than the width of the pulses by 1.54 [98]. The pulse durations at 711 and $835\,\mathrm{nm}$ are 1.6 and $2.9\,\mathrm{ps}$. For transform-limited pulses the corresponding spectral widths, given by the time-bandwidth product (Equation 2.12), are $6.6\,\mathrm{cm}^{-1}$ and $3.6\,\mathrm{cm}^{-1}$ respectively.

3.5.2 Raman spectroscopy of test samples

Raman spectra were recorded of several test samples: toluene, dodecane and polystyrene. This information was later used to select target bands for CARS. Although Raman spectroscopy locates the peaks in the vibrational spectra of samples, the Raman and CARS spectra are not identical and the presence of an identified Raman resonance must still be verified with CARS; this test is described later.

A Raman spectrometer (T800, Coderg) was used with the $514.5\,\mathrm{nm}$ line of an argon ion laser as the excitation source. The Raman scattering was collected at right angles to the incident beam. A triple grating monochromator provides high spectral resolution, better than $1\,\mathrm{cm}^{-1}$. A cooled photomultiplier tube with a GaAs photocathode was used as the detector.

Figure 3.10(A) shows a Raman spectrum of toluene. The laser power incident on the sample was $300\,\mathrm{mW}$ and the acquisition time for the complete spectrum was $1.5\,\mathrm{h}$. Tolu-

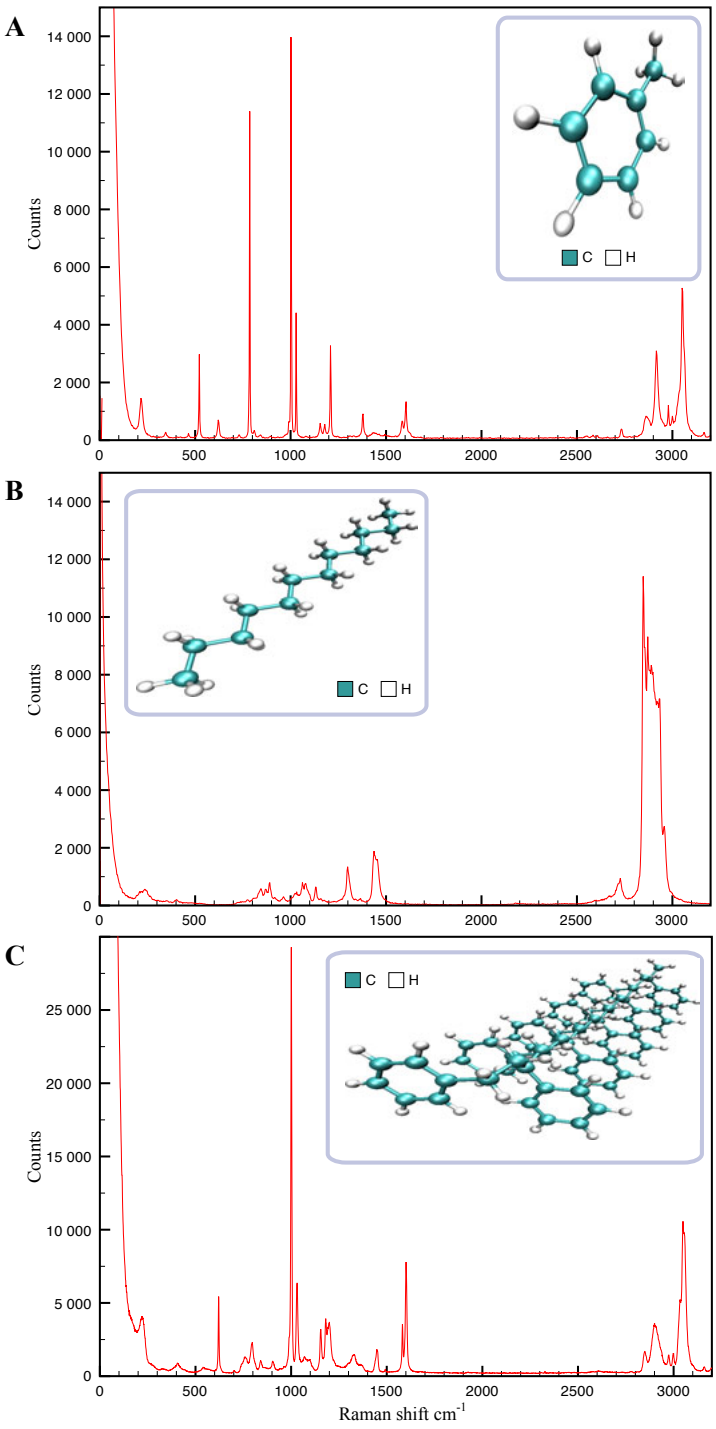

Figure 3.10: Raman spectra of toluene (A), dodecane (B) and (dry) polystyrene (C). The vertical scales are not calibrated, so these spectra cannot be used to compare the strengths of Raman bands between *different* samples.

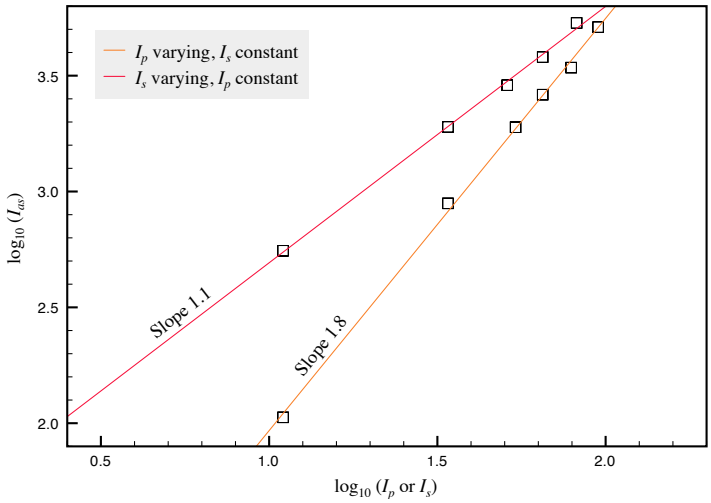

Figure 3.11: Measurement of the dependence of the CARS signal intensity (I_{as}) on the pump and Stokes intensities (I_p and I_s).

ene (C_6H_{12}) is an aromatic hydrocarbon made up of a benzene ring attached to a CH_3 group. All aromatic substances exhibit a strong symmetric ring breathing mode at $1001\,\mathrm{cm}^{-1}$ [9]. The width (FWHM) of this line in the spectrum is $2\,\mathrm{cm}^{-1}$. Toluene is an ideal test sample because a strong (visible) CARS signal can be generated by exciting the ring breathing mode.

The Raman spectrum of dodecane, shown in Figure 3.10(B), indicates a strong peak around $2845\,\mathrm{cm}^{-1}$ due to the large number of C–H bonds in the molecule. The corresponding peak in CARS spectra has been applied for lipid imaging (see Section 2.5) making this sample useful when configuring the microscope for imaging lipids.

The Raman spectrum of a dried sample of polystyrene beads is shown in Figure 3.10(C). Polystyrene beads in water have been extensively used as a test sample for CARS imaging. Two of the bands visible in the spectrum can be used for CARS imaging: at $1600\,\mathrm{cm}^{-1}$ [43] and $2845\,\mathrm{cm}^{-1}$ [99].

3.5.3 Intensity dependence of the CARS signal

The CARS signal intensity I_{as} has the following dependence on the pump and Stokes laser intensities [4]

$$I_{as} \sim I_p^2 I_s \tag{3.3}$$

This relationship was tested to confirm that the detected signal is due to CARS. The signal intensity from dodecane at $2845\,\mathrm{cm}^{-1}$ was measured whilst varying the power of the pump laser with an ND filter. The Stokes laser power was constant. The relative CARS signal intensity was measured by recording the signal level on the photomultiplier tube. The reverse measurement was also made: with a fixed pump power and a varying Stokes power. The results are shown in a log-log plot in Figure 3.11 along with straight line fits to the data. The slopes

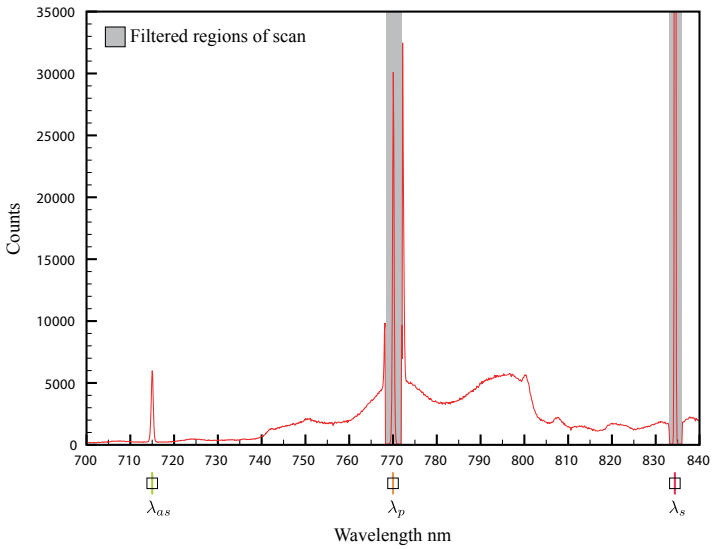

Figure 3.12: Spectrum of the CARS signal from toluene. Filters were inserted when scanning the pump and Stokes wavelengths to avoid saturating the photomultiplier tube.

of the lines are consistent with the given relationship (Equation 3.3), indicating that a CARS signal is being detected.

3.5.4 Spectral resolution

The spectral bandwidths of the pump and Stokes laser pulses were measured along with the wavelength and bandwidth of the CARS signal using the same high-resolution spectrometer (T800, Coderg) described in Section 3.5.2.

A sample of toluene was placed on the CARS microscope and the pump and Stokes laser wavelengths were tuned to the ring breathing mode at $1001\,\mathrm{cm}^{-1}$. This band was chosen because its narrow width ($2\,\mathrm{cm}^{-1}$) permits an estimation of the system's spectral resolution. The unfiltered emission from the toluene was collected by the condenser and coupled into an optical fibre with an aspheric lens. The 20-m-long fibre was used to transmit the light to the spectrometer which was situated in a different laboratory. The spectrometer was scanned from 700 to $841\,\mathrm{nm}$. This range includes the pump, Stokes and CARS wavelengths and these peaks are clearly visible in the spectrum, Figure 3.12. To avoid saturating the photomultiplier tube ND filters were inserted when scanning the spectral regions of the pump and Stokes lasers. The measured pump and Stokes laser wavelengths are 770.1 and $834.4\,\mathrm{nm}$. The measured CARS signal wavelength, $715.0\,\mathrm{nm}$, agrees with the value given by Equation 3.2. Other features visible in the spectrum are likely due to wavelength-shifting effects in the optical fibre. An additional spectrum was recorded with the pump and Stokes lasers out of synchronization. This spectrum (not shown) showed no CARS signal, demonstrating that the signal is caused by a frequency mixing process.

The bandwidths (FWHM) of the pump and Stokes lasers determined from the spectrum

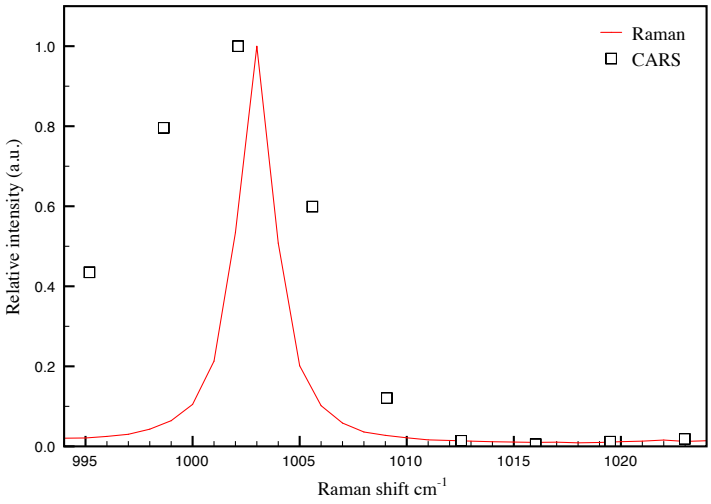

Figure 3.13: Comparison of the Raman and CARS spectra of toluene around the symmetric ring breathing mode at $1001\,\mathrm{cm}^{-1}$. The full Raman spectrum of toluene is shown in Figure 3.10(A). Both spectra are normalized to the height of the peak.

(Figure 3.12) are 6.8 and $4.0\,\mathrm{cm}^{-1}$ respectively. These values are consistent with the bandwidths calculated from measured pulse durations in Section 3.5.1 using the time-bandwidth product (Equation 2.12), indicating that the pulses are near-transform-limited. The bandwidth of the CARS signal, also determined from the spectrum, is $10.4\,\mathrm{cm}^{-1}$ ($5.3\,\mathrm{nm}$). This value gives an estimate of the spectral resolution of the system.

3.5.5 Comparison of CARS and Raman spectra

CARS and Raman excite the same vibrational energies, but are different processes and therefore have different spectra (see Section 2.2.3). The presence of a peak in the Raman spectrum of a sample must therefore also be verified with CARS. To record a full CARS spectrum of a sample would require point-by-point tuning of the lasers over the full range of Raman shifts and this is not practical. Instead, a small part of the CARS spectrum can be recorded by tuning over a few wavenumbers.

Part of the CARS spectrum of toluene was recorded over the spectral region 995–$1023\,\mathrm{cm}^{-1}$. The Stokes laser was tuned to $821.6\,\mathrm{nm}$ whilst the pump laser wavelength was adjusted from to 757.9 to $759.5\,\mathrm{nm}$ in $0.2\,\mathrm{nm}$ steps. The step size was limited by the resolution of the laser spectrometer (see Section 3.3.3). The CARS signal intensity was measured with the photomultiplier tube. The spectrum is shown in Figure 3.13 along with the Raman spectrum of the same region for comparison. The slight variation in laser power with wavelength was corrected by dividing the intensity by the laser powers: $I_p^2 I_s$. The signal with the beams out of phase was also recorded and subtracted to eliminate the effect of any variation in filter transmission with wavelength.

The CARS signal was found to be reduced when the laser wavelengths were moved away

from resonance at $1001\,\mathrm{cm}^{-1}$. As noted in Section 3.5.5, the position of a peak in a CARS spectrum is generally redshifted relative to its Raman equivalent and there is often a sharp dip on the blue side. This dip is evident in Figure 3.13, however it is difficult to determine the presence or absence of the redshift due to the limited precision of wavelength measurements made with the laser spectrometer.

3.5.6 Microscope length scale calibration

The size of the region scanned by the laser beam can be adjusted by setting the maximum command signal voltage V_0, as described in Section 3.4.5. The relationship between this voltage and the dimensions of the scanning region is determined by the following calibration procedure. Once this is known the size and area of objects appearing in images can be measured precisely.

Assuming that the system is telecentric [94], and that the command signal voltage applied to the mirrors results in a proportional angular displacement, the overall size of the (square) image, D, will be proportional to the maximum command signal voltage

$$D = CV_0$$

where C is the length scale calibration constant. To measure C, images of a diffraction grating are recorded over a range of settings for V_0. The number of lines visible in each image N is counted[6]. The image size (in $\mu\mathrm{m}$) can then be determined by multiplying by the grating pitch p

$$D = pN$$

Eliminating D gives

$$N = \frac{C}{p}V_0$$

A graph of N against V_0 should therefore be a straight line with gradient C/p. By imaging a grating with known (or measured) pitch, C can readily be calculated from a linear fit to the measurements. As this calibration constant depends on various aspects of the set-up, including the choice of microscope objective and the focal lengths of other lenses in the microscope system, it must be remeasured after every change in configuration.

Using a diffraction grating with a measured pitch of $p = 25.5(2)\,\mu\mathrm{m}$ the value of C for a 60x water immersion objective (Table 3.1) calculated by a linear fit to the measurements described above is $129(1)\,\mu\mathrm{m/V}$. Nonlinearity of laser scanning, or deviation from telecentricity, would be manifested as geometric distortions (barrel or pincushion) at the edge of images. (Geometric distortion in the objective will also be present but is likely to be less significant.) This was not observed, and the linear relationship between V_0 and D was maintained for image

[6] N is not necessarily a whole number.

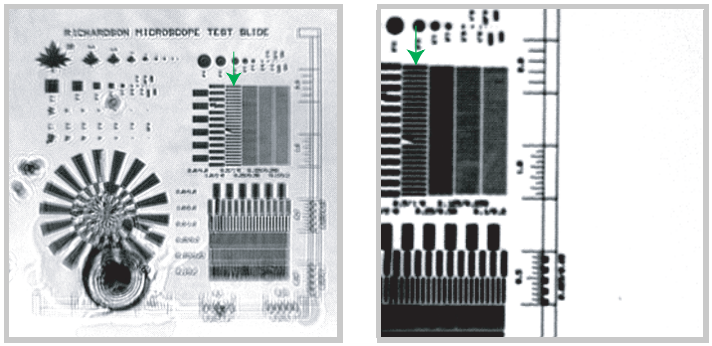

A B

Figure 3.14: A test slide imaged with bright field (A). An image of a small area of the slide was recorded by scanning it with a laser (B). The maximum command voltage was $V_0 = 0.35\,\mathrm{V}$. The image size shown by the 'ruler' is $61 \times 61\,\mu\mathrm{m}$. A 60x microscope water immersion objective lens was used (Table 3.1). The grating with $1.0\,\mu\mathrm{m}$ pitch is marked with a green arrow in both images.

sizes up to $240 \times 240\,\mu\mathrm{m}$.

3.5.7 Spatial resolution

The spatial resolution is the key measure of performance. In a well-configured imaging system the resolution will be close to the diffraction limit. An estimation of the resolution therefore provides a useful measure of the imaging quality. This subsection compares the diffraction-limited resolution with the resolution achieved experimentally. Three imaging methods were tested separately:

1. Bright field imaging: detected by the camera with illumination from the LED.
2. Laser scanning imaging: detected by the photomultiplier tube in the backward direction with illumination from one laser.
3. CARS imaging: detected by the photomultiplier tube in the backward direction with illumination from the pump and Stokes lasers.

For bright field imaging the sample is incoherently illuminated through the condenser lens with an LED. The minimum resolvable distance in the specimen is [1]

$$r_{\mathrm{bf}} = \frac{1.22\lambda_{\mathrm{LED}}}{\mathrm{NA}_{\mathrm{obj}} + \mathrm{NA}_{\mathrm{cond}}}$$

where $\mathrm{NA}_{\mathrm{obj}} = 1.2$ is the numerical aperture of the objective lens (see Table 3.1), $\mathrm{NA}_{\mathrm{cond}} = 0.65$ is the numerical aperture of the condenser lens and $\lambda_{\mathrm{LED}} = 870\,\mathrm{nm}$ is the wavelength of the LED. This gives a diffraction-limited resolution of $r_{\mathrm{bf}} = 0.57\,\mu\mathrm{m}$. The experimental resolution was tested by imaging diffraction gratings of various pitches on a test

slide (Type One, Richardson). Figure 3.14(A) shows a bright field image of the slide. The smallest grating that can be resolved (green arrow) has a pitch of $1.0\,\mu\mathrm{m}$. The adjacent $0.5\,\mu\mathrm{m}$ grating cannot be resolved. This shows that the experimentally realized bright field imaging resolution is in the range 0.5–$1.0\,\mu\mathrm{m}$. As the diffraction-limited resolution lies within this range the image shows that the experimental resolution of bright field imaging is close to the diffraction limit. The resolution of bright field imaging could be improved by using a condenser lens with a higher numerical aperture or a blue LED instead of an infrared one. However such optimizations would have no effect on the resolution of CARS imaging and would be difficult to implement on this set-up.

Laser scanning imaging records the laser light back-reflected from the sample, and can also be applied to image the test slide. The laser power is considerably attenuated and the filters removed from the system to allow the back-reflected laser light to enter the photomultiplier. The diffraction-limited resolution of this imaging method is determined by the wavelength of the coherent illumination λ_{laser} and the numerical aperture of the microscope objective lens $\mathrm{NA}_{\mathrm{obj}}$ (see Equation 2.13 in Section 2.3.3)

$$r_{\mathrm{laser}} = \frac{0.61\lambda_{\mathrm{laser}}}{\mathrm{NA}_{\mathrm{obj}}}$$

With $\lambda_{\mathrm{laser}} = 713\,\mathrm{nm}$ this gives a diffraction-limited resolution of $d = 0.36\,\mu\mathrm{m}$. Figure 3.14(B) shows an image of part of the test slide recorded by laser scanning. As with bright field imaging, the smallest grating which can be resolved has $1.0\,\mu\mathrm{m}$ pitch indicating that the laser scanning system achieves a resolution in the range 0.5–$1.0\,\mu\mathrm{m}$. This shows that the experimental resolution achieved in laser scanning is slightly poorer than the diffraction limit.

For nonlinear microscopy, including CARS, the resolution of point objects is (see Equation 2.14 in Section 2.3.3)

$$r = \frac{0.61\lambda}{\sqrt{2}\mathrm{NA}_{\mathrm{obj}}} \tag{3.4}$$

In CARS, the resolution depends on the *pump* laser wavelength [19]. For $\lambda = \lambda_p = 710\,\mathrm{nm}$ the calculated resolution is $0.26\,\mu\mathrm{m}$.

The experimental resolution for CARS was estimated by imaging titanium dioxide nanopowder according to the method of Chen et al. [67]. TiO_2 has an intrinsically high non-resonant third-order susceptibility producing bright points in images [100]. The nanopowder (677469, Aldrich) has particle sizes less than $0.1\,\mu\mathrm{m}$ and can therefore be used as an approximation to point sources for resolution measurement. A sample of the particles was placed in water and sonicated for $6\,\mathrm{min}$. It was dropped onto a coverslip and dried in a vacuum oven allowing the powder to stick to the glass surface. A drop of water was placed on the coverslip for imaging. The signal from TiO_2 is nonresonant, so should generate a strong signal at any Raman shift. For this measurement the pump laser was tuned to $713.6\,\mathrm{nm}$ and the Stokes to $895.4\,\mathrm{nm}$ to

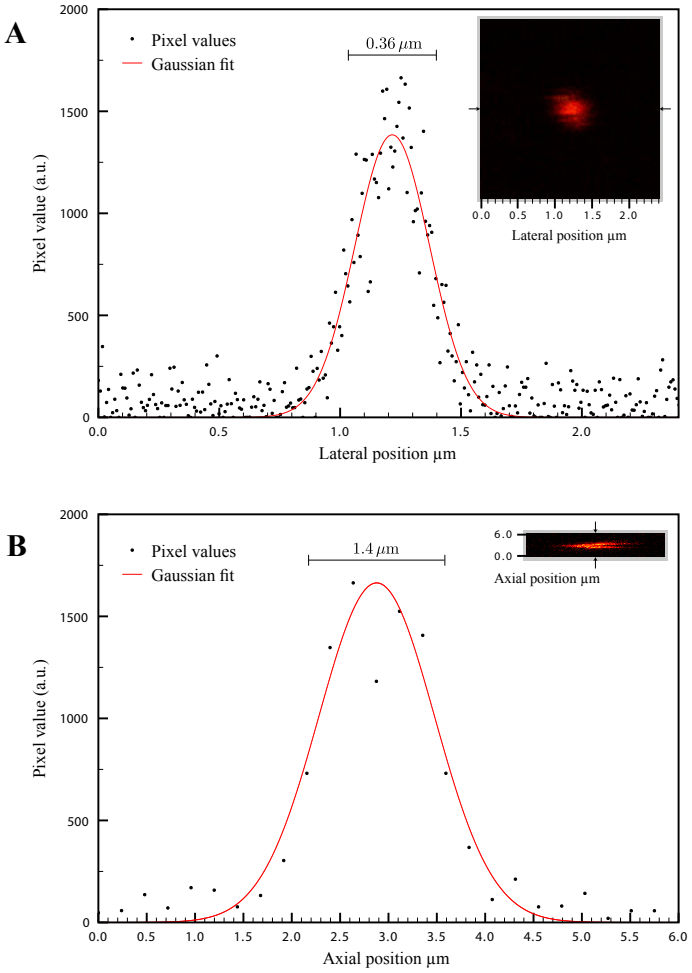

Figure 3.15: Line profiles taken laterally (A) and axially (B) through images of a single nanoscopic particle of titanium dioxide powder. The pixel values are fitted to Gaussian functions. The FWHM of each function provides an estimate of the spatial resolution of the microscope.

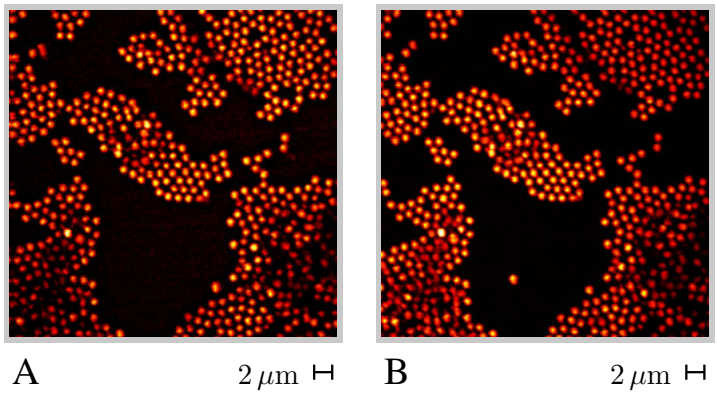

Figure 3.16: CARS images of polystyrene beads in water at $1600\,\mathrm{cm}^{-1}$ (A) and $2845\,\mathrm{cm}^{-1}$ (B). Both images are 512×512 pixels in size and are the average of 4 scans at $11\,\mathrm{s/scan}$. The pump and Stokes laser powers were: both $16\,\mathrm{mW}$ in (A), 15 and $12\,\mathrm{mW}$ in (B).

give a Raman shift of $2845\,\mathrm{cm}^{-1}$. A stack of images was recorded through one particle of the nanopowder by focussing through sample at increasing depths. A differential micrometer on the z axis of the microscope stage (MBT616, Thorlabs) was used to adjust the stage height in $0.25\,\mu\mathrm{m}$ steps.

Figure 3.15(A) shows a graph of a line profile taken laterally through the central slice at the position marked by the arrows on the image (inset). The data are fitted to a Gaussian function. The FWHM of this function, $0.36\,\mu\mathrm{m}$, gives the estimate of the experimental resolution. This is slightly higher than the diffraction-limited resolution calculated by Equation 3.4 and may indicate that further optimization is possible. This value is similar to that reported by Chen et al. [67] ($0.38\,\mu\mathrm{m}$), however their microscope used a longer pump wavelength.

The principal error in the measurement of lateral resolution comes from the uncertainty in the microscope length scale calibration (Section 3.5.6). The error in measuring the size of the particle is estimated at $20\,\mathrm{nm}$. A more precise resolution measurement would require a more precise microscope length scale calibration standard, as well as recording sections through many sub-diffraction sized particles and averaging.

Finally, the axial resolution was also estimated from the recorded image stack. Figure 3.15(B) shows a reconstructed x–z section through the slices. The axial line profile was extracted at the position indicated by the arrows and fitted to a Gaussian function. This gives an estimate of the axial resolution of $1.4\,\mu\mathrm{m}$. The poorer axial resolution (compared to the lateral) is characteristic of most microscope systems as the axial resolution is proportional to $\frac{1}{\mathrm{NA}^2}$ [101]. The error in the axial resolution is due to the limited precision of the stage micrometer, $125\,\mathrm{nm}$. This could be improved with an objective focus motor.

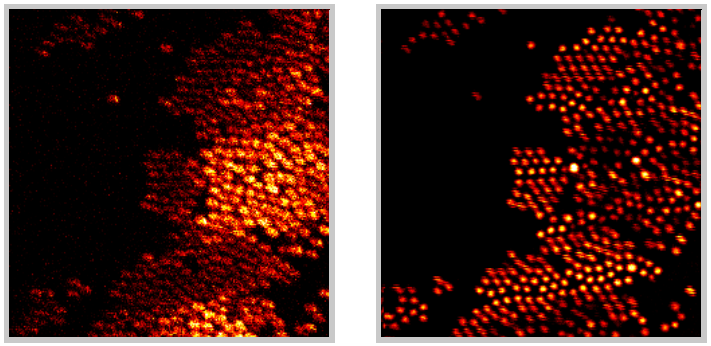

Figure 3.17: E-CARS (A) and F-CARS (B) images of polystyrene beads in water. The images are 256×256 pixels in size. They are the average of 4 scans, at $2.6\,\mathrm{s/scan}$. 600 V was applied to the photomultiplier for the E-CARS image (A). For the F-CARS image (B) this was reduced to 460 V. The laser power incident on the sample was 19 mW.

3.5.8 CARS imaging of polystyrene beads

A sample of polystyrene beads in water was used to test CARS imaging. The average diameter of the beads was determined by light scattering as $1.2\,\mu\mathrm{m}$. A sample of the beads in water was placed on the microscope and allowed to dry out to ensure some beads stick to the coverslip. A drop of water was added for imaging.

Images were recorded at two Raman shifts, 1600 and $2845\,\mathrm{cm}^{-1}$, both shown in the spectrum in Figure 3.10(C). The following wavelengths and band pass filters (Chroma) were used:

Raman shift	R	$1600\,\mathrm{cm}^{-1}$	$2845\,\mathrm{cm}^{-1}$
Pump laser wavlength	λ_p	724.9 nm	712.3 nm
Stokes laser wavelength	λ_s	820.0 nm	893.4 nm
CARS signal wavelength	λ_{as}	649.5 nm	592.2 nm
Filters		HQ650/45	HQ590/20

The images are shown in Figures 3.16(A) and (B). Comparing the two, the image at $1600\,\mathrm{cm}^{-1}$ exhibits a greater background from the surrounding water. This interference likely originates from a broad Raman band in the spectrum of water around $1600\,\mathrm{cm}^{-1}$.

E-CARS images of polystyrene beads were also recorded. Figure 3.17 shows a comparison of E-CARS with F-CARS of the same sample, both recorded at $2845\,\mathrm{cm}^{-1}$. The diameter of the beads is $1.7\lambda_p$, so it is expected that most of the CARS signal will go forward. The E-CARS image (A) therefore produced less CARS signal, and required a higher voltage applied to the photomultiplier resulting in poorer signal-to-noise. Despite this, the signal-to-*background* ratio in the E-CARS image is better than the F-CARS by a factor of 2. This was determined by measuring the intensity in the bead centres and dividing by the average of an area of the water. The absence of the water background generally provides better contrast in E-CARS images. However the low intensity of the E-CARS signal necessitates higher laser powers than F-CARS if excessive noise in images is to be avoided. E-CARS is therefore not well-suited to

biomedical imaging, as discussed later in Chapter 4.

3.6 Conclusions

A signal was detected from toluene at $1001\,\mathrm{cm}^{-1}$ and from dodecane at $2845\,\mathrm{cm}^{-1}$, closely coinciding with peaks in the solvents' Raman spectra. The following tests confirm that the signal is resonant CARS:

- The relationship between the CARS signal wavelength and the pump and Stokes wavelengths is in exact agreement with the calculated value (Section 3.5.4).
- The signal is only present when the pump and Stokes lasers are spatially and temporally overlapped (3.4.1 and 3.5.4).
- The intensity of the signal is proportional to the square of the pump laser intensity and directly proportional to the Stokes laser intensity (3.5.3).
- The signal is significantly reduced when the laser wavelengths are moved away from the resonance (3.5.5).

A laser scanning microscope was constructed to record CARS images. The microscope is capable of recording $512 \times 512\,\mathrm{pixel}$ images at a maximum image acquisition time of $2.6\,\mathrm{s/scan}$. A photomultiplier tube, set up for F-CARS or E-CARS, provides high detection sensitivity across the full range of possible CARS signal wavelengths. The spectral resolution of the system was estimated at $10.4\,\mathrm{cm}^{-1}$, demonstrating the laser system provides the chemical specificity required for contrast in CARS images. The spatial resolution was estimated as $0.36\,\mu\mathrm{m}$ laterally and $1.4\,\mu\mathrm{m}$ axially. The lateral resolution is close to the diffraction limit and similar to values quoted in the CARS literature. The overall performance of the CARS microscope allows its application to study biomedical samples of research interest, which will be the topic of the next chapter.

4

Intracellular imaging with CARS

4.1 Introduction

The previous chapter described the set up and operation of a CARS microscope. The microscope's performance was evaluated by imaging polystyrene beads. In this chapter the system is applied to 'real' specimens—specifically, for imaging lipid droplets in fibroblast cells. The reasons for the choice of this cell type will be explained below. For any biomedical application of CARS imaging the set-up must meet two crucial benchmarks: performance and reliability. The purpose of this chapter is to demonstrate that the system achieves these benchmarks. The next chapter will then apply the microscope for a study of the interactions between a virus and host cells.

Fibroblasts are a type of connective tissue. Their function is to synthesize collagen and other components of the extracellular matrix. Whilst they are interesting from a biomedical perspective—for example, they play an important role in wound healing—they were chosen here because they are one of the most stable cell lines to grow in culture. Their relative 'ease of use' has resulted in their becoming a widely-used cell line for studies in many biological areas [102], including virology [103]. As this cell type is already the subject of active research projects[1], it is an ideal test specimen for the microscope and will readily allow the subsequent application of CARS microscopy for biomedical investigations.

CARS was first applied for imaging fibroblast cells by Cheng et al. in 2002 [39]. Nan et al.

[1]The work described in this chapter and the virological study in Chapter 5 were undertaken in collaboration with the Division of Pathway Medicine at the University of Edinburgh. The cell samples used in this project were grown by Holly Gibbs (Texas A&M University) and Michael Ochsenkühn (University of Edinburgh).

[73] extended this study by, among other results, making a detailed comparison of CARS and fluorescence imaging of cellular lipid droplets. Lipids droplets are a cellular organelle whose primary function is an energy reservoir for the cell. They are composed mainly of neutral lipids and surrounded by a phospholipid monolayer [104]. CARS is the ideal platform for imaging lipid droplets as the high density of C–H bonds produces a strong resonant signal at a Raman shift of $2845\,\mathrm{cm}^{-1}$ [73]. Whilst lipid droplets were once thought of only as a passive energy store, recent evidence suggests they have a diverse range of secondary functions [105]. For example, they carry various proteins, are involved in cellular signaling and play a role in the replication of some viruses—a topic addressed in further detail in Chapter 5.

This chapter will describe the sample preparation procedures, specifically the cell culture methods used, and present the results of a Raman spectroscopic study of the cells. The CARS images presented will demonstrate how both the sample preparation and the microscope system were optimized to achieve the best performance and improve the reliability.

4.2 Background

The theory and background related to CARS microscopy was given in Chapter 2 and the operation of the CARS microscope was explained in Chapter 3. This section will provide a general introduction to cell culture methods in order to provide an understanding of the sample preparation methods used. The explanation given will be an outline only, a comprehensive account can be found in the laboratory manual by Freshney [102].

4.2.1 Cell culture

Cell culture is the growth of cells—animal cells in this case—outside of the organism from which they originate under carefully controlled physiological conditions. Cell culture techniques play a key role in biomedical research, and have important applications in tissue engineering and vaccine production.

The process of laboratory cell culture is illustrated in Figure 4.1. A small number of stock cells are diluted in a medium and seeded into a culture flask. Various media, such as Eagle's [106], have been developed to provide all necessary nutrients for growth. Media usually also contain antibiotics to prevent contamination of cultures with bacterial growth. The physiological conditions of the cells are precisely controlled during incubation to maintain the ideal temperature and pH (37 °C and 7.4 for fibroblasts). Cell cultures can be prepared in two distinct types: as a suspension in the medium, or as monolayer adherent to a substrate (usually glass). The two types of preparation produce cells with very different morphologies. Suspensions of cells adopt a round shape, whilst cells in an adherent monolayer stretch out across the surface and become very flat. The latter is the more commonly used [102] and is the type illustrated in Figure 4.1.

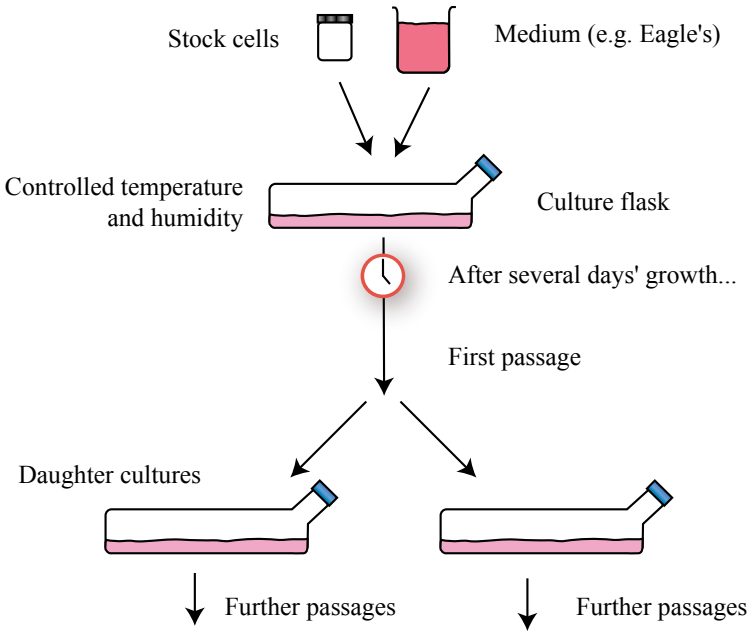

Figure 4.1: Illustration of general cell culture procedure for producing adherent monolayers of cells. The related method for preparation of cells in suspension in media is described by Freshney [102].

During incubation, cells settle and become adherent to the bottom of the culture flask. The cells naturally exhibit contact inhibition and stop growing once the monolayer covers the entire surface area, i.e. when the culture reaches $100\,\%$ *confluency*. At this point cells must be passaged for growth to resume. Passaging involves removing cells from the surface by treatment with trypsin, an enzyme that digests the proteins required for adherence. The detached cells are resuspended in medium and seeded into fresh culture flasks, creating the daughter cultures. The fresh medium added during passaging also keeps the cells nourished. Cells suspensions in medium are passaged in a similar way, with the cells separated from the medium by centrifugation. For both types, cells are routinely counted at each passage by pipetting a small volume of the fluid into a hemocytometer and counting the cells by eye on a low power microscope. This is done to monitor the growth rate and check that the culture remains viable.

The cell samples used in this chapter were fixed before imaging. This allowed optimization of the imaging system without the need to continuously maintain the required physiological conditions on the microscope. An extension of this method to imaging living cells will be described in Chapter 6.

4.3 Methods

4.3.1 Sample preparation

Fibroblast cells were cultured from the 3T3 line [107] in Dulbecco's modification of Eagle's minimum essential medium [102] supplemented with $200\,\mathrm{mol/m^3}$ L-glutamine, $10\,000\,\mathrm{units/mol}$ of penicillin/streptomycin and $10\,\%$ calf serum. They were incubated in *standard conditions*, at a temperature of 37 °C and in a $5\,\%$ CO_2 atmosphere to control pH. Cultures were regularly passaged upon reaching confluency until sufficient cell numbers were grown for the experiment.

For Raman spectroscopy cell samples were grown as a suspension in the medium, then fixed with a solution of $1\,\%$ formaldehyde in phosphate buffered saline (PBS) for $15\,\mathrm{min}$ at room temperature. For most imaging experiments the cells were grown as adherent monolayers. After the final passage they were seeded at $50\,\%$ confluency onto glass coverslips ($22\mathrm{x}50\mathrm{x}0.14\,\mathrm{mm}$) immersed in the medium, and incubated for a further $12\,\mathrm{h}$. The coverslips were then removed from the medium and fixed with formaldehyde solution. They were washed three times with PBS and stored in a fridge at $4\,$°C.

4.3.2 Raman spectroscopy

Raman spectra of cells were recorded[2] with the spectrometer (T800, Coderg) described in Section 3.5.2. An argon ion laser was used as the excitation beam with wavelength $514.5\,\mathrm{nm}$ and power $300\,\mathrm{mW}$. A small fluid volume of cells in suspension in medium was pipetted into an X-ray capillary tube. The thin walls of this container minimize the contribution of the glass to the recorded Raman spectra.

4.3.3 Imaging

The methods for imaging were as described in Chapter 3; a diagram of the setup is shown in Figure 3.1. For most experiments a coverslip of fixed adherent cells was placed on the microscope (which has an inverted configuration) and a drop of PBS added to wet it. Cell selection and coarse focusing were performed by bright field imaging (Section 3.4.8).

4.4 Results

4.4.1 Raman spectra show potential target bands

A Raman spectrum of fibroblast cells in medium is shown in Figure 4.2. This spectrum has not been processed by background subtraction. A large broad band around $3000\,\mathrm{cm^{-1}}$ is therefore present due to water in the medium. The prominent peak near $2900\,\mathrm{cm^{-1}}$ (superimposed on

[2]The Raman spectroscopic study of fibroblast cells was conducted as a master's degree project by Robert Menzies and co-supervised by the author.

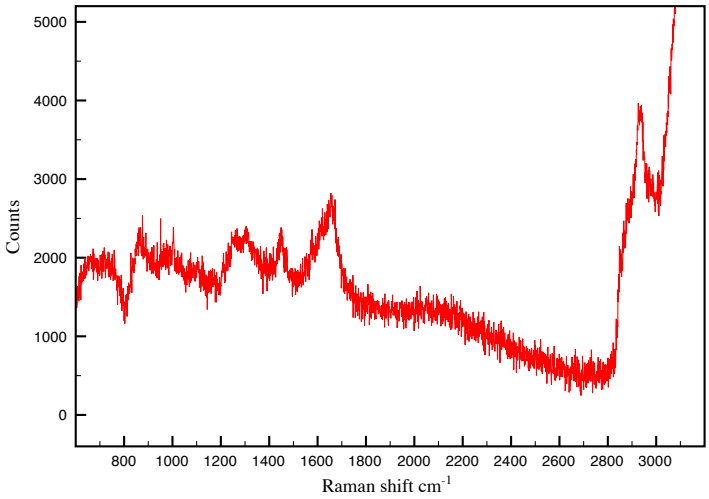

Figure 4.2: Raman spectrum of fixed fibroblast cells in suspension in medium. The water background has not been subtracted. This spectrum was recorded by Robert Menzies [108].

the water band) is due to aliphatic C–H vibrations [39]. This peak was used for all of the CARS images in this chapter.

A systematic study of the Raman spectra of fixed fibroblasts was conducted by Menzies [108]. This study found that the use of a high power argon ion laser for recording the Raman spectra did not cause noticeable damage to fixed cells. Samples imaged by bright field microscopy after Raman spectroscopy showed cell membranes were still intact. Additional processing of the spectra, for example subtracting the background contribution from the suspension medium, revealed the locations of peaks with greater clarity and identified those inherent to the cells and those due to products present in the growth medium such as calf serum. A study by Ochsenkühn et al. [109] used a tweezers Raman spectrometer to record spectra from individual cells, and assigned peaks within the fingerprint region (500–$1800\,\mathrm{cm}^{-1}$).

4.4.2 Adherent monolayers provide clearer CARS images

Cells samples were prepared in two types: as a suspension in the growth medium and as monolayers adherent to a glass surface. Figure 4.3 shows CARS images of each cell type. The different morphologies adopted by the two cell types can be seen in these images.

In general it was found that suspensions of cells, Figure 4.3(A), were problematic for imaging. To confine the medium a small volume of the fluid was sandwiched between a microscope slide and a coverslip, with a thin ($23\,\mu\mathrm{m}$) spacer between the two. However the spherical shape of cells made focusing difficult and their movement inhibited imaging. Additionally there was a strong background from water in the surrounding medium, clearly visible in Figure 4.3(A).

By comparison, imaging of adherent monolayers, Figure 4.3(B), produced clearer CARS images as the stretched morphology adopted by the cells means they are directly adjacent to the coverslip at all points. This resulted in significantly less background signal from the medium.

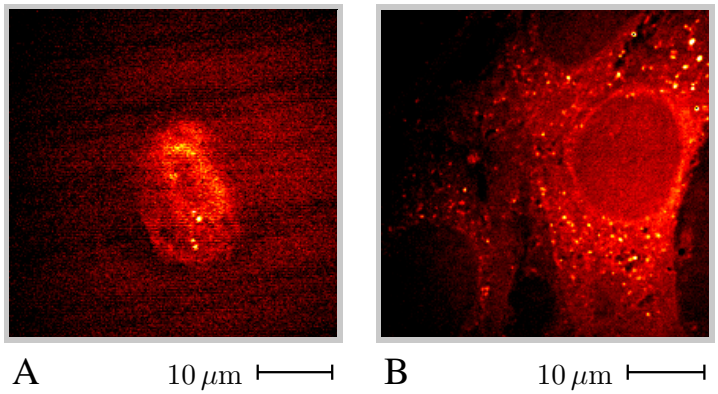

Figure 4.3: F-CARS images of fixed fibroblast cells cultured as a suspension in the medium (A) and as an adherent monolayer on a glass coverslip (B). The pump laser wavlength was 713.3 nm, the Stokes 894.9 nm, giving a Raman shift of 2845 cm^{-1}. The laser power incident on the sample was around 35 mW for both images.

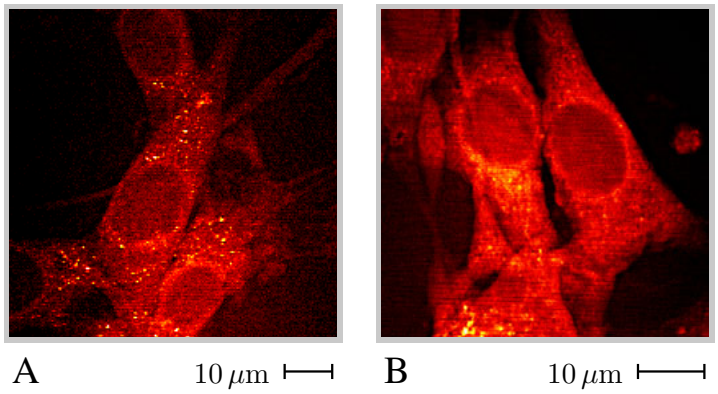

Figure 4.4: Images of different cells within the same sample of fixed fibroblasts recorded at 3 d (A) and 20 d (B) after fixing.

Adherent monolayers were therefore used for all subsequent imaging experiments.

Figure 4.3(B) shows the general features typical of CARS images of fibroblasts recorded at 2845 cm^{-1}. The overall cell shape is triangular, with the nucleus appearing as a dark circular outline, the cytoplasm as a patchy network with a distinct edge at the cell membrane, and lipid droplets as bright points within the cytoplasm.

4.4.3 Fixed samples degrade after several days

It was found that fixed samples suffered from a very limited storage time. Figure 4.4 shows two images of the same sample recorded at 3 d (A) and 20 d (B) after fixing. The comparative lack of contrast in Figure 4.4(B) is due to the absence of lipid droplets. In fact, few clearly-defined lipid droplets were detected anywhere in the sample at 20 d, suggesting that lipid droplets are not preserved by fixing. Further imaging experiments were all performed on samples within three days of fixing in order to avoid this problem.

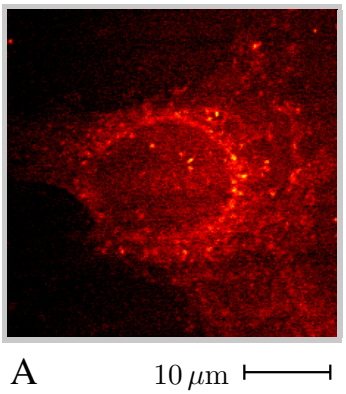

Figure 4.5: E-CARS image of a fixed fibroblast cell. Laser power incident on the sample is around 70 mW.

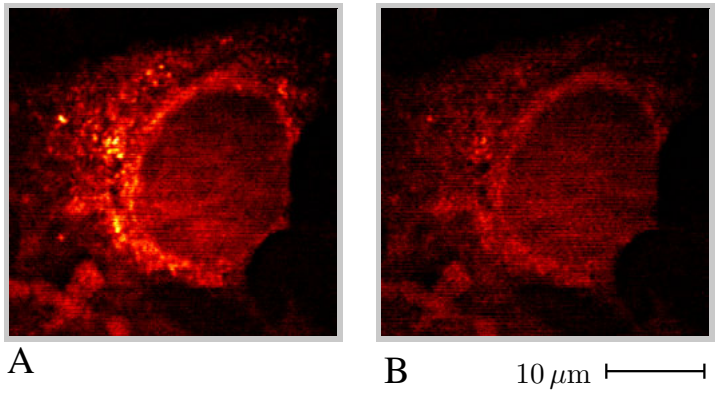

Figure 4.6: F-CARS images of a fixed fibroblast cell recorded on-resonance at $2845\,\mathrm{cm}^{-1}$ (A) and off-resonance at $2895\,\mathrm{cm}^{-1}$ (B). The laser power incident on the sample was 31 mW. A voltage of 444 V was applied to the photomultiplier detector for both images.

4.4.4 E-CARS images require higher laser powers

Images recoded using the backward, E-CARS, signal required a significantly higher laser power than F-CARS to produce images with clearly-defined cellular features. This was due to the reduced signal in the backward direction (see Section 2.3.3). Figure 4.5 shows an E-CARS image of a fibroblast cell. The laser power incident on the sample was estimated at 70 mW, much higher than the ~ 30 mW required for F-CARS images.

4.4.5 Images recorded off-resonance identify the nonresonant background

To interpret images and determine the origin of the detected signal two CARS images of the same cell were recorded at different Raman shifts: on-resonance at $2845\,\mathrm{cm}^{-1}$ and off-resonance at $2895\,\mathrm{cm}^{-1}$. The off-resonance image was recorded by retuning the Stokes laser. The images are shown in Figures 4.6(A) and (B) respectively. The reduced appearance of lipid droplets when moving off-resonance indicates that the signal from the droplets is due to res-

onant CARS. The nonresonant background signal, Figure 4.6(B) reveals the outline of the cell and the nucleus.

There are two reasons why the resonant signal from lipid droplets is substantially brighter the background. Firstly, the C–H stretch vibration at $2845\,\mathrm{cm}^{-1}$ is particularly strong relative to other vibrations (see Raman spectrum in Figure 4.2). Secondly, lipid droplets are solid bodies with a high density of C–H bonds. This gives an enhanced signal due to the quadratic dependence of CARS on the bond concentration (Equation 2.11).

These results are consistent with those of Nan [73] who determined that $2845\,\mathrm{cm}^{-1}$ is the optimum Raman shift for imaging of lipid droplets in fibroblast cells, as it provides the highest signal intensity from the droplets. In the same study, Nan also confirmed that the signal from lipid droplets is resonant by comparing CARS images with P-CARS images (see Section 2.4.1) of the same cells.

4.4.6 CARS imaging provides near-diffraction-limited resolution

Figure 4.7(A) shows a typical fibroblast cell with a large number of lipid droplets visible throughout the cytoplasm. The identifiable cellular features are illustrated in Figure 4.7(B). To estimate the resolution achieved, a smaller region of the same cell was recorded, Figure 4.7(C), by reducing the maximum command signal voltage applied to the scanning mirrors (defined in Section 3.4.5). The size (FWHM) of the smallest lipid droplets visible in this image is $0.36\,\mu\mathrm{m}$. This size coincides with the measured resolution of the microscope determined from images of titanium dioxide nanoparticles (Section 3.5.7). This indicates that the resolution is close to the diffraction limit ($0.26\,\mu\mathrm{m}$) and suggests that at least some of the lipid droplets are sub-diffraction sized, i.e. their actual size is smaller than their apparent size. Figure 4.7(A) also shows the presence of some structure within the nucleus. This may be part of the nonresonant background or could be due to the presence of nuclear lipids [110].

It is likely that some distortion of the microscope focus occurs at the interfaces of lipid droplets due to the refractive index difference between the interior and exterior of the droplet. Whilst there is no obvious manifestation of this in Figure 4.7(C) reports elsewhere have found a dip in signal at the interface of spherical beads [39]. Although the scattering from spherical particles has been extensively studied in confocal microscopy [111, 112] there has been little research on the lens-like behaviour of spherical particles imaged with CARS.

In order to demonstrate the optical sectioning capability of CARS a stack of images was recorded through the cell. 21 images were acquired by successively adjusting the stage height using a differential micrometer in steps of $0.25\,\mu\mathrm{m}$, to a total depth of $5.25\,\mu m$. The stack is shown in Video 4.1. From this stack, the approximate dimensions of the cell were estimated as $20\,\mu\mathrm{m}$ wide by $5.25\,\mu\mathrm{m}$ deep, indicating that it has the thin, stretched shape typical of cells in an adherent monolayer.

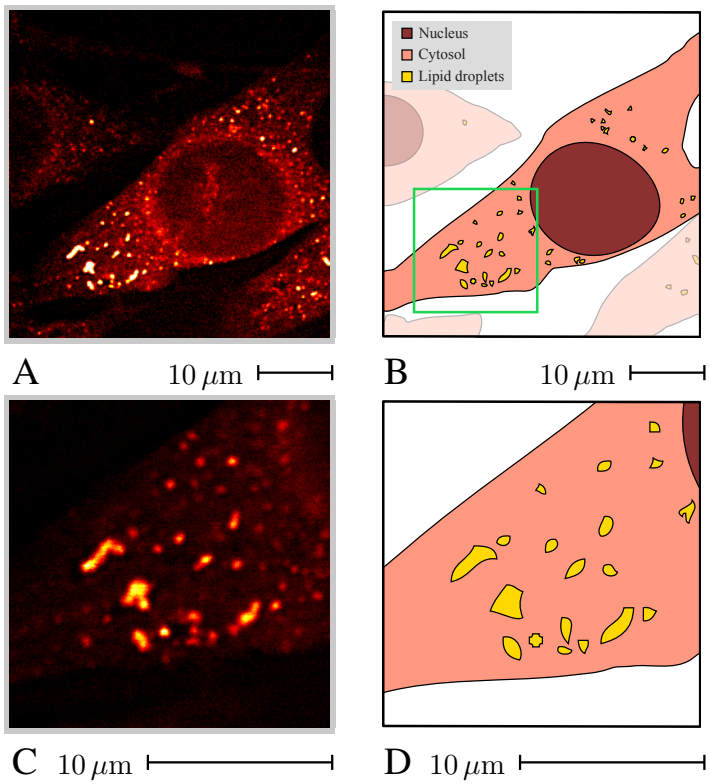

Figure 4.7: F-CARS image of a healthy fibroblast cell (A). The features visible in the image are identified in (B). The area marked by the green square was scanned a second time, producing an image of a smaller region of the cell (C). The pump laser wavelength was $713.8\,\mathrm{nm}$, the Stokes $895.6\,\mathrm{nm}$ giving a Raman shift of $2845\,\mathrm{cm}^{-1}$. A 60x water immersion objective lens was used (see Table 3.1). The laser power incident on the sample was $28\,\mathrm{mW}$ and a voltage of $491\,\mathrm{V}$ was applied to the photomultiplier tube. The pixel acquisition time was $T_p = 40\,\mu\mathrm{s/pixel}$, the image acquisition time was $T_i = 2.6\,\mathrm{s/scan}$ and images are the average of 4 scans. Video 4.1 shows a stack of images through this cell.

4.5 Discussion

The experiments conducted on fibroblast cells were undertaken in order to optimize the performance and reliability of the microscope system. The images presented demonstrate that CARS is the ideal platform for imaging lipid droplets. Whilst the use of fluorescent markers is a widespread technique for generating chemical contrast, such markers are liable to photobleaching and can cause unintended perturbations to specimens. For example, Nile Red and Oil Red O, traditionally used to label lipids, are known to cause lipid droplet deformations [74]. CARS provides the means to image these important organelles avoiding any problems caused by the addition of exogenous fluorophores.

Tuning to the C–H stretch vibration at $2845\,\mathrm{cm}^{-1}$ provided the most favourable ratio of resonant signal to nonresonant background despite the presence of some background signal due to the overlap between the C–H vibration and the much broader water band (see Raman spectrum in Figure 4.2). Imaging at other Raman shifts, especially in the fingerprint region, has the potential to provide additional chemical information, however this was inhibited by the strong background which completely swamped the resonant signal. In these experiments therefore imaging was restricted to the strongest Raman band at $2845\,\mathrm{cm}^{-1}$. The interpretation of images to determine the resonant and nonresonant components revealed a strong resonant signal from lipid droplets. This allows visual interpretation of images without the need for background subtraction. When comparing CARS images, such as these, with those recorded by other modalities it should be noted that the CARS signal intensity depends on the square of the molecular concentration (Equation 2.9).

The degradation of fixed samples after several days limited their utility. The degradation occurs because the formaldehyde used as a fixative cannot enter the dense hydrophobic environment of lipid droplets and therefore does not fix them efficiently [74]. It appears that the lack of complete fixation causes the breakdown of lipid droplets over a period of days. The short storage life of fixed samples severely limits their use as it requires that all sample must be imaged within three days of fixation. This was a motivating factor in the later extension of the microscope system for live cell imaging described in Chapter 6.

Of the two types of cell culture prepared (see Section 4.2.1), adherent monolayers proved to be the more useful for CARS microscopy. Their flatter morphology means that a single image, recorded in a single focal plane, can capture most of the cellular features, as indicated by Figures 4.3(B) and 4.7(A). Whilst CARS microscopy has the ability for optical sectioning (Video 4.1), the thin shape of the cells means this is not generally required, although stack data could for example be used to analyze the volume of lipid droplets with software such as ImageJ [113]. The ability to 'zoom' to recorded regions of interest in greater detail was demonstrated in Figure 4.7(B). However reducing the scanning area increases the intensity and is therefore more likely to cause photodamage. The resolution achieved ($0.36\,\mu\mathrm{m}$) was close to the diffraction limit ($0.26\,\mu\mathrm{m}$) and consistent with values quoted in the CARS literature

($0.30\,\mu\mathrm{m}$ [73]) and the measurement made in the previous chapter (Section 3.5.7).

Whilst E-CARS images in general provide better rejection of background from the solvent or medium (see Section 2.3.3 and also Figure 3.17) the low signal requires higher laser powers to realize sufficient image contrast. Additionally the size-dependence of the E-CARS signal complicates image interpretation as smaller features become unduly prominent. No signs of any photodamage were observed when conducting these experiments. The robustness of these fixed cell samples was also demonstrated during Raman spectroscopy by the lack of cell membrane damage when exposed to a $300\,\mathrm{mW}$ argon ion laser beam for extended periods (Section 4.4.1). Whilst in principle using the maximum available laser power ($\sim 240\,\mathrm{mW}$) for CARS imaging provides the highest contrast in images, such high laser powers introduce other problems. For example, reflections of the laser beams from optical surfaces, including the coverslip, back into the laser cavity caused significant disruption to the laser mode-locking and loss of synchronization. This problem was remedied when the beam was sufficiently attenuated with an ND filter (Figure 3.1) as the back-reflected light is doubly attenuated by this filter (once in each direction). More seriously, a requirement for high laser power would prohibit the extension of the system to live cell imaging. It is therefore desirable to keep the incident laser power at the sample to a minimum. For this reason (and to facilitate the later integration of CARS and two-photon) only F-CARS imaging was used in further experiments.

4.6 Conclusions

It was demonstrated that the performance and reliability of the CARS microscope system achieved a level suitable for its application to biomedical imaging. Adherent monolayers of fibroblast cells provide high quality CARS images revealing cellular features and achieving the expected optical resolution. By comparing CARS images recorded on- and off-resonance the signal from lipid droplets was identified as resonant CARS. A specific application of CARS microscopy, examining virus-host interactions, will be developed in the next chapter.

5

Multimodal imaging of fixed cells

5.1 Introduction

In this chapter a new method for imaging virus-host interactions is established. The method combines two-photon microscopy with CARS in a multimodal imaging system to record the changes in the host cell that occur during infection. CARS imaging at the C–H stretch vibration ($2845\,\mathrm{cm}^{-1}$) is used to reveal the cell morphology and lipid droplet distribution whilst two-photon imaging shows the location and extent of viral protein expression.

The virus used in this study is cytomegalovirus. This is a globally endemic pathogen for which over $40\,\%$ of the world population is seropositive [114]. It is a latent lifelong infection which is usually asymptomatic but can cause acute disease in immunocompromised hosts. For example, it is a cause of sight loss in AIDS patients [115] and can lead to congenital diseases in newborns [116]. It is used in this study as the fibroblast cells described in the previous chapter are permissive to cytomegalovirus infection and carrier cultures can readily be established [114]. The experiments described here were conducted on the mouse strain of the virus, murine cytomegalovirus (MCMV). The restricted host range of this strain means it is safer for use in an optical physics lab, whilst its characteristics are similar to other animal strains, including the human strain [117].

The previous chapter demonstrated that CARS microscopy is the ideal technique for imaging lipid droplets in fibroblast cells. Whilst CARS is a powerful tool for imaging changes in lipid metabolism that occur as a result of infection, it is not sufficient to image lipids alone when studying these processes; observed perturbations to the host cell must be correlated with

the action of the virus. Unfortunately viral particles cannot be imaged directly on a light microscope as their size is below the diffraction limit. However indirect imaging is possible by fluorescence methods, e.g. two-photon [8], and can reveal the subcellular presence of viral particles (but cannot localize them precisely). For example Nan et al. [118] transfected cells with viral ribonucleic acid (RNA) tagged with fluorescin. Using a system which combined simultaneous CARS and two-photon imaging allowed investigation of the apparent stimulation of lipid metabolism caused by the hepatitis C virus (HCV). A recent extension to this study [119] labelled the RNA with the more stable Alexa Fluor 488. However, cells transfected with fluorescently-tagged nucleic acid do not incorporate the fluorophore into progeny. This limits the two-photon imaging capability to the lifetime of the fluorescent RNA, around $6\,\mathrm{h}$ [118], after which the signal fades.

The approach adopted in this study uses a genetic modification to the virus to incorporate the gene for the green fluorescent protein (GFP) [120] into the viral genome. Upon infection the virus initiates the production of the protein by the host cell; alongside the other translated viral proteins. The location and extent of GFP expression can therefore be mapped out with two-photon microscopy whilst CARS shows the host cell morphology and lipid droplet distribution. Use of the modified virus provides a definitive indicator of cell infection. Any GFP expression observed by two-photon imaging must be viral in origin, and therefore indicates that the cell has begun transcribing viral nucleic acid and translating viral proteins. As the modified genome is replicated and incorporated into newly-assembled viruses, the progeny will continue to cause fluorophore expression in subsequent infections. This allows imaging over extended periods post infection without any loss fluorescence.

This chapter will explain the background relevant to this study[1], the methods applied and the results obtained. It forms the basis of the publication in Appendix A. The following section provides a brief outline of the history of virology and highlights the role of light microscopy as a key tool in the science. Cytomegalovirus is a member of the family *Herpesviridae*, and the description of the virus structure and life cycle given in this chapter will be specific to this family. The known host-pathogen interactions for cytomegalovirus will be identified and a more general review of the role of lipid droplets in virus replication will be made. The methods section will briefly outline the sample preparation procedures and describe the extension of the microscope platform for combining two-photon with CARS. The results show the profound effects of the virus on the host cells. An analysis will be given, along with suggestions for the causes of the observed virus-host interactions. Finally, a motivation is presented for extending this study to live cell imaging, which is developed in Chapter 6.

[1]This study was conducted in collaboration with the Division of Pathway Medicine at the University of Edinburgh. The genetically modified virus was provided by Garwin Sing. All cell samples used in this study were prepared by Michael Ochsenkühn.

5.2 Background

This section presents a brief history of virology, assesses the role of light microscopy in this science, and outlines three aspects of viruses: structure, life cycle and the interactions with their hosts. It is intended for a reader familiar with general biology, but less familiar with virology. The description of virus structure and life cycle will relate to the family *Herpesviridae*. Detailed reference material relating to other virus families can be found in the relevant chapters of *Fields Virology* [121]. The methods applied in this chapter combine CARS and two-photon imaging on a multimodal microscope. A review of multimodal microscopy was given in Section 2.4.3. A description the CARS microscope was provided in Chapter 3. As two-photon microscopy is an established imaging technique it will not be explained in detail here; a guide is provided by Denk et al. [8].

5.2.1 History of virology

The scientific study of viruses got off to late start for the simple reason that viruses are too small to be seen with a light microscope, i.e. a microscope which uses propagating light and glass lenses. Although the existence of viruses was hypothesized in the mid-nineteenth century it was not until the 1940s that a significant understanding of these infectious agents emerged [122]. Two developments in particular marked the start of the modern era of virology. Firstly the invention of the electron microscope allowed virus structure to be seen for the first time. Secondly significant advances in cell culture techniques (described in Section 4.2.1) allowed animal viruses to be studied *in vitro* for the first time. Prior to this all studies were conducted *in vivo* and all vaccines were grown in animals or embryonated chicken eggs. In addition to the associated ethical and cost implications, cell samples explanted from animals were not homogenous, leading to poor consistency and reproducibility of results. Among the key developments of the mid-twentieth century were the optimization of the cell growth medium by Eagle [106] and the addition of antibiotics to media which prevented contamination of the cultures. These advances and others were largely motivated by the need to develop new vaccines. This culminated with the development of the polio vaccine in 1952, the first to be grown entirely in cell culture. The second half of the twentieth century has seen important new techniques added to the virological toolkit, including the genetic transformation of viruses and cells. Despite these success there remain many viruses that cannot be propagated in cell culture, significantly hampering research into them [123]. However improved techniques are increasing the range of viruses that can be cultivated *in vitro*. For example, it has recently become possible to establish HCV in cell culture [124], opening unprecedented opportunities for studying it.

The ultimate aim of researching pathogenic viruses is their eradication. This has been successful for smallpox and the end of poliomyelitis is imminent. An understanding of the virus life cycle, and the interactions between the virus and its host organism is crucial to this goal. Antiviral drugs, which target specific points in the life cycle, have been in development since

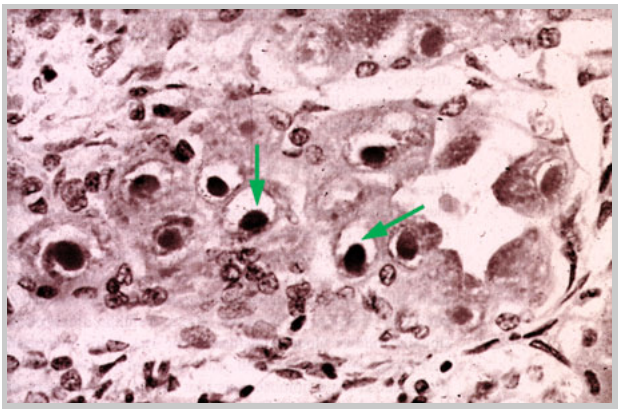

Figure 5.1: Histological image showing the typical "owl's eye" intranuclear inclusions (green arrows) caused by cytomegalovirus. This image is reproduced from Collier and Oxford [125].

the 1960s and have led to effective treatments for a number of infections including, recently, human immunodeficiency virus (HIV). Vaccination programmes have prevented disease by reducing host-to-host transmissions. However, due to their high mutation rate viruses evolve quickly and new viral diseases are often caused by zoonotic infections which jump the species barrier from other animals to humans. These emergent viruses, such as the severe acute respiratory syndrome virus [125], require rapid analysis to develop prevention strategies and treatments. Continuous research on viruses will always be required.

5.2.2 Microscopy in virology

Light microscopy is subject to the diffraction limit, achieving resolution of around $200\,\mathrm{nm}$ at best (see Section 3.5.7). This is not sufficient to observe viruses, which are generally below the diffraction limit[2]. Most of current knowledge about virus structure therefore comes from images recorded by electron microscopy [126], which provides much higher resolution, up to $0.3\,\mathrm{nm}$ [127]. This resolution is sufficient to visualize individual virions, and their detailed structure can be deciphered through studies of many images from the same viral family. Whilst electron microscopy can elucidate the details of viral structure it reveals less about the life cycle. Static images can show the location of the virus in the cell, however electron microscopy cannot image living samples due to the high powers used and the need for staining [128]. It cannot be used to 'watch' viruses in action. Instead the life cycle must be reconstructed by inferring the stages from a series of snapshots and there are often significant gaps in the overall picture.

Although light microscopy cannot image viral particles, the effects of infection on the host—the virus-host interactions—can readily be observed. Bright field microscopy has long been used to identify the *cytopathic effects* which reveal the infection of cultured cells [123]. These effects, though highly virus-specific, have two broad manifestations: a change in cell

[2]The exceptional size of poxviruses, up to $300\,\mathrm{nm}$, allows them to be seen with conventional microscopes.

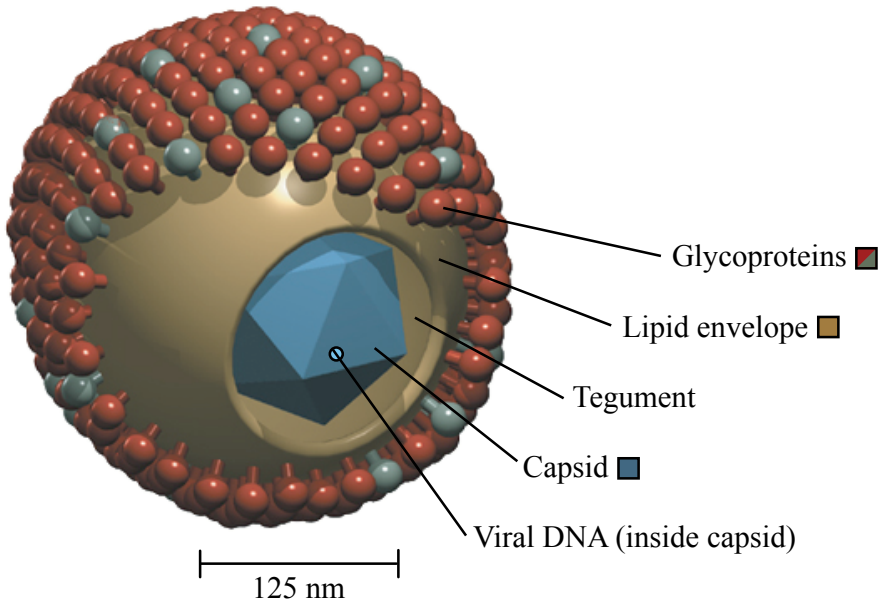

Figure 5.2: Diagram of a herpesvirus. The viral DNA is surrounded by a protective protein shell, the capsid. An amorphous tegument of viral and cellular proteins is enveloped by a lipid layer with protrusions of gylcoproteins. The image was provided by Dr. Marko Reschke.

morphology and the appearance of viral inclusions. Inclusions are regions of foreign material sequestered by the cell in a lipid membrane. For example, cytomegalovirus is named for the enlarged cell effect, *cytomegalia*, which it causes. In the late stage of cell infection typical "owl's eye" inclusions in cell nuclei can be revealed by histological staining [129]. An example is shown in Figure 5.1.

The lack of inherent contrast in bright field microscopy led to the development of laser imaging techniques based on fluorescence [36]. A huge library of fluorescent labels is now available for tracking specific cellular compounds or organelles. The development of various label-free techniques (see Section 2.4.3), including CARS, allow observations of cells under conditions closer to their natural state. Recent advancements in superresolution imaging [37] and single molecule fluorescence [130, 131] have even begun to push microscopy beyond the diffraction limit.

In spite of its limitations then, light microscopy has an important role to play in virology. Advances in microscopy and the development of new techniques continue to improve the chemical selectivity, reduce the invasiveness, add flexibility and enhance the resolution. This progress is critical to provide the tools needed for studying viruses and their pathogenicity.

5.2.3 Structure of viruses

Viruses are macromolecular machines evolved to efficiently transmit the genetic code in their nucleic acid from host cell to host cell. Most viruses are not capable of copying their own

genetic code, and are completely reliant on the machinery of their host for replication. Their small size allows them to more easily take over host cells, but also forces them to adopt a minimalistic structure carrying a small efficient genome sufficient to provide the tools for entering and leaving a cell, but relying on the host for a suitable environment for replication.

The typical herpesvirus is illustrated in Figure 5.2. At its core is the capsid, a protein shell approximately $125\,\mathrm{nm}$ in diameter [132] and highly symmetrical due to the self-assembly method by which it is formed. The capsid encases the viral genome, a linear double-stranded deoxyribonucleic acid (DNA) sequence, which in cytomegaloviruses is approximately $235\,\mathrm{kbp}$ in length encoding around 165 genes [133]. The *nucleocapsid*, i.e. the DNA and capsid together, is surrounded by the tegument, a largely featureless collection of viral proteins that constitutes around $40\,\%$ of the total virion[3] mass. These proteins are ready for immediate use by the virus upon entry into a host cell. They assist in disassembling the virion during cell entry, control transport of the virus through the cell, and aid in managing the host cell environment. The tegument also contains small amounts of RNA of viral or cellular origin. The whole structure is surrounded by a lipid envelope which is ultimately derived from host cell organelles. The surface of this membrane is dotted with numerous protruding glycoproteins which facilitate attachment to and entry through the host cell membrane.

5.2.4 Life cycle of viruses

Herpesviruses have a complex life cycle which is played out in two cellular compartments: the nucleus and the cytoplasm. Whilst many aspects of its replication remain elusive the broad process is understood through studies of the commonalities amongst the various members of the *Herpesviridae* family. A recent review of current knowledge is provided by Mettenleiter et al. [134], which includes the illustration shown in Figure 5.3. The numbered stages in the Figure, (1) to (14), are referred to in the following paragraphs.

The attachment of a virion occurs through the binding of glycoproteins with cell surface receptors (1), though the specific details of this process are poorly understood. Once docked the virion fuses with the cell surface (2) causing removal of the envelope and release of the tegument and nucleocapsid into the cytoplasm (3). The nucleocapsid is transported along microtubules (4) in a journey mediated by tegument proteins. The nucleocapsid docks at a nuclear pore (5) and releases the encased viral DNA into the nucleus. The replication and transcription of viral DNA is performed by the host cell (6). Replication occurs entirely in the nucleus and produces fresh copies of DNA ready for packaging into new viruses. Transcription involves the reading of DNA and the production of messenger RNAs which are exported from the nucleus into the cytoplasm where they are translated to proteins by ribosomes. Viral proteins serve three broad purposes: they assist in replicating the viral genome, they create the structures for packaging the genome and they modulate various host functions to suit the needs of the virus

[3] *Virion* refers to the whole infectious viral particle, including the capsid, the tegument and the envelope. In contrast *virus* may refer only to a part of the virion.

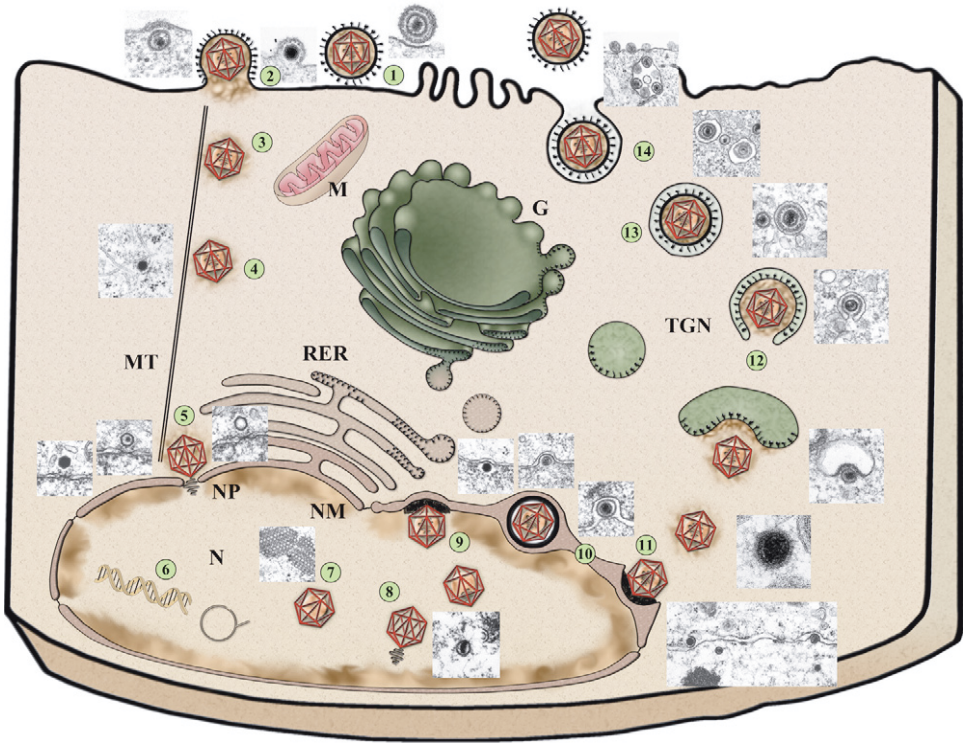

Figure 5.3: Diagram of the herpesvirus life cycle and associated electron microscopy images, reproduced from Mettenleiter [134]. The stages 1–14 are described in the text. The electron microscope images are of the herpesvirus pseudorabies. Key: microtubules (MT), nuclear pore (NP), nucleus (N), nuclear membrane (NM), rough endoplasmic reticulum (RER), mitochondrion (M), Golgi (G), trans-Golgi network (TGN)

[135]. The expression of viral gene products occurs in a cascade of regulated stages throughout the infection cycle. The detailed timing of viral gene expression will not be discussed in detail here, further information is given by Mocarski et al. [114].

Having assumed control of the host cell the assembly of new virions commences. This stage of the cycle begins in the nucleus where capsids self-assemble from viral proteins around a scaffold (7). DNA is packaged into (most of) the capsids to form nucleocapsids (8). These particles must then leave the nucleus to complete their maturation. The process by which they do this has been disputed [132], however it appears that they egress by budding through the two layers of the nuclear membrane [136]. Budding through the inner nuclear membrane (9) leaves the nucleocapsids in the perinuclear space (10). This stage is referred to as *primary envelopment* as they acquire an envelope in the process. This envelope is then lost again by fusion of the particle with the outer nuclear membrane, resulting in the release of the (unenveloped) nucleocapsid into the cytoplasm (11). The addition of proteins to the nucleocapsid occurs in two stages in the cytoplasm, providing the inner tegument and outer tegument. It has been suggested that tegumentation occurs in a viral assembly complex at a specific location within the cytoplasm [137], however this point remains unclear. The secondary envelopment of the virus is thought to occur by budding through vesicles in the trans-Golgi network (12) in a process that wraps the virus in two new layers. Transport to the cell surface occurs by an unknown mechanism (13) followed by fusion of the outer layer with the cell membrane (14). The progeny virus is then released into the intercellular space, ready to infect new cells. The duration of the entire replication process varies between family members: for cytomegalovirus gene expression begins, following a period of latency, at 2–8 hours post infection (hpi) and the first viruses start to leave the cell at 48–72 hpi [114].

The viral assembly process is particularly prone to defects: for example it is estimated that only $1\,\%$ of released cytomegalovirus particles are infectious [114]. A number of the assembled capsids fail to acquire DNA, resulting in viruses that lack the genetic material required for further replication [114]. Additionally, many of the particles lack both DNA and capsid, consisting only of an envelope of proteins [138]. These are termed *dense bodies* and make up the majority of viral particles released by the cell.

5.2.5 Virus-host interactions

To replicate efficiently and produce sufficient progeny to establish further productive infections a virus needs to optimize the host cell environment to suit its requirements. Two general classes of host cell modulation have been identified in cytomegaloviruses: cell cycle disruption and immune response evasion. These will be described below.

Cellular DNA replication does not occur constantly in cells, rather a tightly regulated cell cycle ensures that the process only occurs in the S (synthesis) phase [135]. The result is that the cell produces *exactly one* copy of its genome to prepare it for later mitosis. To ensure efficient replication of the *viral* genome the virus must significantly alter the normal cell cycle

control [139]. It pushes the cell towards the S phase, whilst arresting the normal transition out of the S phase. In this *pseudo-S* state DNA synthesis is stimulated allowing the production of many copies of the viral genome for packaging into progeny. In some cases the cell appears to proceed to a state of *pseudomitosis* [140]. At the same time the virus suppresses the replication of host DNA in order to divert more of the cell's resources to replication of viral DNA.

The virus must also modulate the host environment to evade immune responses if it is to complete its life cycle. This involves disabling cellular alarm signals and suppressing apoptosis (programmed cell death) [141]. Without these interactions immune responses may arrest the virus before it takes full control, or apoptosis would halt the replication process before new virions have completed their maturation.

Recently, it has emerged that some viruses recruit cellular lipid droplets as part of their replication cycle [104, 142]. For example it has been discovered that HCV loads viral proteins onto the surface of lipid droplets during its replication cycle [143]. CARS microscopy, as the ideal technique for lipid droplet imaging, has been applied to study the changes in lipid droplet behaviour of cells transfected with the HCV genome [119, 118] and looks likely to continue to play a key role in these ongoing studies.

5.3 Methods

The detailed method of operation of the CARS microscope was given in Chapter 3. This section will describe the methods specific to preparing the cell samples, and to achieving multimodal microscopy.

Two different strains of the virus were used in this study, which will be referred to as **MCMV** and **MCMV-GFP**. MCMV is derived from the Smith strain, a virus isolated from laboratory mice in 1954 [144]. MCMV-GFP is a version of this same strain which has been modified[4] by integration of a GFP plasmid using the method of Angulo et al. [145].

5.3.1 Sample preparation

Infected cells were prepared under the same conditions as healthy cells described in detail in Section 4.3.1. Solutions of viral particles (MCMV or MCMV-GFP) were diluted in medium to give a multiplicity of infection of 1, and added to culture flasks during the seeding step. Immediately after seeding, the cells were synchronized by storing them for $1\,\mathrm{h}$ at $4\,^{\circ}\mathrm{C}$. This synchronization step allows virions to settle onto the surface of cells without entering. The cells were then placed in an incubator in standard conditions, allowing viral entry to commence and ensuring that the start of the infection cycle is synchronized across the majority of cells. Cell infection was allowed to proceed for $48\,\mathrm{h}$ after which cells were fixed and stored, as described

[4]The genetically modified virus was prepared at the Division of Pathway Medicine at the University of Edinburgh.

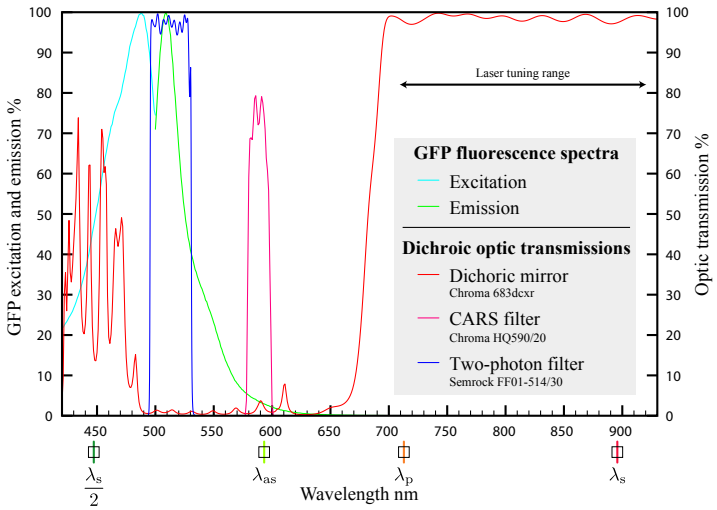

Figure 5.4: Fluorescence excitation and emission spectra of fibroblast cells infected with MCMV-GFP. The spectral transmissions of the dichroic mirror, CARS filter and two-photon filter are also shown, along with the wavelengths of the pump laser λ_p, the Stokes laser λ_s, the CARS signal λ_{as} and two-photon excitation $\frac{\lambda_s}{2}$. Filter and mirror data were supplied by the manufacturers [97, 146].

in the previous chapter (Section 4.3.1). MCMV-GFP samples were kept in dark conditions to avoid bleaching the fluorescence.

5.3.2 Fluorimetry for two-photon microscopy

In order to record CARS and two-photon images of the same sample, two conditions must be met. Firstly, the fluorophore must be excited at a suitable wavelength for two-photon, which is twice the equivalent one-photon wavelength [8]. Secondly, the emission spectrum of the fluorophore, with peak wavelength λ_{2p}, must be separated from the CARS laser wavelengths by suitable dichroic mirrors or filters.

To determine the required optics, and to confirm the cell infection and production of GFP, the excitation and emission spectra of an MCMV-GFP cell sample were recorded with a fluorimeter (FluoroMax, Spex). The spectra are shown in Figure 5.4. The excitation maximum is $486\,\mathrm{nm}$; the emission maximum is $511\,\mathrm{nm}$. These values are consistent with the known values for enhanced GFP [147]. This information was used to select suitable dichroic mirrors and filters whose spectral transmittances are also shown in Figure 5.4.

5.3.3 Imaging

The system was set up for imaging as shown in Figure 3.1 in Chapter 3. The pump and Stokes lasers were tuned to match the C–H stretch vibration at $2845\,\mathrm{cm}^{-1}$. The Stokes laser also provided two-photon fluorescence excitation, as shown in the energy diagram in Figure 2.1(D). The wavelengths are shown in Table 5.1 and in the graph in Figure 5.4.

	CARS		TWO-PHOTON	
Raman shift	R	$2845\,\mathrm{cm}^{-1}$		
Fluorophore			EGFP	
Pump laser wavelength	λ_p	$714.0\,\mathrm{nm}$		Blocked
Stokes/two-photon laser wavelength	λ_s	$896.0\,\mathrm{nm}$	$\lambda_s/2$	$448.0\,\mathrm{nm}$
Signal wavelength	λ_{as}	$593.5\,\mathrm{nm}$	$\lambda_{2\mathrm{p}}$	~ 500–$620\,\mathrm{nm}$
Dichroic mirror	1x 683dcxr		1x 683dcxr	
Filters	2x HQ590/20		1x FF01-514/30	

Table 5.1: The wavelengths of the lasers and signals used for the CARS and two-photon imaging modalities. The corresponding dichroic mirrors and filters are also shown. The CARS signal has a narrow spectral width ($\sim 0.5\,\mathrm{nm}$) and can be regarded as a single wavelength. The two-photon signal covers a broad range of wavelengths. The table data are shown graphically in Figure 5.4.

CARS images were recorded with the photomultiplier tube set up in the forward detection, i.e. for F-CARS. A dichroic mirror (683dcxr, Chroma) and two identical band pass filters (HQ590/20, Chroma) were used to separate the CARS signal from the excitation beams. Both filters were attached to the photomultiplier tube with a light-tight foam seal in order to minimize the effect of stray light in CARS images. The combined transmission of this filter pair at the CARS signal wavelength λ_{as} is only $50\,\%$. This does not pose a significant problem when working with fixed cells as laser power can be increased to compensate for the lost signal. For imaging live cells (Chapter 6) the pair were replaced with higher-transmission filters. The two-photon signal was filtered by a band pass filter (FF01-514/30, Semrock). This filter transmits the peak region of the GFP emission spectrum (Figure 5.4).

When imaging fluorescent samples, either the pump or Stokes wavelength can be used for two-photon excitation. In this case the Stokes laser was used as its equivalent one-photon wavelength $\lambda_s/2$ is closest to the excitation peak of GFP. To record a two-photon image the pump beam was blocked and the detector was set up in the backward (E) position. Although exciting at a wavelength with less than $50\,\%$ of the maximum absorption it was found that sufficient two-photon signal was generated for high quality images.

All images presented in this chapter were recorded with a $60\mathrm{x}$ water immersion objective lens (Table 3.1).

5.4 Results

5.4.1 CARS imaging of infected cells identifies virus-induced changes

Figure 5.5 shows a CARS image of a typical infected cell from the (non-fluorescent) MCMV sample. The cell has lost its characteristic triangular shape and the nucleus has expanded to $27\,\mu\mathrm{m}$ diameter compared to $16\,\mu\mathrm{m}$ in the healthy cell shown in the previous chapter, Figure 4.7(A).

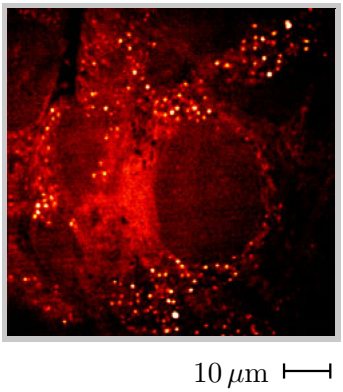

Figure 5.5: CARS image of a fibroblast cell infected with MCMV.

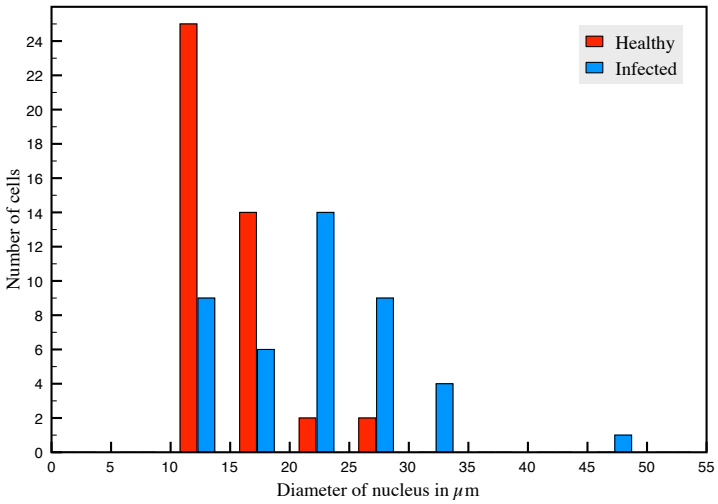

Figure 5.6: Histogram of nuclear diameters comparing 43 healthy cells and 43 infected cells (MCMV).

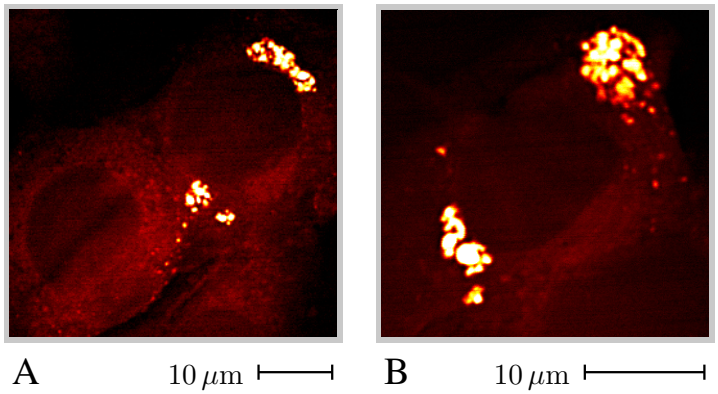

Figure 5.7: CARS images of two different fibroblast cells infected with MCMV. Both exhibit dense accumulations of lipid droplets.

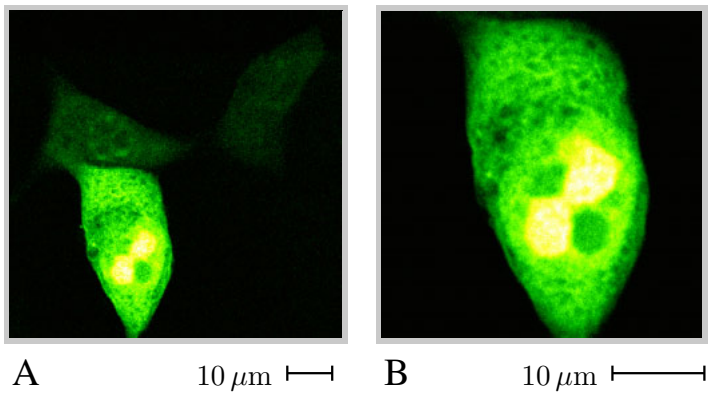

Figure 5.8: Two-photon image of three fibroblast cells infected with MCMV-GFP (A). The pump laser was blocked; two-photon excitation was provided by the Stokes laser at 922 nm. The laser power incident on the sample was 15 mW. The image is the average of 4 scans at 11 s/scan. A second image showing only the lower cell was recorded by scanning a smaller region (B).

To confirm that expansion of the nucleus is caused by the infection, the sizes of nuclei were measured in 43 healthy and 43 infected cells. As the cell nuclei are generally elliptical in shape measurements were made of the major axis (full) length A and minor axis B, and the resulting size expressed as a diameter $\sqrt{AB}$. Figure 5.6 shows a histogram of the measured nuclear diameters. The median diameter of healthy cell nuclei was 13.9 μm, and 20.7 μm for infected cells.

In addition to nuclear expansion, a number of infected cells showed very dense accumulations of lipid droplets at the nuclear periphery, producing a strong CARS signal from these regions. Two examples are shown in Figure 5.7.

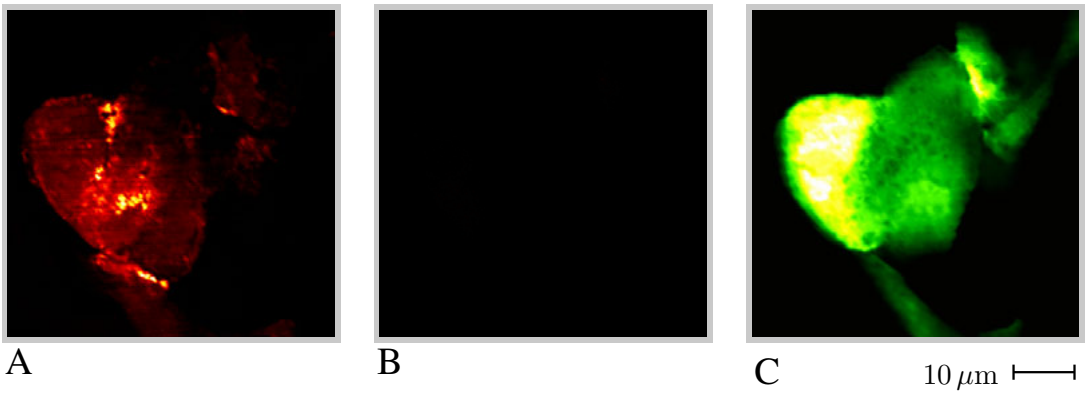

Figure 5.9: A CARS image of an infected cell was recorded (A). The pump and Stokes laser beams were shifted out of phase and the same image was recorded again (B). A two-photon image of the same cell (C).

5.4.2 Two-photon imaging of infected cells indicates viral protein expression

The MCMV-GFP infection causes cells to express GFP along with other virally-encoded proteins. Two-photon imaging revealed its intracellular location. Figure 5.8(A) shows an image of three infected cells. The three cells have different intensities, indicating different levels of viral protein expression. (The top-right cell is barely visible.) Figure 5.8(B) was recorded by scanning just the lower cell. The features it shows—a bright nucleus and a patchy cytoplasm—were found in many cells in the late stages of infection.

5.4.3 Multimodal imaging correlates infection with morphological changes

In order to establish the validity of multimodal images it is essential to check that the signals from each modality are adequately separated into their respective detection channels. Figure 5.4 shows that the CARS filters (HQ590/20, Chroma) will transmit a small fraction of the fluorescence signal. There is spectral overlap between the CARS and two-photon detection channels. To evaluate the effect of this leakage, three images of the same MCMV-GFP infected cell were recorded, shown in Figure 5.9. Images (A) and (B) were recorded in the CARS detection channel. Before recording image (B) the pump and Stokes lasers were shifted out of phase, ensuring that no pulses arrive in the sample simultaneously and no CARS signal is generated. Any significant residual light in the CARS channel is therefore due to two-photon fluorescence. Image (B) appears dark, revealing that the leak of fluorescence light into the CARS channel does not significantly perturb CARS images. Quantitatively, the mean pixel intensity of image (B) is $15\,\%$ of that of image (A), showing that the signal leakage is small compared to the average CARS signal intensity. Image (C) shows the two-photon image; this image is recorded with the pump beam blocked and so is not affected by cross-channel leakage. To summarize, it was found that some fluorescence emission leaks into the CARS detection channel, but does not significantly affect CARS images.

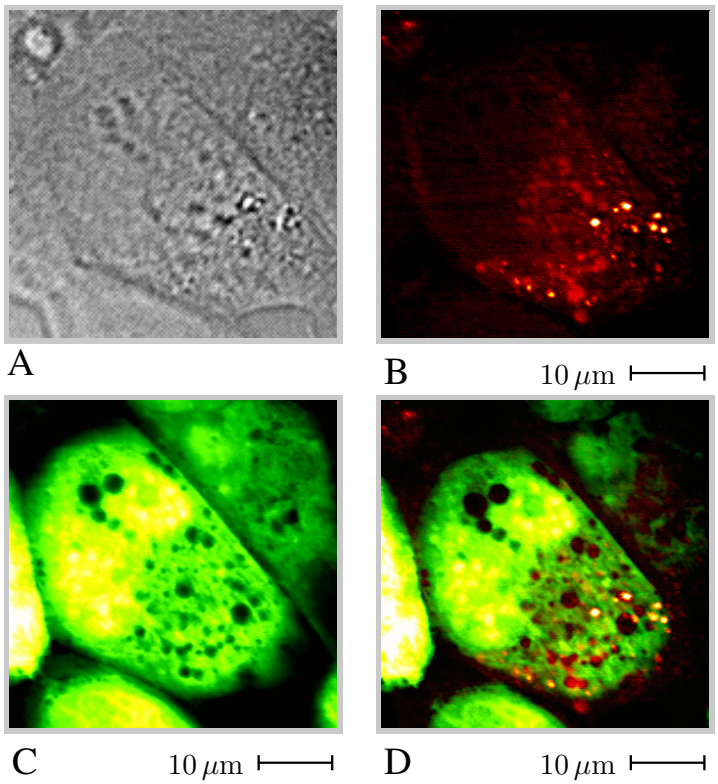

Figure 5.10: Images of infected cells recorded with bright field (A), CARS (B) and two-photon (C). An overlay of the CARS and two-photon images (D). The laser powers incident on the sample were 26 mW (B) and 16 mW (C).

CARS and two-photon images of MCMV-GFP cells were recorded sequentially, along with bright-field images of the same region. An example is shown in Figure 5.10(A–C). This cell has lost its normal morphology and the nuclear boundary is no longer clearly-defined. By overlaying the two-photon image on the CARS, Figure 5.10(D), it is possible to compare the intracellular sites of lipids and GFP.

A number of images, such as Figure 5.11(A–F) showed bright fluorescent spots, often adjacent to the nucleus, which may be the first signs of cellular GFP expression in the cytosol, indicating an early stage of infection. Cells in later stages of infection, such as Figure 5.11(G–I) showed GFP throughout the cell, with the nucleus appearing brighter than the cytosol. The appearance of 'black holes' in the cytoplasm was also a common feature.

5.5 Discussion

The effects of cytomegalovirus on the cells are summarized in Figure 5.12. Comparing CARS images of healthy and infected cells allowed observation of the morphological changes the cell undergoes during infection by MCMV: expansion of the nucleus and rounding of the overall cell shape. As the nuclear boundary could be clearly identified in most images, its diameter could be measured. The nuclei of the MCMV infected cell sample were on average $50\,\%$ larger than the healthy sample. This is probably an underestimate of the overall expansion as the cells were in different stages of infection at the time they were fixed when some nuclei may not yet have expanded to the maximum size. The nuclear expansion is likely due to the stimulation of the host cell metabolism induced by the virus (Section 5.2.5) and the production of new viral capsids within the nucleus (Section 5.2.4). Whilst measurement of nuclear expansion can statistically confirm infection in a large sample of cells, it is not sufficient to identify infection in a single cell. For this reason, further experiments used the MCMV-GFP strain.

The intracellular distribution of GFP was imaged by two-photon microscopy. Combining this with CARS produced images that correlate GFP expression with the cell shape and the lipid droplet distribution. To perform this type of multimodal imaging it is necessary to spectrally separate the two signals. As with any multicolour imaging setup, the leaking of light from one detection channel into the other must be assessed. A 'CARS image' recorded with the pump and Stokes laser beams synchronized, but out of phase appeared dark, Figure 5.9(B). This check confirmed that cross-channel leakage did not cause manifestations in images. Although the setup described here is specific for imaging enhanced GFP it could readily be modified to work with different fluorescent proteins, provided that the emission wavelengths do not spectrally overlap the CARS signal. This can usually be arranged, as the CARS signal wavelength can easily be adjusted by shifting (together) the pump and Stokes wavelengths. Whilst the picosecond pulse durations used for on this setup are not ideal for two-photon imaging, the process has been demonstrated with such long pulses [148]. In practice it was found that the GFP provided ample signal when excited with around $15\,\mathrm{mW}$, despite the less-than-optimum

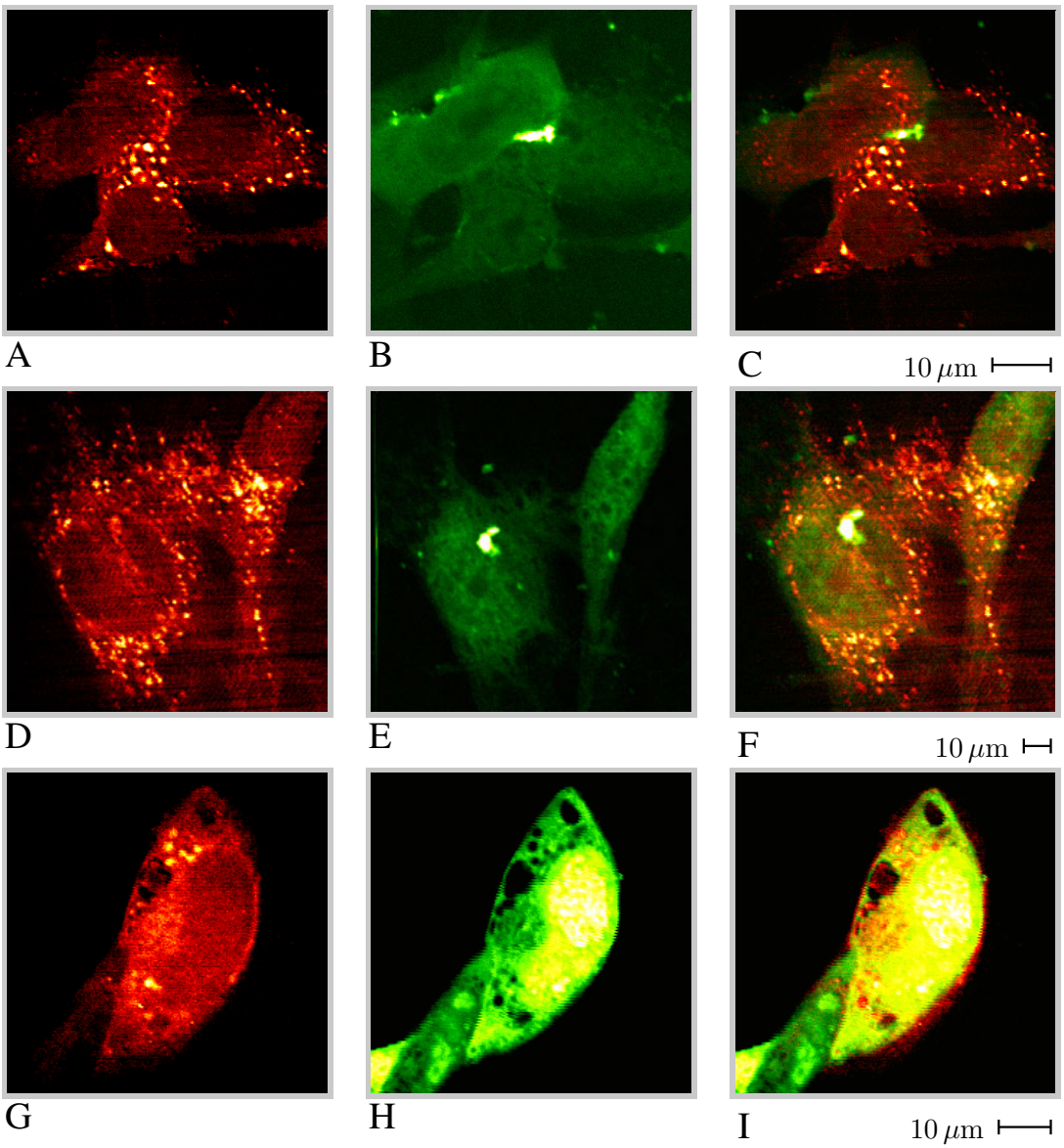

Figure 5.11: CARS image of cells infected with MCMV-GFP (A). Two-photon image of the same area of sample (B). The two-photon image is overlaid on the CARS image (C). Images (D) to (I) show different cells imaged with the same method.

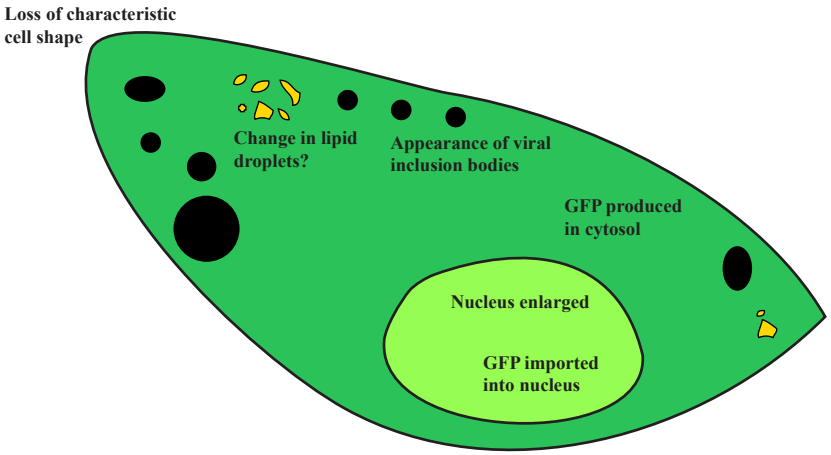

Figure 5.12: Illustration of the effects of infection on fibroblast cells by a genetically-modified cytomegalovirus (MCMV-GFP).

excitation wavelength (Figure 5.4) providing images with a good level of signal-to-noise.

The expression of GFP by the cell is a definitive indicator of cell infection, as it can only be caused by the integration of the GFP gene by the virus into the host. It indicates that viral proteins have been successfully expressed in significant quantities, demonstrating that the virus has succeeded in disrupting the cell cycle and transcribing the viral genome. GFP is expressed by the cell in ribosomes in the cytoplasm, along with other viral proteins required for assembly of new virions. The first signs of GFP were as bright dots, often adjacent to the cell nucleus, as shown in Figure 5.11(B) and (E). These dots may highlight the specific cellular sites of viral protein synthesis or folding. It is reasonable to assume that the amount of cellular GFP increases with time post infection. Therefore images of cells containing substantial amounts of the protein, such as Figure 5.11(H), show cells in later stages of infection. The three adjacent cells shown in Figure 5.8(A) are apparently in different stages of infection. This may indicate that the start of infection was not synchronized as intended (Section 4.3.1), that the infection proceeded at different rates in the different cells, or that the cells were in different phases of the cell cycle upon infection resulting in different viral latency times [139]. It is notable in most images of cells in late-stage infection that the concentration of GFP in the nucleus is significantly higher than in the cytosol (where it is produced). This difference cannot be explained by passive diffusion alone. It is known that the virus significantly disrupts cellular transport mechanisms, including those which shuttle proteins back and forth across the nuclear membrane [149]. Whilst proteins required for nucleocapsid assembly must be imported into the nucleus, GFP is not fused to any other proteins, nor does it carry a nuclear import marker. The mechanism which transports GFP from the cytoplasm into the nucleus remains unclear.

Most two-photon images of cells in the late stage of infection contain many circular ‘black holes’. Some of these holes are lipid droplets, as shown by overlaying the two-photon image on the CARS, Figures 5.10(D) and 5.11(I). The GFP cannot enter the hydrophobic environment

of lipid droplets. Other holes are viral inclusions: accumulations of incomplete viral particles, viral proteins and other foreign material sequestered in a membrane-bound body by the cell as a defense mechanism. These bodies are a typical cytopathic effect observed in many viruses (see Section 5.2.2). Any GFP present in these bodies would not yet be folded, and hence not fluorescent. These inclusions are also visible in bright field images, Figure 5.10(A), and are often the only discernible sign of infection when using conventional light microscopy.

Whilst the morphological changes in the cell as a result of infection are unmistakable, it is not clear from these results whether the virus induces an alteration in the cellular lipid droplet distribution. A number of cells, such as those in Figures 5.7, showed dense accumulations of lipid droplets, although these were only seen in the MCMV samples and not in MCMV-GFP. It is difficult to attribute these formations to a specific stage or function of infection and the possibility that these are artifacts of the fixing process, or an effect non-viral in origin, cannot be ruled out. However tests of formaldehyde fixation of lipid droplets [73] suggest it is a safe technique and does not disturb lipid droplet structure. The connection between the viral infection and these accumulations requires further investigation.

The method presented in this Chapter can be applied to investigate a number of virus-host interactions, however there are several limitations to working with fixed cells. The specimens represent snapshots of cells at the time they were fixed, leaving the intermediate details to inference. The lack of dynamic information made image interpretation difficult as the timing of observed effects could not be placed in sequence. For these reasons, and due to the limited storage time of fixed cells (Section 4.4.3), this work was extended to live cell imaging. The ability to image living cells on the microscope is demonstrated in the next chapter.

5.6 Conclusions

Combined CARS and two-photon imaging were used to study the interactions between cytomegalovirus and host fibroblast cells. The established morphological changes associated with infection were observed in cells infected by MCMV. It was found that nuclei in infected cell samples were on average $50\,\%$ larger than in healthy cells. A number of cells exhibited dense accumulations of lipid droplets at the nuclear periphery, though this was not definitively attributed to the viral infection. As a means to confirm cell infection, a genetically modified virus, MCMV-GFP, was also used (separately) to infect cells. The location and extent of viral protein expression was revealed in two-photon images, whilst sequential CARS imaging of the same cells correlated the infection with changes in cell morphology and lipid droplet distribution. The combination of the two techniques showed that numerous ‘black holes’ appear in cells at the late stage of infection. These holes, which are dark in both CARS and two-photon images, were identified as inclusions. Additionally, it was found that GFP was imported into the nucleus in the late stage of infection.

These experiments focussed on studying the effects on fibroblast cells from infection with

cytomegalovirus. The method is generally applicable and could readily be adapted to work with other viruses or cell types. The principal requirement is that virus can be modified to induce fluorescent protein expression by the host cell, and that the CARS signal from lipids and the two-photon signal from the protein can be adequately separated by wavelength.

6

Live cell imaging

6.1 Introduction

The previous chapter reported the specific virus-host interactions in fixed fibroblast cells infected by cytomegalovirus and imaged by multimodal microscopy. In this chapter the ability to image living cells is demonstrated. The samples used and the imaging methods are broadly similar to Chapter 5; the description given here will focus on the specific adaptations that were made to the microscope to support living samples and the measures taken to minimize laser power in order to prevent photodamage. The results illustrate the importance of live cell imaging as a tool for virological research and demonstrate the ability to record time lapse images of a single cell over an extended period.

Two aspects of working with fixed specimens were found to limit their utility. Firstly, the formaldehyde used as a fixative does not fix lipid droplets, limiting the specimen life to a few days at best (Section 4.4.3). Secondly, it was difficult to reconstruct a sequence of events from a series of still snapshots of different cells (Section 5.5). The same difficulty arises in electron microscopy-based studies of the virus life cycle, where the movement of viruses through the cell during the infection cycle must be inferred from sets of still images (see Figure 5.3 for an example). The gaps—where crucial events are missing from the record—lead to significant uncertainty in how the virus replicates. Unfortunately electron microscopy cannot be applied to living cells due to the high electron powers involved. Fluorescence microscopy can be used for imaging live cells, however the range of compatible fluorophores is very limited. The use of fluorescent proteins, including GFP and variants, is often applied [150]. Some synthetic

fluorophores can be used in living cells, however they are often associated with phototoxicity [151].

In live cell imaging CARS microscopy has a conspicuous advantage; it can be used for label-free imaging of the dynamic intracellular environment in living cells. It does not restrict the range of usable cells based on the limited ability to label live cells with fluorescent markers. The study described in Chapter 5 can readily be extended as both CARS and GFP expression are amenable to live cell imaging. The ultimate goal of applying live cell techniques to this study is to realize the ability to observe the virus life cycle played out in a single cell through time lapse imaging. The results presented in this chapter will show that this is feasible.

As the microscope system is custom-built it can readily be adapted to suit the needs of a specific research objective. This chapter will outline the required physiological conditions, describe the adaptation to the microscope and present the results of tests of live cell imaging.

6.2 Background

Cells grown in culture must be maintained at precise physiological conditions to avoid cell stress and promote growth (see Section 4.2.1). For fibroblasts, this requires keeping the temperature at $37\,^{\circ}\mathrm{C}$ and maintaining the pH of the medium in the range 7.0–7.4 [152]. A $5\,\%$ carbon dioxide atmosphere is used to stabilize the pH by equilibriating the reaction of the air with the medium [102]. The technical challenge for imaging living cells therefore is to reproduce these conditions on the microscope stage.

A variety of commercial and non-commercial systems have been developed for live cell imaging. An up-to-date online review is provided by *Nikon Corporation* [153]. The simplest systems consist of sealed microscope slides which can protect cells whilst on the microscope and allow imaging for periods of minutes to hours [154]. For long term imaging however a heated chamber is required. Sophisticated commercial systems allow the long-term imaging of cells with heaters to maintain temperature and perfusion ports for changing media and maintaining carbon dioxide tension. Other options include customized glass flasks, such as the modified Carrel Flask developed by Stevenson et al. [155], which incorporate heating whilst providing easy access for changes of media or passaging.

Whilst these systems would easily meet the requirements for imaging the infected cells used in this study, they are more elaborate than is required. Maintenance of infected cells does not need to be for more than a few days, as after this time most cells will have succumbed to the virus. Additionally, as the virus halts cell mitosis there is no need for passaging of cells whilst on the microscope. A completely sealed cell chamber is sufficient. The cells can be grown and infected in cell culture, then transferred to the chamber and sealed before being placed on the microscope. The design and construction of the chamber will be described in the following section.

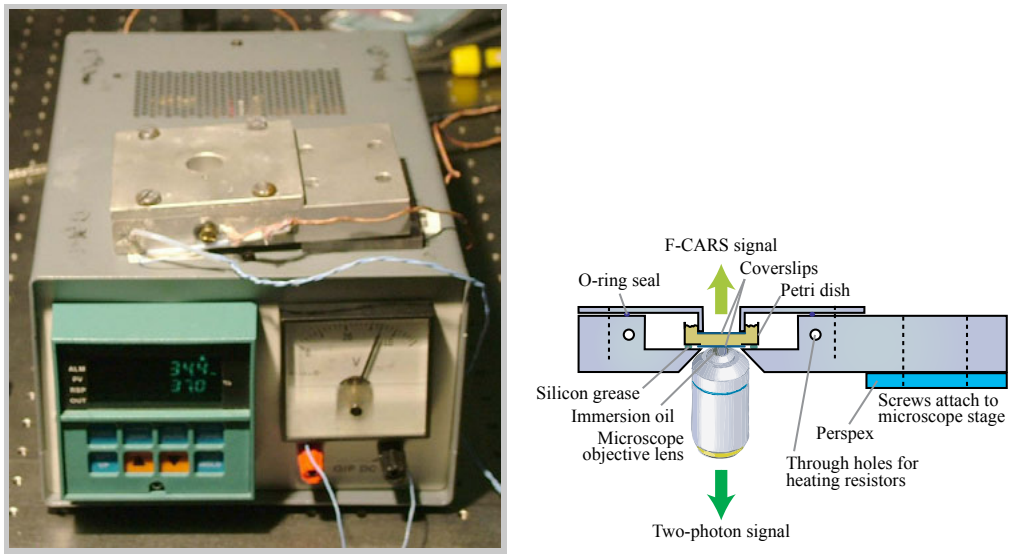

A B

Figure 6.1: Photograph of the cell chamber and temperature controller used for live cell imaging (A). Diagram of the cell chamber on the microscope (B).

6.3 Methods

Most of the methods used for these experiments have been described in previous chapters. This section will cover only the adaptation of the microscope for imaging living specimens. The operation of the CARS microscope was described in detail in Chapter 3. The cell culture methods used for sample preparation were described in general in Section 4.2.1 and the methods for preparing infected samples and multimodal imaging in Section 5.3.

6.3.1 Cell chamber

A cell chamber was built to contain living cells on the microscope. A photograph and diagram are shown in Figure 6.1. The chamber is designed to simply replace the existing microscope stage plate, visible in the photograph in Figure 3.2, allowing the two to be readily exchanged depending on the experiment. The design requirements for the chamber were:

- It must be sealed.
- It must include transparent optical windows to allow collection of the forward and backward signals.
- It must withstand autoclaving.
- It must fit into the narrow space ($24\,\mathrm{mm}$) between the top of the objective lens and the bottom of the condenser lens.

The chamber was constructed from aluminium, which has a high heat capacity to provide thermal stability and can withstand high temperatures during autoclaving. The chamber is designed to accommodate a coverslip-bottomed petri dish (P35Gcol-1.0-14-C, MatTek) which is sealed into the chamber with silicon grease as shown in the diagram in Figure 6.1(B). An additional circular glass coverslip was glued into the lid of the chamber to transmit the F-CARS signal. The lid was shaped such that, when closed, the coverslip is immersed in the culture medium. This ensures that condensation does not form on the coverslip and minimizes the number of changes in refractive index between the sample and the forward detector which may refract light away from the detector.

High-power ceramic resistors were potted into holes drilled through the length of the assembly. A thermocouple attached to the front surface of the chamber was connected to a temperature controller (UDC3000, Honeywell) and power supply which powered the resistors. During operation the temperature was stable to within $\pm 0.1\,°\mathrm{C}$.

In Chapter 5 a 60x water-immersion objective lens was used. This is problematic for long-term live cell imaging as the immersion fluid can dry up. Instead a 100x oil immersion objective was used (see Table 3.1 for objective specifications), however this may cause optical aberrations due to the refractive index mismatch between the immersion fluid and the medium [40].

6.3.2 Sample preparation

The specific sample preparation for fixed cells was described in Section 4.3.1[1]. The live samples were prepared by the same method, with the final step seeding them into the petri dish. The cell chamber was autoclaved, then loaded and sealed in a $5\,\%$ CO_2 atmosphere before being transferred to the microscope for imaging. The air-tight seal of the chamber is sufficient to maintain a stable pH. This was monitored with an indicator dye, Phenolred, which changes colour when the pH deviates from 7.4 by more than 0.4 [151].

6.3.3 Imaging

The method used here for multimodal CARS and two-photon imaging is the same as that described in Section 5.3.3, and illustrated in Figure 3.1, with a few modifications[2]. These modifications were made with one aim in mind—to minimize the exposure of the sample to laser radiation.

An additional photomultiplier tube was added to the system which allows simultaneous recording of the two signals: CARS in the forward direction (F) and two-photon in the backward (E). The two signals are acquired in synchronization by the acquisition board (see Section 3.4.7) and displayed by the microscopy software. This could eliminate the need to scan the sample twice (once for each modality), thus reducing laser exposure significantly.

[1] As in Chapter 5, samples were prepared and the infection performed by Michael Ochsenkühn.
[2] The adaptations described in this subsection (6.3.3) were made by Christine Wong.

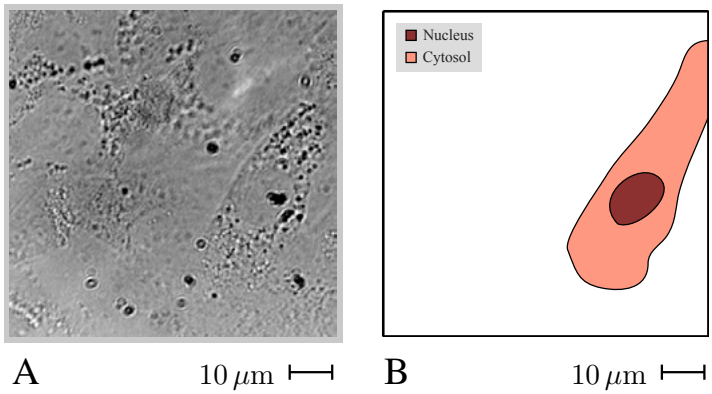

Figure 6.2: Bright field image of fibroblast cells after five days on the microscope (A). The image was recorded with a 100x microscope objective lens (Table 3.1). Outline of one of the cells (B). Other cells can be seen in the microscope image but have indistinct outlines due to the limited contrast of bright field microscopy.

The filters used in Chapter 5 for imaging fixed cells did not provide good transmission at the CARS signal wavelength (see Figure 5.4). They were replaced with two $600\,\mathrm{nm}$ band pass filters (FF01-600/14-25, Semrock) with $99\,\%$ specified transmission at the CARS signal wavelength [146]. In addition to improving the signal detection efficiency, the narrower bandwidth ($14\,\mathrm{nm}$) of these filters better excludes stray light from entering the photomultiplier tube. The filter for two-photon imaging was replaced by one with a wider bandwidth (FF01-510/84, Semrock). This transmits a broader range of the spectrum of GFP emission, whilst still blocking the CARS signal wavelength. Both of these optimizations allowed lower laser power to be used for imaging.

The most basic method for preventing photodamage is to ensure that the cell is only exposed to laser light during useful imaging. In live cell experiments greater use was made of bright field imaging for both cell selection and focusing. However the resolution of bright field imaging is poor due to the use of an infrared LED for illumination. Therefore the focus must still be fine-tuned whilst recording CARS images, inevitably leading to additional exposure of the cell to the laser beam.

6.4 Results

6.4.1 Live cells can be maintained on the microscope for 5 days

A sample of healthy (uninfected) cells was placed on the microscope. Figure 6.2(A) shows a bright field image of the cells recorded after $5\,\mathrm{d}$. As cells were not passaged during this time cell growth is likely to have stopped due to contact inhibition. The cells are identified as healthy as they are still adherent to the coverslip. (See Section 4.2.1 and Figure 4.1 for an explanation of cell culture.) This timescale is more than sufficient to observe the full virus life cycle, as cytomegalovirus typically starts producing progeny at 48–$72\,\mathrm{hpi}$ [114].

6.4.2 Photodamaged cells exhibit morphology changes and detachment

The effect of photodamage on cells was investigated by subjecting a single cell to laser scanning. Figure 6.3(A) shows a cell imaged with bright field imaging. The cell was then scanned by the laser with a power of $3\,\mathrm{mW}$ for $3\,\mathrm{min}$ and imaged again in bright field (B). Comparing the corresponding cell outlines (E) and (F), the cell's 'arm' appears to have retracted. After scanning with $6\,\mathrm{mW}$ for a further $3\,\mathrm{min}$ (C) the cell showed morphological changes; the cell membrane bulges outwards. Scanning at $9\,\mathrm{mW}$ for a further $3\,\mathrm{min}$ (D) results in loss of adherence to the glass surface suggesting that necrosis or apoptosis has occurred.

An approximate estimate of the cell's damage threshold can made by quantifying the exposure to the laser beam as the product of the laser power and the total scan time. Assuming that cell damage is cumulative over the duration of this experiment, i.e. that the cell did not recover between the scans, the exposure threshold for this cell lies below the total exposure of the cell in Figure 6.3(B), i.e. less than $9\,\mathrm{mW\,min}$. For a CARS image recorded by averaging over 4 scans with typical scanning parameters (Table 3.2) the total acquisition time is $40\,\mathrm{s}$. This suggests that the maximum power threshold for CARS imaging is around $12\,\mathrm{mW}$. This quantity was used as an estimate of the power live cells could tolerate.

6.4.3 Cell migration and lipid droplet diffusion limit the ability to record stacks

Video 6.1 shows a stack of slices through a live cell at increasing depths[3]. The acquisition time per slice is $33\,\mathrm{s}$ with an additional $30\,\mathrm{s}$ required between each slice to adjust the microscope stage micrometer. The movement of lipid droplets due to diffusion can be observed between each slice and it appears that the cell has migrated slightly during the stack recording.

Faster recording may reduce the effects of movement, however in general a stack cannot provide a faithful three-dimensional snapshot of the dynamic intracellular environment. Even with fully automated optical sectioning, the recording of a stack cannot be made sufficiently fast to freeze intracellular movements, as active transport processes in cells can cause translations of lipid droplets at speeds greater than $0.5\,\mu\mathrm{m/s}$ [24].

6.4.4 Use of low laser power increases noise in images

The cell damage caused clearly requires the reduction of laser power to the lowest possible levels. To quantify the effect on image quality, two images of the same cell were recorded at different laser powers. Figure 6.4(A) shows a cell recorded with $53\,\mathrm{mW}$ laser power incident on the sample and a voltage of $330\,\mathrm{V}$ applied to the photomultiplier. Figure 6.4(B) shows the same cell with $20\,\mathrm{mW}$ laser power and a voltage of $602\,\mathrm{V}$.

When reducing the total laser power incident on the sample the CARS signal drops off cubically (see Equation 3.3 in Chapter 3). Therefore a reduction in laser power from $53\,\mathrm{mW}$ to

[3] This stack was recorded by Christine Wong.

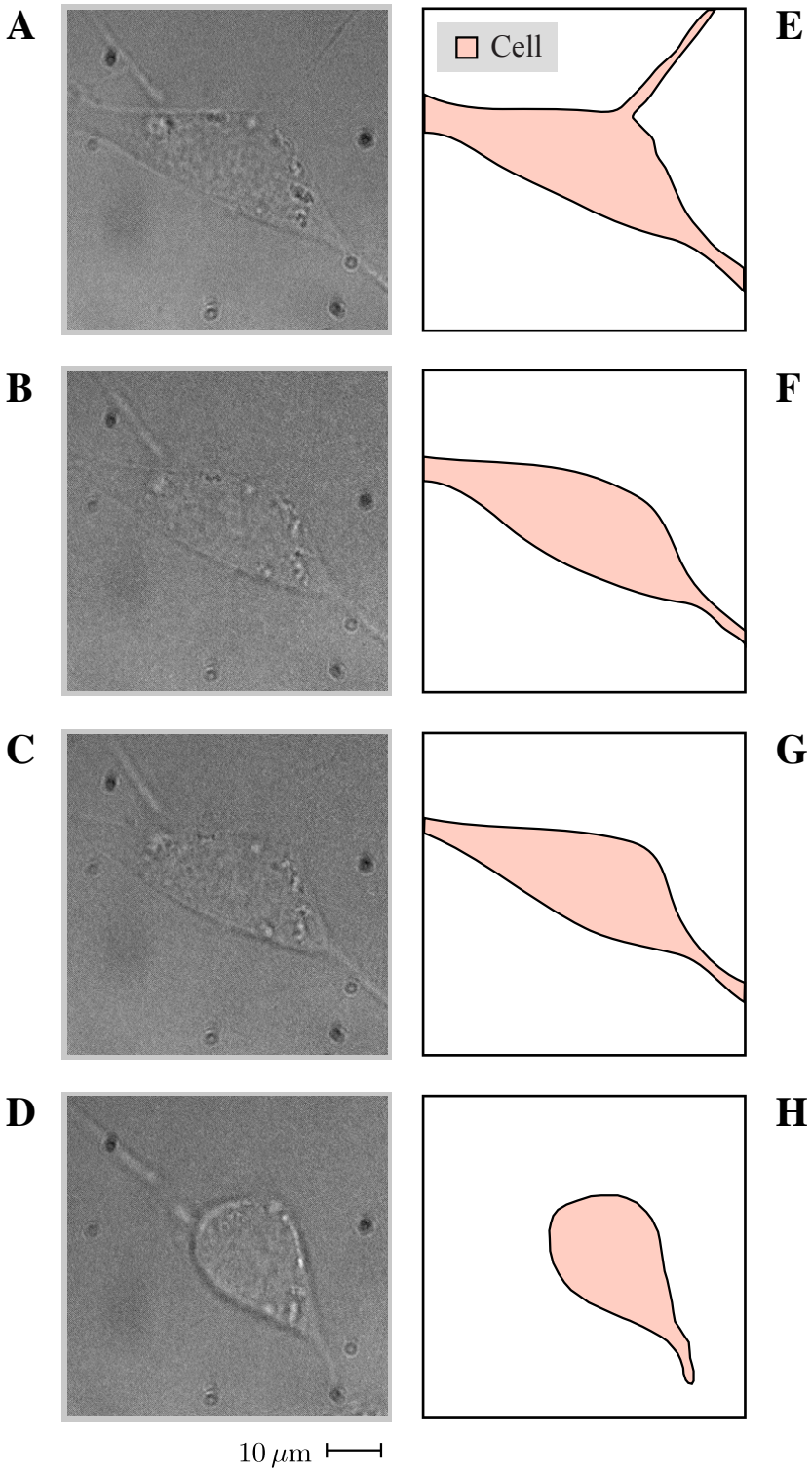

Figure 6.3: Effect of photodamage on cells recorded with bright field imaging. The cell (A) was scanned for 3 minute intervals at successively increasing laser powers: 3 mW (B) then 6 mW (C) then 9 mW (D). The shape of the cell in images (A–D) is outlined in (E–H). Due to the limited contrast the shape of the nucleus cannot be clearly defined .

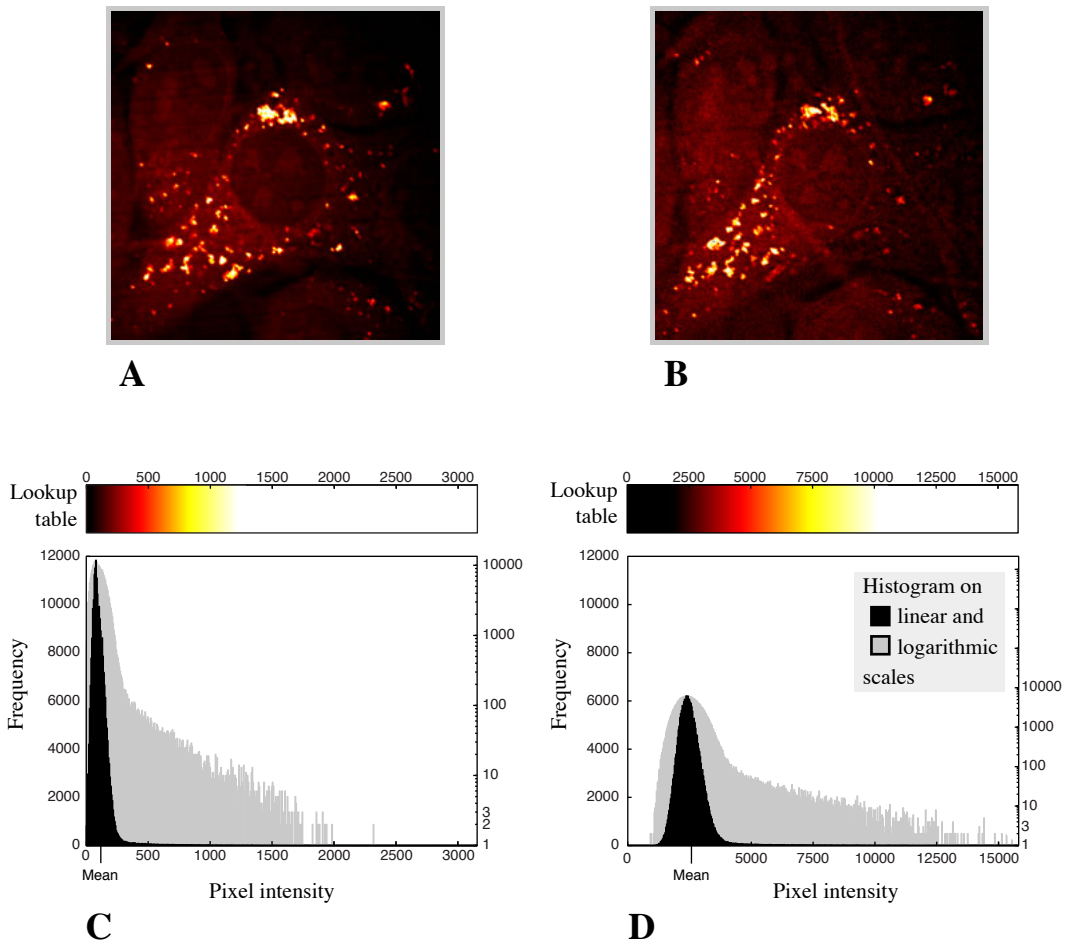

Figure 6.4: CARS images of a healthy live fibroblast cell. Image (A) was recorded with $53\,\mathrm{mW}$ laser power incident on the sample and a voltage of $330\,\mathrm{V}$ was applied across the photomultiplier tube. Image (B) used $20\,\mathrm{mW}$ laser power and $602\,\mathrm{V}$ and was recorded directly after image (A). (C) and (D) show the histograms of the two images.

$20\,\mathrm{mW}$ reduces the CARS signal level by $95\,\%$. As the voltage on the photomultiplier tube was increased between the high-power image (A) and the low power (B)—in order to compensate for the lower signal—the absolute pixel values cannot be directly compared between the two images. The overall image brightness appears similar as the lookup tables were also adjusted to take account of the different signal levels.

To quantify the effect of the reduced signal level the histograms are plotted below the corresponding images, in Figure 6.4(C) and (D). Comparing (D) with (C), the mean pixel value has shifted to a higher intensity. This is largely due to the higher dark level on the photomultiplier tube which increases as higher voltages are applied. This dark level is the combined effect of several causes. The principal cause is dark current, which is mainly due to the thermionic emission of electrons from the photocathode [45]. This dark current is strongly temperature-dependent and can be reduced by cooling of the tube. It increases with voltage and ultimately places a limit on detection sensitivity as at high voltages it will eventually swamp the signal [156]. Other contributions to the dark level come from stray light entering the tube.

The contrast in an image defined by a set of pixel values I, is given by the dimensionless quantity [157]

$$C = \frac{I_{max} - I_{min}}{\bar{I}}$$

where I_{max} is the maximum pixel intensity, I_{min} the minimum, and $\bar{I}$ the mean. The contrast in the high-power image (A) is 27, compared to 6.1 in the low-power image (B). This is probably an overestimate of contrast in the low-power image as it includes the spurious contrast caused by the dark level.

Further reduction of the laser power causes a further loss of contrast and a dark level which begins to swamp the signal. The contrast is then reduced below the level required to distinguish image features (lipid droplets in this case). The detection sensitivity could be improved by reducing the amount of stray light entering the photomultiplier tube and by improving the filtering of the signal from the excitation beams. Cooling the tube to reduce thermionic emission would provide further improvement.

6.4.5 A single living cell can be imaged with CARS over 7 h

Video 6.2 shows bright field and CARS images of a single cell recorded over a $7\,\mathrm{h}$ period. Images were recorded once every $30\,\mathrm{min}$. The image acquisition time was $66\,\mathrm{s}$ with a power of $23\,\mathrm{mW}$. The total exposure is therefore $354\,\mathrm{mW\,min}$.

6.4.6 CARS images recorded at other Raman shifts have large background

All CARS images of fibroblasts presented so far were recorded at the strong C–H stretch vibration at $2845\,\mathrm{cm}^{-1}$. CARS images of healthy live cells were also recorded at two other Raman shifts. The Raman spectra in Figure 4.2 show a number of other peaks which may have potential for CARS imaging. Two of these peaks were selected. The peak at $1663\,\mathrm{cm}^{-1}$ consists

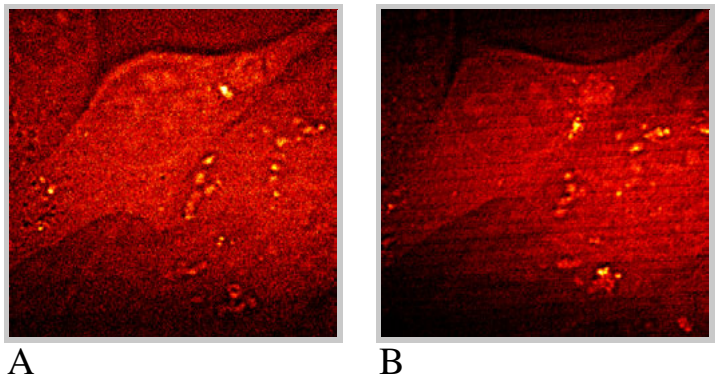

Figure 6.5: CARS images of a healthy fibroblast cell at and $1658\,\mathrm{cm}^{-1}$ (A) and $1450\,\mathrm{cm}^{-1}$ (B). Image (B) was recorded after image (A).

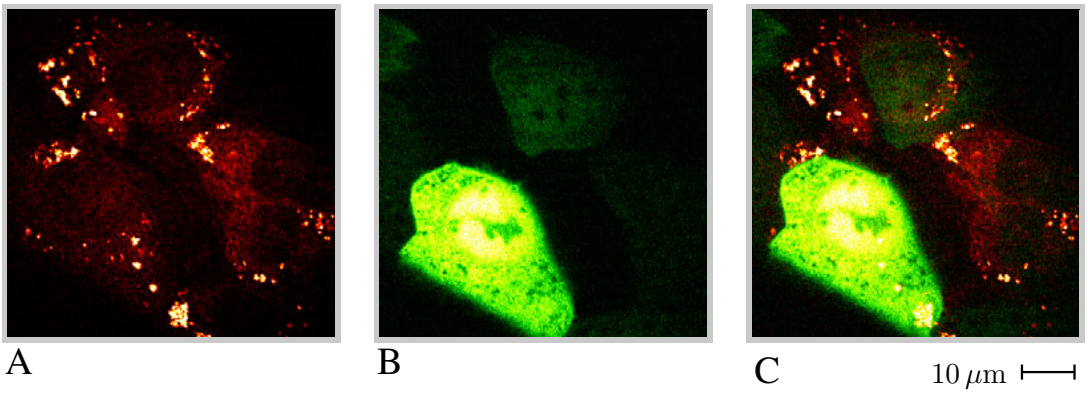

Figure 6.6: CARS image of infected fibroblast cells (A) and sequential two-photon image of the same cells (B). The two-photon image is overlaid on the CARS (C). The laser powers were 33 mW (A) and 15 mW (B).

of the overlapped C=C stretch and amide I band; the peak at $1450\,\mathrm{cm}^{-1}$ is a CH_2 vibration also present in lipids [109]. As the CARS and Raman peaks may have different positions in their corresponding spectra (Section 3.5.5), images were first recorded over a range of around $25\,\mathrm{cm}^{-1}$ to determine the Raman shift which provided best contrast. Figure 6.5(A) shows a CARS image recorded at $1658\,\mathrm{cm}^{-1}$ with a laser power of $65\,\mathrm{mW}$. Figure 6.5(B) shows an image recorded at $1450\,\mathrm{cm}^{-1}$ with $84\,\mathrm{mW}$. As these Raman bands are much weaker than the C–H stretch at $2845\,\mathrm{cm}^{-1}$ the contrast in the images is much reduced and the nonresonant background dominates. The laser power is not tolerable to living cells and there are visible indicators of cell damage in Figure 6.5(B).

6.4.7 Combined CARS and two-photon imaging of living cells allows monitoring of infection stage

Images of live cells infected by MCMV-GFP (defined in Section 5.3) were recorded with CARS and two-photon sequentially[4]. Figure 6.6 shows an example. The CARS image, Figure 6.6(A) shows the lipid droplet distribution in several cells, whilst the two-photon image, Figure 6.6(B) indicates that they are in different stages of infection. The two-photon image is overlaid on the CARS in Figure 6.6(C). The clustering of lipid droplets is observed in some cells, similar to that seen in fixed (MCMV) infected cells in Figure 5.7.

6.5 Discussion

The demonstration of live cell CARS imaging showed that time lapse recording of a single cell over a period of $7\,\mathrm{h}$ is possible without observable photodamage. This is long enough to observe the effect of viral infection and if the imaging period were extended to around $48\,\mathrm{h}$, by reducing laser power or number of scans, this would allow observation of a single cell through the complete cytomegalovirus infection cycle. It was also demonstrated here that the method of multimodal microscopy combining CARS and two-photon described in Chapter 5 can be extended to image live cells (Figure 6.6). The images recorded show accumulations of lipid droplets similar, though less dense, to those seen in fixed cells in Figure 5.7. This suggests that the virus modulates the host cell lipid metabolism, however further investigation would be required to confirm this.

Laser power was the critical concern as cells were easily photodamaged. It appeared that cells' susceptibilities to photodamage depended on the proximity of other cells; isolated cells were more easily damaged than interconnected groups. Additionally cells appeared to 'recover' to some degree between scanning periods. The accumulated exposure of the cell imaged over $7\,\mathrm{h}$ (Video 6.2) was over five times that which killed the cell in Figure 6.3(D). If the cause of photodamage is the laser-induced accumulation of some noxious substance within the cell [18] it appears that this had time to dissipate during the $30\,\mathrm{min}$ interval between scans.

To date there have been few systematic studies of photodamage in CARS microscopy [75, 158]. It has been suggested that photodamage in both CARS [75] and two-photon [18] is caused by second-order processes at low laser powers and, additionally, higher-order processes at high laser powers. The damage threshold for the cell imaged in Figure 6.3 was estimated to be $12\,\mathrm{mW}$. This agrees with the general principle for nonlinear imaging that powers greater than $10\,\mathrm{mW}$ are damaging to cells [18]. However, the laser powers used in this chapter were generally significantly higher than this. Further optimization to the set-up is required to achieve imaging at powers below $10\,\mathrm{mW}$ whilst retaining sufficient image contrast to clearly identify cellular features such as lipid droplets. The various interdependent laser parameters, including

[4]These images were recorded by Christine Wong.

pulse duration, repetition rate, peak power, average power and pump-to-Stokes power ratio, can be adjusted to optimize the CARS signal and minimize photodamage. Performing this type of optimization needs a reliable indicator of cell damage. Whilst morphological changes are indicators of significant damage, an indicator based on observing whether cells later proceed to mitosis would be more suitable. The progression to mitosis could be observed by recording time lapse bright field images for a period of several hours after laser scanning [159]. This would allow a more precise determination of the laser damage threshold for healthy cells. By reducing laser power well below this threshold when imaging infected cells the important distinction between virus-induced and laser-induced damage can be made.

Whilst imaging live cells circumvents the problems associated with fixed cells (discussed in Section 5.5) it is not without drawbacks. The requirement to maintain physiological conditions on the microscope adds an extra level of complexity to the system. Sample preparation is also made more difficult, as cells must be prepared in a sterile environment, but imaged in a non-sterile optical lab. It is likely therefore that fixed cells will still have a role to play in this study. Whilst live cell imaging makes observation of virus-host interactions easier, fixed cell imaging is required to validate results. For example, fixed samples can act as a control for live cells to demonstrate that effects are caused by the infection, and not by poor maintenance of cell conditions on the microscope stage.

Future work on this system will require a systematic optimization in order to identify the causes of, and minimize, photodamage. If this can be achieved time lapse imaging of individual cells with both CARS and two-photon should be possible over periods of many hours. The images in this chapter were recorded sequentially, but the extension to simultaneous imaging poses no distinct obstacles and will allow multimodal imaging without increasing the laser exposure. The ability to watch virus-host interactions in a single cell throughout the infection cycle would provide a clearer picture of the process and help to answer the questions raised in the previous chapter. In particular it should help to identify processes causing the clustering of lipid droplets and the transport of GFP to the nucleus and identify the timing of these processes in the infection cycle. The ability to image at Raman shifts other than $2845\,\mathrm{cm}^{-1}$ was hampered in this work by the large nonresonant background. Future attempts will require subtraction or suppression of the nonresonant background. The congested fingerprint region of these cell's Raman spectra [108, 109] may contain other peaks which reveal significant chemical information about the infection process.

6.6 Conclusions

Fixed cell imaging provides limited information about the virus life cycle and there is a clear need for live cell imaging to complement it. This was demonstrated by the addition of a sealed temperature-controlled chamber to the microscope stage. Cells in the chamber can be kept alive for at least five days, sufficient for several infection cycles to occur. A single cell can

be imaged by time lapse recording of one image every thirty minutes for a period up to seven hours without causing visible signs of photodamage.

This work demonstrates that live cell imaging is a valuable technique for virological studies, especially when applied in tandem with fixed cell imaging on a flexible microscope platform. The ability to perform live cell imaging demonstrated here should allow, as future work, some of the questions raised about cytomegalovirus life cycle to be answered.

7
Conclusions

The contribution of this research has been the development of an enhanced method for studying viruses. The technique enables the imaging of the interactions between virus and host cell. It provides the potential to develop a better understanding of virus-host interactions, and the possibility of discovering previously-unknown interactions.

The objective here was twofold; to construct a CARS microscope and to apply it to an area of biomedical science. The set-up of the microscope (Chapter 3) and the achievement of suitable benchmarks of performance and reliability (Chapter 4) allowed its subsequent application to a virological study (Chapter 5) and demonstrated that this study could be extended to live cells (Chapter 6). This research showed that a combination of CARS and two-photon microscopies can provide high-resolution intracellular images of infected cells. It suggests a link between infection by cytomegalovirus and cytoplasmic accumulations of lipid droplets, however this has yet to be demonstrated conclusively. Additionally, it was discovered that cells in the late stage of infection transport the green fluorescent protein (GFP) from cytoplasm to nucleus, suggesting that the virus significantly disrupts host cell transport pathways.

CARS microscopy is the ideal platform for imaging cellular lipid droplets. Previous methods relied on the use of fluorescent markers which are limited in range, especially for live cell imaging, and are known to cause droplet deformations [74]. CARS circumvents these difficulties and allows label-free imaging of lipid droplets. Recent evidence [143] shows that lipid droplets play an essential role in replication of hepatitis C virus. A better understanding of the mechanisms involved could provide new routes for intervention and treatments of infections. CARS is therefore a crucial tool for investigating the link between viral infection and changes

in lipid droplet metabolism. Imaging lipid droplets alone is not sufficient to elucidate this link, a method is also required to correlate observations with the infection state of the cell. Previous studies have focused on imaging infection progression by transfecting cells with fluorescently-tagged RNA molecules [118]. However the fluorophore molecule is not transcribed into progeny RNA, limiting the lifetime of tagged RNA within the cell [119]. In contrast, this study used a modified virus encoding the GFP gene within the viral genome. CARS microscopy was applied to image the effect of the virus on host cell morphology and lipid droplet distribution whilst two-photon microscopy was used to image GFP expression. As the GFP is produced by the cell itself no exogenous fluorophores are needed. Expression of GFP begins when the cell starts translating viral genes and this provides a definitive indicator of the commencement of infection. It also enables an assessment of the stage of infection by observing the level of GFP expression in the cell.

The principal drawback of CARS microscopy is the presence of the nonresonant background. In this thesis the background limited the application of CARS to the C–H stretch vibration at $2845\,\mathrm{cm}^{-1}$, which produces a particularly strong resonant signal. Whilst the nonresonant background is inherent to CARS there are a variety of methods to suppress or eliminate it. Adapting the microscope for stimulated Raman scattering [6] is one possibility. With the background removed it would be possible to search for other chemical species of interest in infected cells, e.g. the DNA backbone or specific protein bands [109], which lie in the chemically-important fingerprint region. The ideal microscope would be able to image individual viral particles, however this is forbidden by the diffraction limit, a fundamental law of optics. Despite this, recent progress in superresolution techniques [37] suggests that imaging such small particles with light microscopy is not 'as impossible' as once thought, suggesting that light microscopy will continue to play an important role in virological studies.

This thesis concludes with suggestions for future work, from both the physics and the virology perspectives.

The ability to watch an infected cell as the process unfolds would greatly enhance the understanding of the virus-host interactions observed in this study. The potential of the microscope for live cell imaging of infection processes was demonstrated (Chapter 6) by imaging a single cell with CARS over a period of hours. However, cells are very susceptible to photodamage and a systematic study of the causes of this damage is required. This should include the use of cell damage markers and additional optimizations to the laser and microscope systems to reduce the laser power further. The use of a custom-built microscope is advantageous as the system can quickly be adapted *in situ* to meet the changing demands of experiments, or to further explore a particular scientific thread. For example, the integration of extra modalities, such as second harmonic generation for collagen imaging [160], would add further flexibility. The investigation of cytomegalovirus is an ongoing research project, and the contribution of CARS microscopy to this project is continuing. This will allow the further refinement of the techniques involved, and ultimately the extension of this work to other viruses.

The outlook for the field in general is promising. Whilst the cost and complexity of the laser source for CARS remains a significant obstacle to its widespread adoption, recent progress in the development of fibre lasers [35] has moved a step closer to providing a low-cost alignment-free all-fibre light source which can simply be fitted to existing confocal and two-photon microscopes. The removal of this obstacle would immediately stimulate the uptake of the technique by researchers and its integration with many existing laser scanning microscopes. This would enable CARS to be applied more readily in existing research projects. Efforts to reduce or eliminate the nonresonant background have also led to the development of new laser sources, such as specialized lasers for FM-CARS, and to a new technique, stimulated Raman scattering (described in Section 2.6). If the initial promise of this new imaging modality is borne out it could become the future direction of this research field.

Bibliography

[1] S. Inoué and K. R. Spring. *Video Microscopy*. Plenum Press, New York, second edition, 1997.

[2] P. D. Maker and R. W. Terhune. Study of optical effects due to an induced polarization third order in electric field strength. *Phys. Rev.*, 148:990–999, 1965. 10.1103/PhysRev.148.990

[3] M. Duncan, J. Reintjes, and T. Manuccia. Scanning coherent anti-Stokes Raman microscope. *Opt. Lett.*, 7:350–352, 1982. 10.1364/OL.7.000350

[4] A. Zumbusch, G. R. Holtom, and X. S. Xie. Three-dimensional vibrational imaging by coherent anti-Stokes Raman scattering. *Phys. Rev. Lett.*, 82:4142–4145, 1999. 10.1103/PhysRevLett.82.4142

[5] C. L. Evans and X. S. Xie. Coherent anti-Stokes Raman scattering microscopy: Chemical imaging for biology and medicine. *Annu. Rev. Anal. Chem.*, 1:883–909, 2008. 10.1146/annurev.anchem.1.031207.112754

[6] C. W. Freudiger, W. Min, B. G. Saar, S. Lu, G. R. Holtom, C. He, J. C. Tsai, J. X. Kang, and X. S. Xie. Label-free biomedical imaging with high sensitivity by stimulated raman scattering microscopy. *Science*, 322:1857–1861, 2008. 10.1126/science.1165758

[7] B. G. Saar, G. R. Holtom, C. W. Freudiger, C. Ackermann, W. Hill, and X. S. Xie. Intracavity wavelength modulation of an optical parametric oscillator for coherent Raman microscopy. *Opt. Express*, 17:12532–12539, 2009. 10.1364/OE.17.012532

[8] W. Denk, D. W. Piston, and W. W. Webb. Multi-photon molecular excitation in laser-scanning microscopy. In J. B. Pawley, editor, *Handbook of Biological Confocal Microscopy*, pages 535–549. Springer, New York, third edition, 2006.

[9] E. Smith and G. Dent. *Modern Raman Spectroscopy: A Practical Approach*. Wiley, Chichester, 2004.

[10] J. Ferraro, K. Nakamoto, and C. W. Brown. *Introductory Raman Spectroscopy*. Academic Press, San Diego, second edition, 2003.

[11] D. A. Long. *The Raman Effect: A Unified Treatment of the Theory of Raman Scattering by Molecules*. Wiley, Chichester, 2002.

[12] R. W. Boyd. *Nonlinear Optics*. Academic Press, San Diego, third edition, 2008.

[13] H. Lotem, R. T. Lynch, and N. Bloembergen. Interference between Raman resonances in four-wave difference mixing. *Phys. Rev. A*, 14:1748–1755, 1976. 10.1103/PhysRevA.14.1748

[14] J. A. Shirley, R. J. Hall, and A. C. Eckbreth. Folded BOXCARS for rotational Raman studies. *Opt. Lett.*, 5:380–382, 1980. 10.1364/OL.5.000380

[15] G. Bjorklund. Effects of focusing on third-order nonlinear processes in isotropic media. *IEEE J. Quantum Elect.*, 11:287–296, 1975.

[16] R. Gauderon, P. Lukins, and C. Sheppard. Three-dimensional second-harmonic generation imaging with femtosecond laser pulses. *Opt. Lett.*, 23:1209–1211, 1998. 10.1364/OL.23.001209

[17] Y. Barad, H. Eisenberg, M. Horowitz, and Y. Silberberg. Nonlinear scanning laser microscopy by third harmonic generation. *Appl. Phys. Lett.*, 70:922–924, 1997. 10.1063/1.118442

[18] A. Hopt and E. Neher. Highly nonlinear photodamage in two-photon fluorescence microscopy. *Biophys. J.*, 80:2029–2036, 2001. 10.1016/S0006-3495(01)76173-5

[19] J.-X. Cheng and X. S. Xie. Coherent anti-Stokes Raman scattering microscopy: instrumentation, theory, and applications. *J. Phys. Chem. B*, 108:827–840, 2004. 10.1021/jp035693v

[20] W. T. Silfvast. *Laser Fundamentals*. Cambridge University Press, second edition, 2004.

[21] A. M. Weiner. *Ultrafast Optics*. Wiley, Hoboken, 2009.

[22] J.-X. Cheng, A. Volkmer, L. Book, and X. S. Xie. An epi-detected coherent anti-stokes raman scattering (E-CARS) microscope with high spectral resolution and high sensitivity. *J. Phys. Chem. B*, 105:1277–1280, 2001. 10.1021/jp003774a

[23] J. Girkin and G. McConnell. Advances in laser sources for confocal and multiphoton microscopy. *Microsc. Res. Tech.*, 67:8–14, 2005. 10.1002/jemt.20179

[24] X. Nan, E. O. Potma, and X. S. Xie. Nonperturbative chemical imaging of organelle transport in living cells with coherent anti-Stokes Raman scattering microscopy. *Biophys. J.*, 91:728–735, 2006. 10.1529/biophysj.105.074534

[25] M. Hashimoto, T. Araki, and S. Kawata. Molecular vibration imaging in the fingerprint region by use of coherent anti-Stokes Raman scattering microscopy with a collinear configuration. *Opt. Lett.*, 25:1768–1770, 2000. 10.1364/OL.25.001768

[26] L. Ma, R. Shelton, H. Kapteyn, M. Murnane, and J. Ye. Sub-10-femtosecond active synchronization of two passively mode-locked Ti:sapphire oscillators. *Phys. Rev. A*, 64:021802, 2001. 10.1103/PhysRevA.64.021802

[27] E. O. Potma, D. Jones, J.-X. Cheng, X. S. Xie, and J. Ye. High-sensitivity coherent anti-Stokes Raman scattering microscopy with two tightly synchronized picosecond lasers. *Opt. Lett.*, 27:1168–1170, 2002. 10.1364/OL.27.001168

[28] F. Ganikhanov, S. Carrasco, X. S. Xie, M. Katz, W. Seitz, and D. Kopf. Broadly tunable dual-wavelength light source for coherent anti-Stokes Raman scattering microscopy. *Opt. Lett.*, 31:1292–1294, 2006. 10.1364/OL.31.001292

[29] D. Hughes and J. Barr. Laser diode pumped solid state lasers. *J. Phys. D: Appl. Phys.*, 25:563–586, 1992. 10.1088/0022-3727/25/4/001

[30] C. L. Evans, X. Xu, S. Kesari, X. S. Xie, S. T. C. Wong, and G. S. Young. Chemically-selective imaging of brain structures with CARS microscopy. *Opt. Express*, 15:12076–12087, 2007. 10.1364/OE.15.012076

[31] *picoEmerald* specifications sheet. Angewandte Physik und Elektronik GmbH, Berlin, 2009., http://www.ape-berlin.de/pdf/picoEmerald.pdf

[32] N. Dudovich, D. Oron, and Y. Silberberg. Single-pulse coherent anti-Stokes Raman spectroscopy in the fingerprint spectral region. *J. Chem. Phys.*, 118:9208–9215, 2003. 10.1063/1.1568072

[33] E. Andresen, V. Birkedal, J. Thøgersen, and S. Keiding. Tunable light source for CARS microspectroscopy based on the soliton self-frequency shift. *Opt. Lett.*, 31:1328–1330, 2006. 10.1364/OL.31.001328

[34] E. Andresen, C. Nielsen, J. Thøgersen, and S. Keiding. Fiber laser-based light source for coherent anti-Stokes Raman scattering microspectroscopy. *Opt. Express*, 15:4848–4856, 2007. 10.1364/OE.15.004848

[35] A. F. Pegoraro, A. Ridsdale, D. J. Moffatt, J. P. Pezacki, B. K. Thomas, L. Fu, L. Dong, M. E. Fermann, and A. Stolow. All-fiber CARS microscopy of live cells. *Opt. Express*, 17:20700–20706, 2009. 10.1364/OE.17.020700

[36] J. B. Pawley, editor. *Handbook of Biological Confocal Microscopy*. Springer, New York, third edition, 2006.

[37] S. W. Hell. Far-field optical nanoscopy. *Science*, 316:1153–1158, 2007. 10.1126/science.1137395

[38] S. W. Hell and A. Schönle. Nanoscale resolution in far-field fluorescence microscopy. In P. W. Hawkes and J. C. H. Spence, editors, *Science of Microscopy*. Springer, New York, first edition, 2007. 10.1007/978-0-387-49762-4_12

[39] J.-X. Cheng, Y. Jia, G. Zheng, and X. S. Xie. Laser-scanning coherent anti-stokes Raman scattering microscopy and applications to cell biology. *Biophys. J.*, 83:502–509, 2002. 10.1016/S0006-3495(02)75186-2

[40] M. Abramowitz, K. Spring, H. Keller, and M. Davidson. Basic principles of microscope objectives. *BioTechniques*, 33:772–781, 2002.

[41] H. E. Keller. Objective lenses for confocal microscopy. In J. B. Pawley, editor, *Handbook of Biological Confocal Microscopy*. Springer, New York, third edition, 2006.

[42] A. Wright, S. Poland, J. M. Girkin, C. W. F. Freudiger, C. L. Evans, and X. S. Xie. Adaptive optics for enhanced signal in CARS microscopy. *Opt. Express*, 15:18209–18219, 2007. 10.1364/OE.15.018209

[43] J.-X. Cheng, A. Volkmer, and X. S. Xie. Theoretical and experimental characterization of coherent anti-Stokes Raman scattering microscopy. *J. Opt. Soc. Am. B*, 19:1363–1375, 2002. 10.1364/JOSAB.19.001363

[44] C. L. Evans, E. O. Potma, M. Puoris'haag, D. Côté, C. Lin, and X. S. Xie. Chemical imaging of tissue in vivo with video-rate coherent anti-Stokes Raman scattering microscopy. *Proc. Natl. Acad. Sci. USA*, 102:16807–16812, 2005. 10.1073/pnas.0508282102

[45] Hamamatsu Photonics K. K. *Photomultiplier Tubes: Basics and Applications*, 2007. http://sales.hamamatsu.com/assets/pdf/catsandguides/PMT_handbook_v3aE.pdf

[46] M. B. Cannell, A. McMorland, and C. Soeller. Image enhancement by deconvolution. In J. B. Pawley, editor, *Handbook of Biological Confocal Microscopy*, pages 488–499. Springer, New York, third edition, 2006.

[47] B. Roysam, G. Lin, M.-A. Abdul-Karim, O. Al-Kofahi, K. Al-Kofahi, W. Shain, D. H. Szarowski, and J. N. Turner. Automated three-dimensional image analysis methods for confocal microscopy. In J. B. Pawley, editor, *Handbook of Biological Confocal Microscopy*. Springer, New York, third edition, 2006.

[48] J. Oudar, R. Smith, and Y. Shen. Polarization-sensitive coherent anti-Stokes Raman spectroscopy. *Appl. Phys. Lett.*, 34:758, 1979. 10.1063/1.90663

[49] J.-X. Cheng, L. Book, and X. S. Xie. Polarization coherent anti-Stokes Raman scattering microscopy. *Opt. Lett.*, 26:1341–1343, 2001. 10.1364/OL.26.001341

[50] J.-X. Cheng. Coherent anti-Stokes Raman scattering microscopy. *Appl. Spectrosc.*, 61:197A–208A, 2007. 10.1366/000370207781746044

[51] F. Ganikhanov, C. L. Evans, B. Saar, and X. S. Xie. High-sensitivity vibrational imaging with frequency modulation coherent anti-Stokes Raman scattering (FM CARS) microscopy. *Opt. Lett.*, 31:1872–1874, 2006. 10.1364/OL.31.001872

[52] B. von Vacano, T. Buckup, and M. Motzkus. Highly sensitive single-beam heterodyne coherent anti-Stokes Raman scattering. *Opt. Lett.*, 31:2495–2497, 2006. 10.1364/OL.31.002495

[53] E. O. Potma, C. L. Evans, and X. S. Xie. Heterodyne coherent anti-Stokes Raman scattering (CARS) imaging. *Opt. Lett.*, 31:241–243, 2006. 10.1364/OL.31.000241

[54] C. L. Evans, E. O. Potma, and X. S. Xie. Coherent anti-Stokes Raman scattering spectral interferometry: determination of the real and imaginary components of nonlinear susceptibility $\chi^{(3)}$ for vibrational microscopy. *Opt. Lett.*, 29:2923–2925, 2004. 10.1364/OL.29.002923

[55] A. Volkmer. Time-resolved coherent anti-Stokes Raman scattering microscopy: Imaging based on Raman free induction decay. *Appl. Phys. Lett.*, 80, 2002. 10.1063/1.1456262

[56] N. Dudovich, D. Oron, and Y. Silberberg. Single-pulse coherently controlled nonlinear Raman spectroscopy and microscopy. *Nature*, 418:512–514, 2002. 10.1038/nature00933

[57] V. V. Krishnamachari and E. O. Potma. Focus-engineered coherent anti-Stokes Raman scattering microscopy: a numerical investigation. *J. Opt. Soc. Am. A*, 24:1138–1147, 2007. 10.1364/JOSAA.24.001138

[58] J.-X. Cheng, A. Volkmer, L. Book, and X. S. Xie. Multiplex coherent anti-stokes Raman scattering microspectroscopy and study of lipid vesicles. *J. Phys. Chem. B*, 106:8493–8498, 2002. 10.1021/jp025771z

[59] M. Bonn, M. Müller, H. Rinia, and K. Burger. Imaging of chemical and physical state of individual cellular lipid droplets using multiplex CARS microscopy. *J. Raman Spectrosc.*, 40:763–769, 2009. 10.1002/jrs.2253

[60] E. Vartiainen, H. Rinia, M. Muller, and M. Bonn. Direct extraction of Raman line-shapes from congested CARS spectra. *Opt. Express*, 14:3622–3630, 2006. 10.1364/OE.14.003622

[61] T. T. Le, C. W. Rehrer, T. B. Huff, M. B. Nichols, I. G. Camarillo, and J.-X. Cheng. Nonlinear optical imaging to evaluate the impact of obesity on mammary gland and tumor stroma. *Mol. Imaging*, 6:205–211, 2007.

[62] T. T. Le, I. M. Langohr, M. J. Locker, M. Sturek, and J.-X. Cheng. Label-free molecular imaging of atherosclerotic lesions using multimodal nonlinear optical microscopy. *J. Biomed. Opt.*, 12:054007, 2007. 10.1117/1.2795437

[63] H. Wang, Y. Fu, P. Zickmund, R. Shi, and J.-X. Cheng. Coherent anti-stokes Raman scattering imaging of axonal myelin in live spinal tissues. *Biophys. J.*, 89:581–591, 2005. 10.1529/biophysj.105.061911

[64] E. O. Potma and X. S. Xie. Direct visualization of lipid phase segregation in single lipid bilayers with coherent anti-Stokes Raman scattering microscopy. *ChemPhysChem*, 6:77–79, 2005. 10.1002/cphc.200400390

[65] H.-W. Wang, T. T. Le, and J.-X. Cheng. Label-free imaging of arterial cells and extracellular matrix using a multimodal CARS microscope. *Opt. Commun.*, 281:1813–1822, 2008. 10.1016/j.optcom.2007.07.067

[66] S. Tang, T. Krasieva, Z. Chen, G. Tempea, and B. Tromberg. Effect of pulse duration on two-photon excited fluorescence and second harmonic generation in nonlinear optical microscopy. *J. Biomed. Opt.*, 11:020501, 2006. 10.1117/1.2177676

[67] H. Chen, H. Wang, M. N. Slipchenko, Y. Jung, Y. Shi, J. Zhu, K. K. Buhman, and J.-X. Cheng. A multimodal platform for nonlinear optical microscopy and microspectroscopy. *Opt. Express*, 17:1282–1290, 2009. 10.1364/OE.17.001282

[68] A. Pegoraro, A. Ridsdale, D. Moffatt, and Y. Jia. Optimally chirped multimodal CARS microscopy based on a single Ti:sapphire oscillator. *Opt. Express*, 17:2984–2996, 2009. 10.1364/OE.17.002984

[69] E. O. Potma, X. S. Xie, L. Muntean, J. Preusser, D. Jones, J. Ye, S. Leone, W. Hinsberg, and W. Schade. Chemical imaging of photoresists with coherent anti-Stokes Raman scattering (CARS) microscopy. *J. Phys. Chem. B*, 108:1296–1301, 2004. 10.1021/jp030903p

[70] B. G. Saar, H.-S. Park, X. S. Xie, and O. D. Lavrentovich. Three-dimensional imaging of chemical bond orientation in liquid crystals by coherent anti-stokes Raman scattering microscopy. *Opt. Express*, 15:13585–13596, 2007. 10.1364/OE.15.013585

[71] A. Volkmer. Vibrational imaging and microspectroscopies based on coherent anti-Stokes Raman scattering microscopy. *J. Phys. D: Appl. Phys.*, 38:R59–R81, 2005. 10.1088/0022-3727/38/5/R01

[72] E. O. Potma and X. S. Xie. Detection of single lipid bilayers with coherent anti-Stokes Raman scattering (CARS) microscopy. *J. Raman Spectrosc.*, 34:642–650, 2003. 10.1002/jrs.1045

[73] X. Nan, J.-X. Cheng, and X. S. Xie. Vibrational imaging of lipid droplets in live fibroblast cells with coherent anti-Stokes Raman scattering microscopy. *J. Lipid Res.*, 44:2202–2208, 2003. 10.1194/jlr.D300022-JLR200

[74] S. Fukumoto and T. Fujimoto. Deformation of lipid droplets in fixed samples. *Histochem. Cell Biol.*, 118:423–428, 2002. 10.1007/s00418-002-0462-7

[75] Y. Fu, H. Wang, R. Shi, and J.-X. Cheng. Characterization of photodamage in coherent anti-Stokes Raman scattering microscopy. *Opt. Express*, 14:3942–3951, 2006. 10.1364/OE.14.003942

[76] Y. Fu, H. Wang, T. B. Huff, R. Shi, and J.-X. Cheng. Coherent anti-stokes Raman scattering imaging of myelin degradation reveals a calcium-dependent pathway in lyso-PtdCho-induced demyelination. *J. Neurosci. Res.*, 85:2870–2881, 2007. 10.1002/jnr.21403

[77] H. Wang, T. B. Huff, Y. Fu, K. Y. Jia, and J.-X. Cheng. Increasing the imaging depth of coherent anti-Stokes Raman scattering microscopy with a miniature microscope objective. *Opt. Lett.*, 32:2212–2214, 2007. 10.1364/OL.32.002212

[78] K. M. Hanson and C. J. Bardeen. Application of nonlinear optical microscopy for imaging skin. *Photochem. Photobiol.*, 85:33–44, 2009. 10.1111/j.1751-1097.2008.00508.x

[79] F. Légaré, C. L. Evans, F. Ganikhanov, and X. S. Xie. Towards CARS Endoscopy. *Opt. Express*, 14:4427–4432, 2006. 10.1364/OE.14.004427

[80] H. Wang, T. Huff, and J.-X. Cheng. Coherent anti-Stokes Raman scattering imaging with a laser source delivered by a photonic crystal fiber. *Opt. Lett.*, 31:1417–1419, 2006. 10.1364/OL.31.001417

[81] P. Nandakumar, A. Kovalev, and A. Volkmer. Vibrational imaging based on stimulated Raman scattering microscopy. *New J. Phys.*, 11:033026, 2009. 10.1088/1367-2630/11/3/033026

[82] Coherent Inc., Santa Clara. *Operator's Manual for the Coherent Mira Optima 900-P Laser*, revision AA, 2004.

[83] Coherent Inc., Santa Clara. *Operator's Manual for the Mira Synchrolock*, revision AA, 2002.

[84] J. Kafka, M. Watts, and J.-W. Pieterse. Picosecond and femtosecond pulse generation in a regeneratively mode-locked Ti:sapphire laser. *IEEE J. Quantum Elect.*, 28:2151–2162, 1992. 10.1109/3.159524

[85] R. Schermaul. The climatic effects of water vapour. *Physics World*, 2003. http://physicsworld.com/cws/article/print/17402/3

[86] S. Crooker, F. Betz, J. Levy, and D. Awschalom. Femtosecond synchronization of two passively mode-locked Ti:sapphire lasers. *Rev. Sci. Instrum.*, 67:2068–2071, 1996. 10.1063/1.1147016

[87] A. Yu, X. Ye, D. Ionascu, W. Cao, and P. Champion. Two-color pump-probe laser spectroscopy instrument with picosecond time-resolved electronic delay and extended scan range. *Rev. Sci. Instrum.*, 76:114301, 2005. 10.1063/1.2126808

[88] R. Kaindl, M. Wurm, K. Reimann, P. Hamm, A. Weiner, and M. Woerner. Generation, shaping, and characterization of intense femtosecond pulses tunable from 3 to 20 μm. *J. Opt. Soc. Am. B*, 17:2086–2094, 2000. 10.1364/JOSAB.17.002086

[89] D. Jones, E. Potma, J.-X. Cheng, B. Burfeindt, Y. Pang, J. Ye, and X. Xie. Synchronization of two passively mode-locked, picosecond lasers within 20 fs for coherent anti-Stokes Raman scattering microscopy. *Rev. Sci. Instrum.*, 73:2843–2848, 2002. 10.1063/1.1492001

[90] D. Spence, W. Sleat, J. Evans, W. Sibbett, and J. Kafka. Time synchronisation measurements between 2 self-modelocked Ti:sapphire lasers. *Opt. Commun.*, 101:286–296, 1993. 10.1016/0030-4018(93)90378-I

[91] Synchrolock test data sheet. Provided by Coherent Inc., Santa Clara, 2006.

[92] Y. Takagi, T. Kobayashi, K. Yoshihara, and S. Imamura. Multiple- and single-shot autocorrelator based on two-photon conductivity in semiconductors. *Opt. Lett.*, 17:658–660, 1992. 10.1364/OL.17.000658

[93] T. Minamikawa, N. Tanimoto, M. Hashimoto, T. Araki, M. Kobayashi, K. Fujita, and S. Kawata. Jitter reduction of two synchronized picosecond mode-locked lasers using balanced cross-correlator with two-photon detectors. *Appl. Phys. Lett.*, 89:191101, 2006. 10.1063/1.2374803

[94] E. H. K. Stelzer. The intermediate optical system of laser-scanning confocal microscopes. In J. B. Pawley, editor, *Handbook of Biological Confocal Microscopy*, pages 207–220. Springer, New York, 2006.

[95] J. M. Khosrofian and B. A. Garetz. Measurement of a Gaussian laser-beam diameter through the direct inversion of knife-edge data. *Appl. Optics*, 22:3406–3410, 1983. 10.1364/AO.22.003406

[96] D. Wokosin. Nikon lens transmission. Data sheet provided by Bio-Rad Laboratories, Hercules.

[97] Filter spectral transmission data. Provided by Chroma Technology Corp., Bellows Falls., http://www.chroma.com/

[98] D. T. Reid. Ultrafast Photonics. Lecture notes from Heriot–Watt University, Edinburgh.

[99] C. L. Evans, E. O. Potma, X. Nan, W. Y. Yang, F. Ganikanhov, S. Carrasco, B. G. Saar, H. Chen, and X. S. Xie. The Third Annual CARS Workshop Manual. Harvard University, 2006.

[100] J. Moger, B. D. Johnston, and C. R. Tyler. Imaging metal oxide nanoparticles in biological structures with CARS microscopy. *Opt. Express*, 16:3408–3419, 2008. 10.1364/OE.16.003408

[101] S. Inoué and R. Oldenbourg. Microscopes. In M. Bass, editor, *Handbook of Optics Volume II*. McGraw-Hill, second edition, 1995.

[102] R. I. Freshney. *Culture of Animal Cells*. Wiley-Liss, Chichester, third edition, 1994.

[103] V. G. George, J. C. Hierholzer, and E. W. Ades. Cell culture. In H. O. Kangro and B. W. J. Mahy, editors, *Virology Methods Manual*, pages 3–24. Academic Press, London, 1996.

[104] Y. Guo, K. R. Cordes, R. V. Farese, and T. C. Walther. Lipid droplets at a glance. *J. Cell Sci.*, 122:749–752, 2009. 10.1242/jcs.037630

[105] T. Fujimoto, Y. Ohsaki, J. Cheng, M. Suzuki, and Y. Shinohara. Lipid droplets: a classic organelle with new outfits. *Histochem. Cell Biol.*, 130:263–279, 2008. 10.1007/s00418-008-0449-0

[106] H. Eagle. Nutrition needs of mammalian cells in tissue culture. *Science*, 122:501–504, 1955. 10.1126/science.122.3168.501

[107] G. J. Todaro and H. Green. Quantitative studies of the growth of mouse embryo cells in culture and their development into established lines. *J. Cell Biol.*, 17:299–313, 1963. 10.1083/jcb.17.2.299

[108] R. I. Menzies. A Raman spectroscopic study of healthy and infected fibroblast cells. Master's thesis, University of Edinburgh, 2009.

[109] M. A. Ochsenkühn, P. R. T. Jess, H. Stoquert, K. Dholakia, and C. J. Campbell. Nanoshells for Surface-Enhanced Raman Spectroscopy in Eukaryotic Cells: Cellular Response and Sensor Development. *ACS Nano*, 3:3613–3621, 2009. 10.1021/nn900681c

[110] R. Irvine. Nuclear lipid signalling. *Nature Rev. Mol. Cell Biol.*, 4:349–360, 2003. 10.1038/nrm1100

[111] J. Aguilar, M. Lera, and C. Sheppard. Imaging of spheres and surface profiling by confocal microscopy. *Appl. Optics*, 39:4621–4628, 2000. 10.1364/AO.39.004621

[112] W. Weise, P. Zinin, T. Wilson, G. Briggs, and S. Boseck. Imaging of spheres with the confocal scanning optical microscope. *Opt. Lett*, 21:1800–1802, 1996. 10.1364/OL.21.001800

[113] W. S. Rasband. *ImageJ*. U. S. National Institutes of Health, Bethesda, Maryland, 1997–2009. http://rsb.info.nih.gov/ij/

[114] E. S. Mocarski, T. Shenk, and R. F. Pass. Cytomegaloviruses. In D. M. Knipe and P. M. Howley, editors, *Fields Virology*, pages 2702–2772. Lippincott Williams and Wilkins, Philadelphia, fifth edition, 2006.

[115] W. L. Drew. Cytomegalovirus infection in patients with AIDS. *Clin. Infect. Dis.*, 14:608–615, 1992.

[116] T. C. Merigan and S. Resta. Cytomegalovirus: where have we been and where are we going? *Rev. Infect. Dis.*, 12:S693–S700, 1990.

[117] C. Sweet. The pathogenicity of cytomegalovirus. *FEMS Microbiol. Rev.*, 23:457–482, 1999.

[118] X. Nan, A. M. Tonary, A. Stolow, X. S. Xie, and J. P. Pezacki. Intracellular imaging of HCV RNA and cellular lipids by using simultaneous two-photon fluorescence and coherent anti-Stokes Raman scattering microscopies. *ChemBioChem*, 7:1895–1897, 2006. 10.1002/cbic.200600330

[119] R. Lyn, D. Kennedy, S. Sagan, D. Blais, Y. Roleau, A. F. Pegoraro, X. S. Xie, A. Stolow, and J. P. Pezacki. Direct imaging of the disruption of hepatitis C virus replication complexes by inhibitors of lipid metabolism. *Virology*, 394:130–142, 2009. 10.1016/j.virol.2009.08.022

[120] R. Tsien. The green fluorescent protein. *Annu. Rev. Biochem.*, 67:509–544, 1998. 10.1146/annurev.biochem.67.1.509

[121] D. M. Knipe and P. M. Howley. *Fields Virology*. Lippincott Williams and Wilkins, Philadelphia, fifth edition, 2006.

[122] A. J. Levine and L. W. Enquist. History of virology. In D. M. Knipe and P. M. Howley, editors, *Fields Virology*, pages 3–23. Lippincott Williams and Wilkins, Philadelphia, fifth edition, 2006.

[123] R. C. Condit. Principles of virology. In D. M. Knipe and P. M. Howley, editors, *Fields Virology*, pages 25–57. Lippincott Williams and Wilkins, Philadelphia, fifth edition, 2006.

[124] B. D. Lindenbauch, M. J. Evans, A. J. Syder, B. Wolk, T. L. Tellinghuisen, C. C. Liu, T. Maruyama, R. O. Hynes, D. R. Burton, J. A. McKeating, and C. M. Rice. Complete replication of hepatitis C virus in cell culture. *Science*, 309:623–626, 2005. 10.1126/science.1114016

[125] L. Collier and J. Oxford. *Human Virology*. Oxford University Press, third edition, 2006.

[126] S. C. Harrison. Principles of virus structure. In D. M. Knipe and P. M. Howley, editors, *Fields Virology*, pages 59–98. Lippincott Williams and Wilkins, Philadelphia, fifth edition, 2006.

[127] X. Zhang, E. Settembre, C. Xu, P. R. Dormitzer, R. Bellamy, S. C. Harrison, and N. Grigorieff. Near-atomic resolution using electron cryomicroscopy and single-particle reconstruction. *Proc. Natl. Acad. Sci. USA*, 105:1867–1872, 2008. 10.1073/pnas.0711623105

[128] I. L. Chrystie. Electron microscopy. In H. O. Kangro and B. W. J. Mahy, editors, *Virology Methods Manual*, pages 91–106. Academic Press, London, 1996.

[129] F. Mattes, J. McLaughlin, V. Emery, D. Clark, and P. Griffiths. Histopathological detection of owl's eye inclusions is still specific for cytomegalovirus in the era of human herpesviruses 6 and 7. *J. Clin. Pathol.*, 53:612–614, 2000. 10.1136/jcp.53.8.612

[130] C. Joo, H. Balci, Y. Ishitsuka, C. Buranachai, and T. Ha. Advances in single-molecule fluorescence methods for molecular biology. *Annu. Rev. Biochem.*, 77:51–76, 2008. 10.1146/annurev.biochem.77.070606.101543

[131] G. Seisenberger, M. Ried, T. Endress, H. Buning, M. Hallek, and C. Brauchle. Real-time single-molecule imaging of the infection pathway of an adeno-associated virus. *Science*, 294:1929–1932, 2001. 10.1126/science.1064103

[132] P. E. Pellett and B. Roizman. The family *Herpesviridae*: a brief introduction. In D. M. Knipe and P. M. Howley, editors, *Fields Virology*, pages 2479–2499. Lippincott Williams and Wilkins, Philadelphia, fifth edition, 2006.

[133] A. Dolan, C. Cunningham, R. Hector, A. Hassan-Walker, L. Lee, C. Addison, D. Dargan, D. McGeoch, D. Gatherer, V. Emery, P. Griffiths, C. Sinzger, B. McSharry, G. Wilkinson, and A. Davison. Genetic content of wild-type human cytomegalovirus. *J. Gen. Virol.*, 85:1301–1312, 2004. 10.1099/vir.0.79888-0

[134] T. C. Mettenleiter, B. G. Klupp, and H. Granzow. Herpesvirus assembly: an update. *Virus. Res.*, 143:222–234, 2009. 10.1016/j.virusres.2009.03.018

[135] B. Alberts, A. Johnson, J. Lewis, M. Raff, K. Roberts, and P. Walter. *Molecular Biology of the Cell*. Garland Science, New York, fourth edition, 2002.

[136] T. C. Mettenleiter, B. G. Klupp, and H. Granzow. Herpesvirus assembly: a tale of two membranes. *Curr. Opin. Microbiol.*, 9:423–429, 2006. 10.1016/j.mib.2006.06.013

[137] S. Das, A. Vasanji, and P. E. Pellettl. Three-dimensional structure of the human cytomegalovirus cytoplasmic virion assembly complex includes a reoriented secretory apparatus. *J. Virol.*, 81:11861–11869, 2007. 10.1128/JVI.01077-07

[138] S. Pepperl, J. Munster, M. Mach, J. Harris, and B. Plachter. Dense bodies of human cytomegalovirus induce both humoral and cellular immune responses in the absence of viral gene expression. *J. Virol.*, 74:6132–6146, 2000.

[139] M. Bain and J. Sinclair. The S phase of the cell cycle and its perturbation by human cytomegalovirus. *Rev. Med. Virol.*, 17:423–434, 2007. 10.1002/rmv.551

[140] L. Hertel and E. S. Mocarski. Global analysis of host cell gene expression late during cytomegalovirus infection reveals extensive dysregulation of cell cycle gene expression and induction of pseudomitosis independent of US28 function. *J. Virol.*, 78:11988–12011, 2004. 10.1128/JVI.78.21.11988-12011.2004

[141] A. L. McCormick and E. S. Mocarski. Viral modulation of the host response to infection. In A. Arvin, G. Campadelli-Fiume, E. S. Mocarski, P. S. Moore, B. Roizman, R. Whitley, and K. Yamanishi, editors, *Human Herpesviruses: Biology, Therapy, and Immunoprophylaxis*, pages 324–337. Cambridge University Press, 2007.

[142] B. Helms. Host-pathogen interactions: Lipids grease the way. *Eur. J. Lipid Sci. Technol.*, 108:895–897, 2006. 10.1002/ejlt.200600194

[143] J. McLauchlan. Lipid droplets and hepatitis C virus infection. *Biochim. Biophys. Acta*, 1791:552–559, 2009. 10.1016/j.bbalip.2008.12.012

[144] L. M. Smith, A. R. McWhorter, L. L. Masters, G. R. Shellam, and A. J. Redwood. Laboratory strains of murine cytomegalovirus are genetically similar to but phenotypically distinct from wild strains of virus. *J. Virol.*, 82:6689–6696, 2008. 10.1128/JVI.00160-08

[145] A. Angulo, P. Ghazal, and M. Messerle. The major immediate-early gene ie3 of mouse cytomegalovirus is essential for viral growth. *J. Virol.*, 74:11129–11136, 2000.

[146] Filter spectral transmission data. Provided by Semrock Inc., Rochester., http://www.semrock.com/

[147] G. Patterson, R. Day, and D. W. Piston. Fluorescent protein spectra. *J. Cell Sci.*, 114:837–838, 2001.

[148] J. Bewersdorf and S. Hell. Picosecond pulsed two-photon imaging with repetition rates of 200 and 400 MHz. *J. Microsc.*, 191:28–38, 1998. 10.1046/j.1365-2818.1998.00379.x

[149] P. Lischka, O. Rosorius, E. Trommer, and T. Stamminger. A novel transferable nuclear export signal mediates CRM1-independent nucleocytoplasmic shuttling of the human cytomegalovirus transactivator protein pUL69. *EMBO J.*, 20:7271–7283, 2001. 10.1093/emboj/20.24.7271

[150] M. A. Rizzo and D. W. Piston. Fluorescent protein tracking and detection. In R. D. Goldman and D. L. Spector, editors, *Live Cell Imaging: A Laboratory Manual*, pages 3–23. Cold Spring Harbor Laboratory Press, 2005.

[151] M. E. Dailey, D. C. Focht, A. Khodjakov, C. L. Rieder, K. R. Spring, N. S. Claxton, S. G. Olenych, J. D. Griffin, and M. W. Davidson. Maintaining live cells on the microscope stage. In *MicroscopyU*. Nikon Corp. http://www.microscopyu.com/articles/livecellimaging/livecellmaintenance.html

[152] P. Watson. Live cell imaging for target and drug discovery. *Drug News Perspect.*, 22:69–79, 2009. 10.1358/dnp.2009.22.2.1334450

[153] M. E. Dailey, D. C. Focht, A. Khodjakov, C. L. Rieder, K. Spring, N. S. Claxton, S. G. Olenych, J. D. Griffin, and M. W. Davidson. Culture chambers for live-cell imaging. In *MicroscopyU*. Nikon Corp. http://www.microscopyu.com/articles/livecellimaging/culturechambers.html

[154] G. Sluder, J. J. Nordberg, F. J. Miller, and E. H. Hinchcliffe. A sealed preparation for long-term observations of cultured cells. In R. D. Goldman and D. L. Spector, editors, *Live Cell Imaging: A Laboratory Manual*, pages 345–349. Cold Spring Harbor Laboratory Press, 2005.

[155] D. Stevenson, D. Carnegie, B. Agate, F. Gunn-Moore, and K. Dholakia. Long-term cell culture on a microscope stage: the Carrel Flask revisited. *Microsc. Anal.*, 123:9, 2008.

[156] J. Art. Photon detectors for confocal microscopy. In J. B. Pawley, editor, *Handbook of Biological Confocal Microscopy*. Springer, New York, fifth edition, 2006.

[157] J. B. Pawley. Points, pixels, and gray levels: digitizing image data. In J. B. Pawley, editor, *Handbook of Biological Confocal Microscopy*, pages 59–79. Springer, New York, fifth edition, 2006.

[158] H. Wang, Y. Fu, and J.-X. Cheng. Experimental observation and theoretical analysis of Raman resonance-enhanced photodamage in coherent anti-Stokes Raman scattering microscopy. *J. Opt. Soc. Am. B*, 24:544–552, 2007. 10.1364/JOSAB.24.000544

[159] J. R. Swedlow, P. D. Andrews, and M. Platani. In vivo imaging of mammalian cells. In R. D. Goldman and D. L. Spector, editors, *Live Cell Imaging: A Laboratory Manual*, pages 329–343. Cold Spring Harbor Laboratory Press, 2005.

[160] P.-F. Lee, A. T. Yeh, and K. J. Bayless. Nonlinear optical microscopy reveals invading endothelial cells anisotropically alter three-dimensional collagen matrices. *Exp. Cell Res.*, 315:396–410, 2009. 10.1016/j.yexcr.2008.10.040

A

Publication

J. Biophoton. **3**, No. 3, 138–146 (2010) / **DOI** 10.1002/jbio.200910054

Journal of
BIOPHOTONICS

FULL ARTICLE

Intracellular imaging of host-pathogen interactions using combined CARS and two-photon fluorescence microscopies

Iain Robinson[**,1], *Michael Andreas Ochsenkühn*[2], *Colin J. Campbell*[2,3], *Gerard Giraud*[1], *William J. Hossack*[1], *Jochen Arlt*[1], *and Jason Crain*[*,1,4]

[1] Collaborative Optical Spectroscopy, Micromanipulation and Imaging Centre (COSMIC), School of Physics and Astronomy, The University of Edinburgh, Mayfield Road, Edinburgh EH9 3JZ, UK
[2] School of Chemistry, The University of Edinburgh, West Mains Road, Edinburgh EH9 3JJ, UK
[3] Division of Pathway Medicine, The University of Edinburgh, Edinburgh EH16 4SB, UK
[4] National Physical Laboratory, Hampton Road, Teddington, Middlesex, TW11 0LW, UK

Received 1 July 2009, revised 27 July 2009, accepted 28 July 2009
Published online 11 August 2009

Key words: CARS, cytomegalovirus, lipids, multimodal microscopy, TPF

PACS: 42.62.Be, 42.65.Dr, 87.14.Cc, 87.64.Vv

Intracellular imaging is a key tool in the investigation of host-pathogen interactions. Advances in this area are particularly sought to understand the effect of viral infection processes on the host cell and its metabolic functions including those cases where host cell lipid metabolism is modulated as a result of infection. We demonstrate the use of combined coherent anti-Stokes Raman scattering (CARS) and two-photon fluorescence microscopies to image fibroblast cells infected by cytomegalovirus. CARS is used to image the host cell membrane, lipid droplets and morphology of the nucleus. Cell nuclei are found to expand during infection, approximately doubling in area. Some cells also show accumulations of lipid droplets at the nuclear periphery. Using a genetically modified virus strain expressing the green fluorescent protein also enables two-photon imaging of the same cells to reveal the location, nature and extent of viral protein expression.

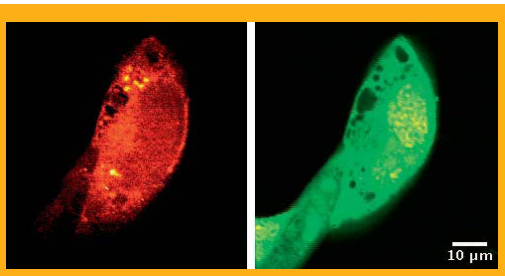

Left: Infected NIH/3T3 fibroblast cell imaged with CARS microscopy at the C–H stretching vibration showing lipid droplets and membranes. Right: Two-photon fluorescence image of the same cell. GFP expression by the cell confirms viral infection.

* Corresponding author: e-mail: j.crain@ed.ac.uk, Phone: +44 131 650 5265, Fax: +44 131 650 5902
** e-mail iain@physics.org, Phone: +44 131 650 5263, Fax: +44 131 650 5902

1. Introduction

Biomedical research is placing increasing demands on cell imaging techniques for improved resolution, sensitivity and chemical detail to enable critical insight into the nature and dynamics of cell function. Important applications have been reported in medical diagnosis [1, 2] and drug discovery [3].

Confocal laser scanning microscopy has been the key tool driving progress in the understanding of cellular processes. It provides chemical specificity through fluorescence labelling and has 3-D optical sectioning capability. Advances based on nonlinear microscopy led to the demonstration and adoption of two-photon imaging [4], which has brought significant advantages over standard confocal imaging, including greater depth penetration and reduced photobleaching. Despite the power and widespread use of these methods, problems inherent to fluorescent labelling persist. These include the extra time and effort required in sample preparation, contamination of images from autofluorescence background signals, photobleaching with associated production of toxic photoproducts and unpredictable disruption to biochemical pathways [5]. As a result, there is intense interest in imaging modalities that avoid the need for fluorescent labelling. Second harmonic generation microscopy can image unlabelled samples [6], but it is limited to structured specimens such as collagen [7]. Spontaneous Raman imaging generates contrast from inherent molecular vibrations, however the intrinsically weak Raman signal necessitates long acquisition times, typically several minutes per spectrum [8]. More recently, the nonlinear coherent anti-Stokes Raman scattering (CARS) process has been used to substantially enhance the vibrational signal.

Imaging based on the CARS process received revived interest in 1999 with the development by Zumbush et al. of a microscope using a pump-Stokes collinear beam geometry and tight focusing of the beams into the sample with a high numerical aperture microscope objective lens [9]. The enhanced vibrational signal enables imaging at speeds up to video-rate [10]. To implement a microscope based on CARS a light source is required which can deliver short pulses at the pump and Stokes wavelengths which are overlapped in the sample. The development of laser systems which meet these demands is a significant technical challenge and a variety of solutions have been applied [9, 11]. Advances in this area have led to simpler, more compact laser sources [12, 13]. Whilst the ability to image label-free samples is the clear advantage of CARS microscopy it also has other beneficial features. Due to the nonlinear nature of the scattering process it has inherent optical sectioning capability and can be used to record stacks of images through thick samples. Additionally, the CARS signal is blue-shifted relative to the excitation wavelengths and can easily be separated from any autofluorescence. However, unlike fluorescence microscopy, CARS excitation also produces a nonresonant background along with the resonant CARS signal. Efforts to reduce or eliminate this background can improve the sensitivity of CARS imaging [14].

CARS microscopy is finding new areas of application in biomedical imaging and clinical diagnosis [15], especially when combined with more established methods [16]. The use of CARS alongside other nonlinear imaging techniques on the same microscope makes a versatile multimodal imaging platform [17, 18]. The system we describe here is capable of performing both CARS and two-photon fluorescence imaging by using the Stokes wavelength as the fluorescence excitation source. Most nonlinear imaging techniques require ultrashort pulses, typically 200 fs duration, to provide the high peak powers needed to generate significant signal intensity. For CARS though, the ratio of the resonant signal to the nonresonant background depends on the pulse duration with the ideal balance in the range 1–2 ps [19, 20]. Although such pulses will yield lower fluorescence signal for two-photon imaging, longer-duration pulses, even up to continuous wave, have been successfully applied [21].

In this paper we discuss the benefits that arise from using multimodal microscopy to probe the complex relationship between a cell and a virus. The diagnosis of diseases and the development of new therapies rely heavily on the understanding at a molecular level of the host-pathogen interactions. Recently, a number of publications have reported the important role of lipids at various stages of cell infection and virus replication [22, 23]. A CARS microscope is the ideal platform for studying the behaviour and chemistry of cellular lipid droplets [24]. Lipid droplets are abundant with C–H bonds which have a strong Raman-active vibration at 2845 cm^{-1} providing high contrast in images. For example, CARS microscopy has been used in the study of cells infected with hepatitis C virus to image rearrangements of cellular lipid droplets that occur during the infection process [25, 26]. By tagging the viral RNA with a fluorescent marker and imaging with two-photon and CARS, both the virus and lipid droplets can be tracked simultaneously. However, fluorescent labels attached to RNA are not transcribed into new viral particles. Consequently there is a steady decline in fluorescence signal from the viral RNA following the initial infection.

Here, we propose a method to track virus activity by two-photon imaging of green fluorescent protein (GFP) whilst recording changes in lipid droplet distribution and membrane morphologies with CARS. By using a modified version of the Smith strain

Journal of BIOPHOTONICS

which expresses GFP under the control of the immediate-early promoter 3 [27], infected cells will exhibit fluorescence as soon as they begin translation of the viral mRNA. In most instances the modified genetic code will persist in the DNA of newly-synthesised viruses. Thus viral progeny will retain the ability to express GFP in cells which they subsequently infect allowing continual monitoring of the viral progression even after extended periods since the initial infection. We use mouse cytomegalovirus, a herpesvirus, modified for GFP expression. The human strain of this virus is endemic and found in more than 40–80% of the worlds population aged over 40 years. The latent virus can lead to severe infection in immunodeficient individuals, e.g. the elderly or HIV positive. In prenatal infections it can lead to loss of hearing and is also connected to congenital blindness [28].

In order to demonstrate the power of combining CARS and two-photon imaging we examine NIH/3T3 fibroblast cells since they are permissive to infection by cytomegalovirus [29, 30] and they contain a large number of lipid droplets, providing high contrast in images [31].

2. Experimental

2.1 Sample preparation

NIH/3T3 fibroblast cells with a passage number of 11–20 were grown in Dulbeccos modified Eagles Medium supplemented with L-glutamine (200 mol/m^3), penicillin/streptomycin (10 000 units/ml) and 10% calf serum and incubated in standard growth conditions at 37 °C in a 5% CO_2 atmosphere. The cells were seeded on 0.12-millimetre-thick glass cover-slips at 50% confluence for 12 h at standard growth conditions. Cells were then fixed with 1% formaldehyde in phosphate buffered saline (PBS) for 15 min at room temperature, washed three times with PBS and stored in a dry environment at 4 °C. PBS was used to wet the samples for imaging.

Infections with mouse cytomegalovirus wild type mutant C3X (MCMV) or a genetically modified version of the Smith strain expressing GFP (MCMV-GFP) were conducted at a multiplicity of infection of 1, resulting in one viral particle per seeded cell, with media containing 3% calf serum to reduce cell growth. Seeding was followed by a synchronisation step keeping cells for 1 h at 4 °C before incubation for 48 h at 37 °C. Cells were then washed twice with PBS, fixed, and stored, as described above. Fluorescent samples were kept in dark conditions.

2.2 Imaging instrumentation

A custom-built laser-scanning inverted microscope was used to record images. A diagram of the setup is shown in Figure 1. The pump and Stokes frequencies, ω_p and ω_s, are provided by a pair of titanium-sapphire lasers (Mira 900, Coherent). The pump laser is tuned to 714 nm, the Stokes to 896 nm, to give a frequency difference $\omega_p - \omega_s$ of 2845 cm^{-1} which matches the aliphatic C–H vibration in lipids. The two beams are combined collinearly and focused into the sample with a 60x water immersion microscope objective lens (Plan Apo 1.20 numerical aperture, Nikon). The CARS signal arises from an anti-Stokes transition with frequency $\omega_{as} = 2\omega_p - \omega_s$ (inset, Figure 1). The wavelength of the signal is therefore blue-shifted relative to the pump and Stokes wavelengths. It is separated by reflection from a long wave pass dichroic mirror (683dcxr, Chroma), and further filtered with two band pass filters (HQ590/20, Chroma). A photomultiplier tube (R3896, Hamamatsu) is used to detect the signal. The tube can be positioned for forward (F-CARS) or backward

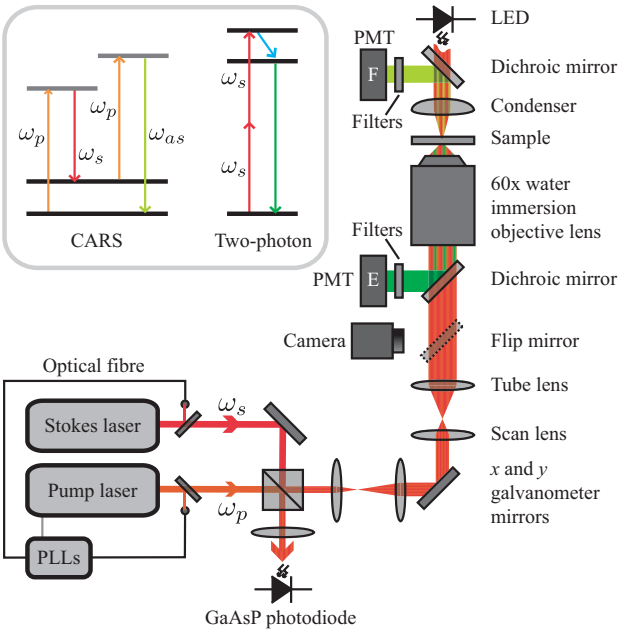

Figure 1 Diagram of a setup for CARS and two-photon imaging. The Stokes laser is tuned to 896 nm, the pump to 714 nm, giving a Raman shift of 2845 cm^{-1}. The lasers are synchronised by two phase-locked loops (PLLs). Phase synchronisation is monitored with a GaAsP photodiode. The beams are scanned by a pair of galvanometer mirrors. A photomultiplier tube (PMT) is used for forward (F) detection of the CARS signal or backward (E) detection of CARS or fluorescence. An LED provides illumination for bright field imaging. **Inset:** Energy diagrams for the CARS and two-photon processes showing the pump ω_p, Stokes ω_s and anti-Stokes ω_{as} (CARS) frequencies.

(E-CARS) detection. The beams are scanned in the sample plane with a pair of galvanometer mirrors (Cambridge Technology). Bright field images are recorded with a CCD camera under illumination by an infrared LED.

The pump and Stokes lasers are synchronised with a phase-locked loop system (Synchrolock, Coherent). Both lasers are mode-locked, emitting pulses of 2 ps duration. Each laser has a repetition rate of around 80 MHz; however, for CARS imaging the two repetition rates, which depend on the laser cavity lengths, must be precisely synchronised. To achieve this, the lasers are set up in a master-and-slave configuration: the Stokes laser is free-running whilst the cavity length of the pump laser is actively adjusted to match it [32]. A repetition rate error signal is generated by picking off a portion of each beam and is minimised through a phase-locked loop. Timing jitter in the synchronisation causes visible noise in images. However this noise can be eliminated by switching over to a separate phase-locked loop on a higher harmonic of the error signal [11]. By using the ninth harmonic the timing jitter is maintained at less than 215 fs.

To generate a CARS signal, the phase shift between the pump and Stokes pulses must be adjusted in order that the two wavelengths can mix in the sample. The phase synchronisation is monitored with a GaAsP photodiode (G1116, Hamamatsu) positioned as shown in Figure 1. The band gap of the semiconductor is greater than either the pump or Stokes photon energies, so the laser wavelengths both lie outside of its spectral response range. However a photocurrent is generated through two-photon absorption in the material giving a signal from each beam which is proportional to the square of its intensity [33]. Additionally, a cross-correlation signal is detected when the phase shift is less than the pulse duration [34], i.e. when pulses from the pump laser partially overlap pulses from the Stokes laser. The phase shift of the harmonic phase-locked loop is optimised to maximise the cross-correlation signal in order to ensure the pulses are fully overlapped.

The lateral resolution of the CARS microscope was measured at 0.26 μm, and the axial resolution at 1.5 μm. These measurements were made by imaging titanium oxide nanopowder (Aldrich) with particle diameters less than 0.1 μm. TiO_2 has an intrinsically high nonresonant third-order susceptibility [35], producing bright points in images which can be used as an approximation to point sources. The resolutions were determined from line profiles taken laterally and axially through a particle.

To test the microscope system CARS images of polystyrene beads in water were recorded. Figure 2 shows F-CARS (A) and E-CARS (B) images. A nonresonant background signal is generated along

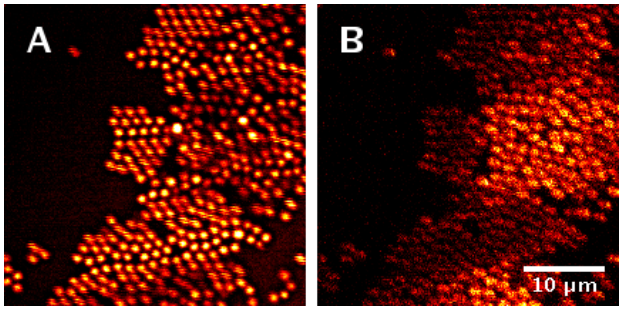

Figure 2 F-CARS and E-CARS images of polystyrene beads in water, 1.2 μm diameter, with the detector set up in forward (**A**) and backward (**B**) detection geometries. The Raman shift is 2845 cm^{-1}. The laser power incident on the sample is estimated at 20 mW. The acquisition time is 40 μs/pixel. The images are the average of 4 scans, each taking 2.7 s.

with the resonant CARS signal. The direction of the signals depend both on the shape of the scatterer and its size relative to the pump wavelength λ_p [20, 36]. For these 1.2 μm ($= 1.7\lambda_p$) diameter spherical beads the E-CARS signal is expected to be substantially weaker than the F-CARS. However, the nonresonant signal from the water goes forward, reducing contrast in F-CARS images, whilst E-CARS images are free of this background. The signal-to-background ratios in Figure 2 were determined by comparing the signal from the centre of the beads with the average signal from an area of the water. The E-CARS image (B) showed an improvement in signal-to-background ratio over the F-CARS image (A) by a factor of 2. Despite this E-CARS generally produces poorer quality images with more noise, due the lower resonant CARS signal and the size-dependence of the scattering. For imaging thin damage-sensitive samples such as fixed cells F-CARS is the preferred configuration.

Two-photon imaging is achieved on the same set-up by using the Stokes laser to excite GFP. The backward signal is recorded with a GFP filter in place (Brightline 514/30, Semrock). Although the CARS signal wavelength at 593 nm overlaps the tail of the GFP emission spectrum only minimal fluorescent signal was observed in the CARS detection channel which did not affect CARS images. This was confirmed by recording 'dark' images with the pump and Stokes lasers synchronised, but out of phase.

3. Results and discussion

CARS images of healthy uninfected NIH/3T3 fibroblasts were recorded by excitation of the aliphatic C–H vibration. An image of a typical cell is shown in Figure 3(A). Figure 4 shows a stack of images of

Journal of
BIOPHOTONICS

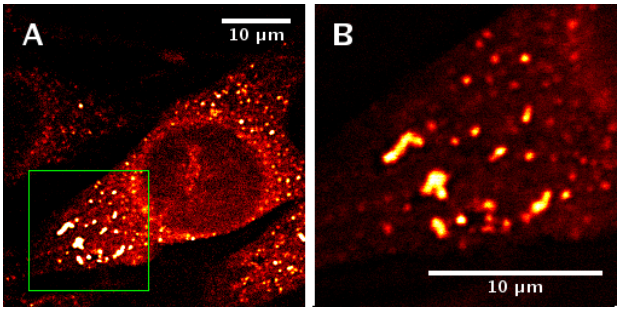

Figure 3 F-CARS image of a fibroblast cell at a Raman shift of 2845 cm^{-1} (**A**). The cell nucleus appears dark; the bright spots are lipid droplets. An enlarged view of the lipid droplets (**B**) was recorded by scanning the area marked by the green square in (A). The laser power incident on the sample is estimated at 28 mW. The images are the average of 4 scans, each taking 2.6 s.

the same cell, demonstrating the optical sectioning capability of CARS. The stack was recorded by focusing the beams at increasing depths through the cell. From this figure the thickness of the cell is estimated at 4 µm. The cell nucleus appears dark as it is devoid of structural lipids, although the sections in Figure 4 reveal some inhomogeneities which may be caused by signalling lipids [37]. In contrast, the cytosol—where lipid droplets, vesicles and organelles can be found—shows much brighter regions. The high intensity spots are lipid droplets [31]. An enlarged view of these droplets, Figure 3(B), was recorded by reducing the size of the scanning area to the square region marked in Figure 3(A). The size (full width at half maximum) of the smallest lipid droplets visible is 0.48 µm. Lipid droplets are used by the cells as storage for energy reserves, hydrophobic compounds such as cholesterol, and as a reservoir for lipid membrane building blocks [22]. In our studies, we observed a deterioration of these droplets in the fixed cells after a storage time of about ten days, leading to bigger and more diffuse bright spots (images not shown); this has also been also reported by Fujimoto et al. [38].

Cells infected with mouse cytomegalovirus (MCMV) were also imaged at the same C–H vibration band. Figure 5 shows two images. In contrast to the triangular stretched shape of healthy cells (Figure 3) the infected cells undergo characteristic morphological changes. They become more rounded and the nucleus expands, leading to a compression of the cytosolic lipid droplets and cellular compartments. To quantify nuclear expansion the dimensions of healthy and infected cell nuclei were measured from 40 cell images of each type. The elliptical region outlined by the nuclear boundary can be readily identified in images due to the drop in signal inside the nucleus and the absence of lipid droplets. The median nuclear area of healthy cells was 152 μm^2. For infected cells it was 336 μm^2, approximately twice the area. The wide variation in the nuclear sizes of infected cells suggests that they were in different stages of infection at the time of fixation. We observed many infected cells with nuclei greater than 500 μm^2 in area. In some cases the nucleus had expanded to fill almost the whole cell.

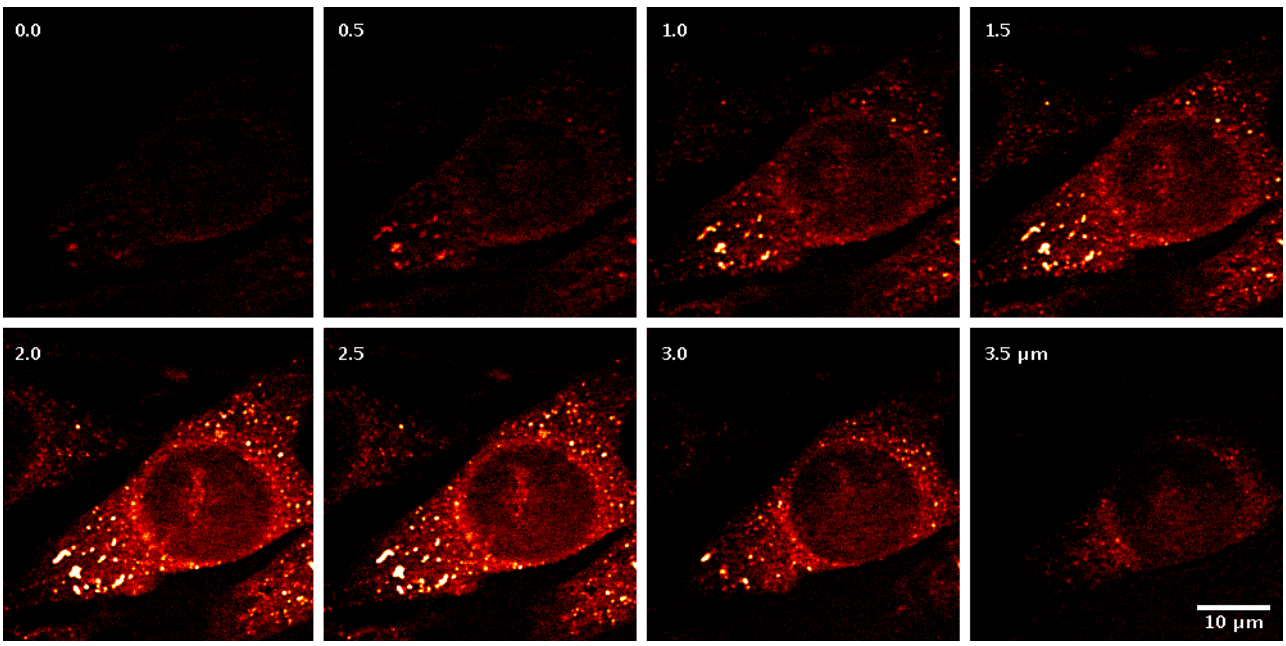

Figure 4 Stack of F-CARS images of a fibroblast cell (also shown in Figure 3) at increasing depths. The numbers indicate the depth relative to the first image.

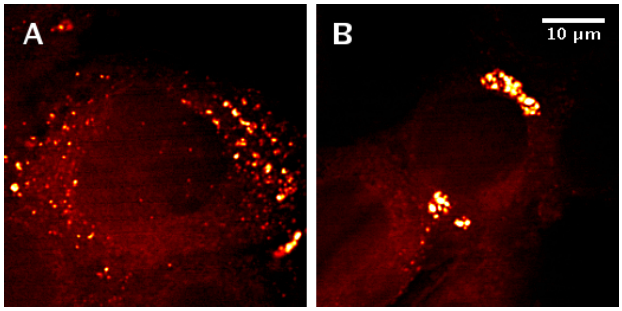

Figure 5 F-CARS images of fibroblast cells infected with mouse cytomegalovirus. The Raman shift is 2845 cm^{-1}. Infected cells show expansion of the cell nucleus (**A**). Some cells also showed dense accumulations of lipid droplets at the edge of the nucleus (**B**). The images are the average of 4 scans, each taking 11 s.

Observation of nuclear expansion is consistent with what is known about cytomegalovirus replication [39, 40]. During infection the viral capsid is transported to the nucleus of the host cell into which it releases its own genetic code and starts replication. Translated viral mRNA is released into the cytosol where viral protein production is conducted. The viral proteins then enter the nucleus. The mechanism by which this occurs in cytomegalovirus is not completely understood, however the viral proteins are used to assemble new capsids inside the nucleus. This leads to an enlargement of the nucleus inhibiting cell function and causing the loss of its normal morphology, resulting in a rounded and swollen shape. The new capsids are released into the cytosol through a primary envelopment process at the nuclear membrane. They are then budded through a second envelopment step resulting in infectious viral particles ready for release into the extracellular environment.

In some cases infected cells exhibited dense accumulations of lipid droplets at the nuclear periphery. Figure 5(B) shows an example. We speculate that this rearrangement from the healthy cell lipid distribution is attributable to the virus infection and may play a role in the assembly process of new virions. Virus-induced rearrangements of lipid droplets have been observed with other viruses. For example, the replication of the hepatitis C virus involves the recruitment of lipid droplets to play a role in viral particle assembly and transport, as recently reported by McLaughlan et al. [41, 42].

To track the infection, a separate sample of cells infected with a genetically modified virus expressing GFP (MCMV-GFP) was used. CARS, two-photon and bright field images were recorded, shown in Figure 6. The cells visible in the CARS image, Figure 6(A), show again the characteristic morphological changes associated with infection: nuclear expansion and rounding of the cell shape. Figure 6(B) shows a

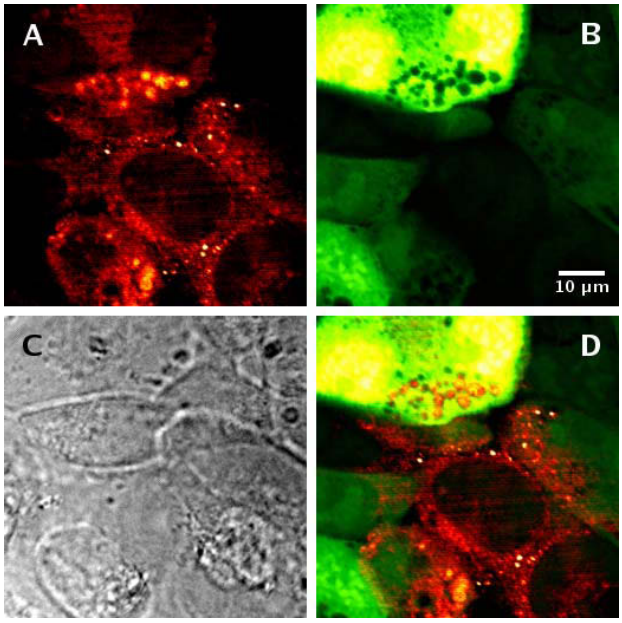

Figure 6 F-CARS image of fibroblast cells at a Raman shift of 2845 cm^{-1} during infection with a genetically modified mouse cytomegalovirus which expresses the green fluorescent protein with the immediate early promoter 3 (**A**). The corresponding two-photon image showing GFP (**B**). Bright field image (**C**). The CARS and two-photon images are superimposed (**D**). The acquisition times for (A) and (B) are both 40 µs/pixel. The images are the average of 4 scans, each taking 11 s.

two-photon image. The GFP is expressed together with, but not fused to, the viral proteins in the cytosol and then diffuses throughout the cell. In all two-photon images we observed a large fluorescence signal from the cell nucleus, indicating a higher concentration of GFP in the nucleus than in the cytosol. This result is unexpected, however little is known about the mechanisms employed by cytomegalovirus in transporting viral proteins into the nucleus. Zones of depleted GFP concentration are also clearly visible in Figure 6(B). These features were common to most two-photon images. They are either lipid droplets or inclusion bodies. Lipid droplets appear dark in two-photon images as hydrophilic GFP is excluded from the non-polar environment. Inclusion bodies are known to contain proteins, or parts of proteins, in unfolded form. Unfolded GFP in these bodies will not fluoresce, leaving dark spaces. The two features are readily distinguished by comparison with the corresponding CARS image, where lipid droplets appear bright and inclusion bodies are dark (see Abstract Figure). The overlay of CARS and two-photon images in Figure 6(D) shows some cells displaying the morphological characteristics of infection, but little or no fluorescence. These cells may be infected by MCMV-GFP which has undergone faulty replication resulting in the GFP expression being switched off.

Journal of
BIOPHOTONICS

Cells infected with the two viral strains, MCMV and MCMV-GFP, displayed the same morphological changes in CARS images. The two-photon images of the MCMV-GFP strain revealed the extent of viral protein expression. This method can be applied to enhance understanding of the role played by lipid droplets in viral replication and aid investigation of protein transport during infection. As GFP expression is non-destructive to the cell the method is not limited to imaging fixed samples but may be readily applied to live cells.

4. Conclusion

High resolution CARS and two-photon fluorescence microscopies have been combined to image infection of fibroblast cells by mouse cytomegalovirus. Morphological changes were observed, including expansion of the nucleus to approximately double its original area, rounding of the cell shape and, in some cases, rearrangement of lipid droplet distribution. In cells infected with a genetically modified strain of the virus, the green fluorescent protein was expressed in the cell and transported to the nucleus. This study demonstrates the utility of combining CARS and two-photon imaging modalities to establish correlations between viral protein expression and perturbations to the host cell. Further work is underway to continue these investigations with live cells.

Acknowledgements We are grateful to Alvin Yeh and Anthony Lee of Texas A & M University for assistance with microscopy software. The authors would also like to thank Garwin Sing at the University of Edinburghs Division of Pathway Medicine for providing the GFP modified virus, and advice. This work was supported by the Scottish Universities Physics Alliance.

Iain Robinson graduated from the University of Edinburgh in 2004 with a Master of Physics degree. He returned to Edinburgh to undertake a Ph.D. in laser microscopy in the School of Physics and Astronomy. He is currently working on new applications of CARS microscopy.

Michael Ochsenkühn studied Chemistry at the University of Freiburg (Germany) where he worked on the re-engineering of Mycobacterium smegmatis porin A for his Diploma thesis, graduating in 2006. Afterwards he joined Colin Campbells research group at the University of Edinburgh (Scotland, UK) to obtain a Ph.D. in Chemistry. He is currently working on surface enhanced Raman scattering based sensors for the detection of proteins and is interested in the intracellular application of gold nanoparticles and their influence on living cells. Furthermore he is working in the Division of Pathway Medicine investigating host pathogen interactions.

Colin Campbell is an EaStCHEM research fellow. His research group in the Division of Pathway Medicine conducts interdisciplinary research towards understanding the fundamental interactions between biomolecules and physical systems. This involves both electrochemical and photochemical research, the ultimate goal of which is the integration of physical sciences and life sciences for the benefit of applications and understanding in medicine. Specifically his group works on arrays of miniaturised biosensors, new imaging modalities or combinations thereof.

Gerard Giraud graduated from the University of Lyon (France) and received his Ph.D. in Physics in 2003 from the University of Strathclyde (UK), investigating the low frequency modes of proteins. Gerard has extensive experience in the field of optical spectroscopy and imaging techniques, in particular time resolved fluorescence and nonlinear spectroscopy. After three years of postdoctoral research at the École Polytechnique Fédéral de Lausanne (Switzerland), he

joined the COSMIC research centre in 2006 at the University of Edinburgh; where he is now working on the design of new transduction methods for biosensing application.

Will Hossack is Senior Lecturer in Physics. His background is in optics and imaging systems including optical manipulation, real-time holographic systems and digital image processing and analysis. He is a member of the COSMIC Research Centre at the University of Edinburgh with a particular interest in the development of optical instrumentation for bio-imaging.

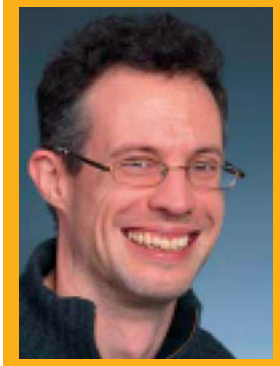

Jochen Arlt is Lab Manager and Research Fellow of COSMIC. He obtained his Ph.D. in Physics from the University of St Andrews and has extensive expertise in optical imaging techniques and novel instrumentation, with particular focus on optical tweezers and fluorescence techniques. He has broad experience in application of optical techniques within interdisciplinary projects in soft-condensed matter and biophysics.

Jason Crain is Professor of Applied Physics. His background is in condensed matter physics and disordered materials studied using experimental and computational techniques. He is Director of the COSMIC Research Centre at the University of Edinburgh, regular Visiting Professor at the IBM T. J. Watson Research Center in New York. He is currently on secondment as Divisional Head of Science at the UK National Physical Laboratory. He has extensive experience in leading large collaborative research programs at the physical/life science interface in both academic and industrial sectors.

References

[1] S. Tyagi, Imaging intracellular RNA distribution and dynamics in living cells. Nat. Methods **6**, 331–338 (2009).
[2] R. Weissleder and M. J. Pittet, Imaging in the era of molecular oncology. Nature **452**, 580–589 (2008).
[3] P. Lang, K. Yeow, A. Nichols, and A. Scheer, Cellular imaging in drug discovery. Nat. Rev. Drug Discovery **5**, 343-356 (2006).
[4] W. Denk, J. Strickler, and W. Webb, Two-photon laser scanning fluorescence microscopy. Science **248**, 73–76 (1990).
[5] I. D. Johnson, Practical considerations in the selection and application of fluorescent probes, in: J. B. Pawley (ed.), Handbook of Biological Confocal Microscopy, (Springer, 2006), pp. 353–367.
[6] R. Gauderon, P. B. Lukins, and C. J. R. Sheppard, Three-dimensional second-harmonic generation imaging with femtosecond laser pulses. Opt. Let. **23**, 1209–1211 (1998).
[7] P. Lee, A. T. Yeh, and K. J. Bayless, Nonlinear optical microscopy reveals invading endothelial cells anisotropically alter three-dimensional collagen matrices. Exp. Cell. Res. **315**, 396–410 (2009).
[8] P. R. T. Jess, M. Mazilu, K. Dholakia, A. C. Riches, and C. S. Herrington, Optical detection and grading of lung neoplasia by Raman microspectroscopy. Int. J. Cancer **124**, 376–380 (2009).
[9] A. Zumbusch, G. R. Holtom, and X. S. Xie, Three-dimensional vibrational imaging by coherent anti-Stokes Raman scattering. Phys. Rev. Lett. **82**, 4142–4145 (1999).
[10] C. L. Evans, E. O. Potma, M. Puorishaag, D. Côté, C. P. Lin, and X. S. Xie, Chemical imaging of tissue in vivo with video-rate coherent anti-Stokes Raman scattering microscopy. P. Natl. Acad. Sci. USA **102**, 16807–16812 (2005).
[11] E. O. Potma, D. J. Jones, J. X. Cheng, X. S. Xie, and J. Ye, High-sensitivity coherent anti-Stokes Raman scattering microscopy with two tightly synchronized picosecond lasers. Opt. Lett. **27**, 1168–1170 (2002).
[12] H. Kano and H. Hamaguchi, Vibrationally resonant imaging of a single living cell by supercontinuum-based multiplex coherent anti-Stokes Raman scattering microspectroscopy. Opt. Express **13**, 1322–1327 (2005).
[13] F. Ganikhanov, S. Carrasco, X. S. Xie, M. Katz, W. Seitz, and D. Kopf, Broadly tunable dual-wavelength light source for coherent anti-Stokes Raman scattering microscopy. Opt. Lett. **31**, 1292–1294 (2006).
[14] M. Jurna, J. P. Korterik, C. Otto, J. L. Herek, and H. L. Offerhaus, Background free CARS imaging by phase sensitive heterodyne CARS. Opt. Express **16**, 15863–15869 (2008).
[15] H. Kano and H. Hamaguchi, Coherent Raman imaging of human living cells using a supercontinuum light source. Jpn. J. Appl. Phys. 1 **46**, 6875–6877 (2007).

[16] C. Krafft, A. A. Ramoji, C. Bielecki, N. Vogler, T. Meyer, D. Akimov, P. Rösch, M. Schmitt, B. Dietzek, I. Petersen, A. Stallmach, and J. Popp, A comparative Raman and CARS imaging study of colon tissue. J. Biophotonics **2**, 303–312 (2009).
[17] H. Chen, H. Wang, M. N. Slipchenko, Y. Jung, Y. Shi, J. Zhu, K. K. Buhman, and J. X. Cheng, A multimodal platform for nonlinear optical microscopy and microspectroscopy. Opt. Express **17**, 1282–1290 (2009).
[18] H. Wang, T. T. Le, and J. X. Cheng, Label-free imaging of arterial cells and extracellular matrix using a multimodal CARS microscope. Opt. Commun. **281**, 1813–1822 (2008).
[19] J. X. Cheng, A. Volkmer, L. D. Book, and X. S. Xie, An epi-detected coherent anti-Stokes Raman scattering (E-CARS) microscope with high spectral resolution and high sensitivity. J. Phys. Chem. B **105**, 1277–1280 (2001).
[20] J. X. Cheng and X. S. Xie, Coherent anti-Stokes Raman scattering microscopy: Instrumentation, theory, and applications. J. Phys. Chem. B **108**, 827–840 (2004).
[21] J. M. Girkin and G. McConnell, Advances in laser sources for confocal and multiphoton microscopy. Microsc. Res. Techniq. **67**, 8–14 (2005).
[22] Y. Guo, K. R. Cordes, R. V. Farese, and T. C. Walther, Lipid droplets at a glance. J. Cell Sci. **122**, 749–752 (2009).
[23] B. Helms, Host-Pathogen interactions: Lipids grease the way. Eur. J. Lipid Sci. Tech. **108**, 895–897 (2006).
[24] M. Bonn, M. Müller, H. A. Rinia, and K. N. J. Burger, Imaging of chemical and physical state of individual cellular lipid droplets using multiplex CARS microscopy. J. Raman Spectrosc. **40**, 763–769 (2009).
[25] X. Nan, A. M. Tonary, A. Stolow, X. Xie, and J. P. Pezacki, Intracellular imaging of HCV RNA and cellular lipids by using simultaneous two-photon fluorescence and coherent anti-Stokes Raman scattering microscopies. Chem. Bio. Chem. **7**, 1895–1897 (2006).
[26] B. Rakic, S. M. Sagan, M. Noestheden, S. Belanger, X. Nan, C. L. Evans, X. S. Xie, and J. P. Pezacki, Peroxisome proliferator-activated receptor alpha antagonism inhibits hepatitis C virus replication. Chem. Biol. **13**, 23–30 (2006).
[27] A. Angulo, P. Ghazal, and M. Messerle, The major immediate-early gene *ie3* of mouse cytomegalovirus is essential for viral growth. J. Virol. **74**, 11129–11136 (2000).
[28] D. H. Lee, D. Wenkert, M. P. Whyte, M. T. Trese, and O. A. Cruz, Congenital blindness and osteoporosis-pseudoglioma syndrome. J. AAPOS **7**, 75–77 (2003).
[29] M. Kenzelmann and K. Mühlemann, Transcriptome analysis of fibroblast cells immediate-early after human cytomegalovirus infection. J. Mol. Biol. **304**, 741–751 (2000).
[30] T. Ranneberg-Nilsen, M. Bjørås, L. Luna, R. Slettebakk, H. A. Dale, E. Seeberg, and H. Rollag, Human cytomegalovirus infection modulates DNA base excision repair in fibroblast cells. Virology **348**, 389–397 (2006).
[31] X. Nan, J. X. Cheng, and X. S. Xie, Vibrational imaging of lipid droplets in live fibroblast cells with coherent anti-Stokes Raman scattering microscopy. J. Lipid. Res. **44**, 2202–2208 (2003).
[32] L. S. Ma, R. K. Shelton, H. C. Kapteyn, M. M. Murnane, and J. Ye, Sub-10-femtosecond active synchronization of two passively mode-locked Ti:sapphire oscillators. Phys. Rev. A **64**, 021802 (2001).
[33] Y. Takagi, T. Kobayashi, K. Yoshihara, and S. Imamura, Multiple- and single-shot autocorrelator based on two-photon conductivity in semiconductors. Opt. Lett. **17**, 658–660 (1992).
[34] T. Minamikawa, N. Tanimoto, M. Hashimoto, T. Araki, M. Kobayashi, K. Fujita, and S. Kawata, Jitter reduction of two synchronized picosecond mode-locked lasers using balanced cross-correlator with two-photon detectors. Appl. Phys. Lett. **89**, 191101 (2006).
[35] J. Moger, B. D. Johnston, and C. R. Tyler, Imaging metal oxide nanoparticles in biological structures with CARS microscopy. Opt. Express **16**, 3408–3419 (2008).
[36] J. X. Cheng, A. Volkmer, and X. S. Xie, Theoretical and experimental characterization of coherent anti-Stokes Raman scattering microscopy. J. Opt. Soc. Am. B **19**, 1363–1375 (2002).
[37] R. F. Irvine, Nuclear lipid signalling. Nat. Rev. Mol. Cell Biol. **4**, 349–361 (2003).
[38] T. Fujimoto, Y. Ohsaki, J. Cheng, M. Suzuki, and Y. Shinohara, Lipid droplets: a classic organelle with new outfits. Histochem. Cell Biol. **130**, 263–279 (2008).
[39] M. J. Reddehase and N. Lemmermann, Cytomegaloviruses: molecular biology and immunology, (Caister Academic Press, 2006), pp. 619.
[40] T. C. Mettenleiter, B. G. Klupp, and H. Granzow, Herpesvirus assembly: a tale of two membranes. Curr. Opin. Microbiol. **9**, 423–429 (2006).
[41] S. Boulant, M. Douglas, L. Moody, A. Budkowska, P. Targett-Adams, and J. McLauchlan, Hepatitis C virus core protein induces lipid droplet redistribution in a microtubule- and dynein-dependent manner. Traffic **9**, 1268–1282 (2008).
[42] J. McLauchlan, Lipid droplets and hepatitis C virus infection. Biochim. Biophys. Acta **1791**, 552–559, (2009).

